Novel Ground States of Bose-Condensed Gases

by

Jamil R. Abo-Shaeer

Submitted to the Department of Physics
in partial fulfillment of the requirements for the degree of

Doctor of Philosophy

at the

MASSACHUSETTS INSTITUTE OF TECHNOLOGY

October 2004 [Feb. 2005]

Author .....
Department of Physics
October 1, 2004

Certified by .....
Wolfgang Ketterle
John D. MacAurthur Professor of Physics
Thesis Supervisor

Accepted by .....
Thomas J. Greytak
Professor of Physics, Associate Department Head for Education

Novel Ground States of Bose-Condensed Gases

by

Jamil R. Abo-Shaeer

Submitted to the Department of Physics
on October 1, 2004, in partial fulfillment of the
requirements for the degree of
Doctor of Philosophy

Abstract

Bose-Einstein condensates (BEC) provide a novel tool for the study of macroscopic quantum phenomena and condensed matter systems. Two of the recent frontiers, quantized vortices and ultracold molecules, are the subject of this thesis.

The formation of highly-ordered vortex lattices in a Bose-condensed gas has been observed. These triangular lattices contain more than 150 vortices with lifetimes of several seconds. The vortices were generated by rotating the condensate with a scanning blue-detuned laser beam. Depending on the stirrer size, vortices were either nucleated at discrete surface-mode resonances (large beams) or over a broad range of stirring frequencies (small beams). Additionally, the dynamics of the lattices have been studied at finite temperature by varying the condensed fraction of atoms in the system. The decay of angular momentum is observed to be strongly temperature-dependant, while the crystallization of the lattice appears to be insensitive to temperature change.

Recently, the field of BEC has been extended to include cold molecules. Here ultra-cold sodium molecules were produced from an atomic BEC by ramping an applied magnetic field across a Feshbach resonance. These molecules were used to demonstrate coherent molecular optics. In particular, we have extended Kapitza-Dirac and Bragg diffraction to cold molecules. By measuring the Bragg spectrum of the molecules immediately after their creation, the conversion from atoms to molecules was shown to be coherent - the matter wave analog to frequency doubling in optics. In addition, the more general process of sum-frequency generation was demonstrated. Atoms prepared in two momentum states, prior to creating molecules, were observed to cross-pair, generating a third momentum state. Finally, molecular matter-wave interference was realized using an autocorrelation technique.

Thesis Supervisor: Wolfgang Ketterle
Title: John D. MacArthur Professor of Physics

For my family,

Nadya, Amir, Anita and Muhsin.

Acknowledgments

In my time in the Ketterle lab I have witnessed the group grow by leaps and bounds. When I arrived at MIT there were only two sodium experiments. Now we have a rubidium and lithium machine as well. Because of this, I have had the pleasure of working with many great people over the last five years and my acknowledgements are numerous. It's impossible to do each person justice in one or two sentences, but in the interest of brevity I must try. For the purposes of bookkeeping, I will *try* to go through lab by lab, although this will not be the rule.

First, I would like to thank Wolfgang Ketterle for giving me the opportunity to work in his lab. I only hope that I have been able to repay him in my time here. Wolfgang's cleverness is well-documented, so I needn't restate this fact. Rather, I'd like to thank him for his kindness and skill for inspiring excitement about physics. In addition, Wolfgang's ability to keep us feeling good about our work when we most needed it will always be appreciated.

When I arrived at MIT I was assigned to the "New Lab", the newly christened, 2nd generation BEC machine. In the beginning I had the benefit of working with three wonderful postdocs: Roberto Onofrio, Johnny Vogels, and Chandra Raman. Each had his own unique set of talents that contributed to my development. The four of us worked together on the second critical velocity experiment. Despite playing a small role in the experiment, I had more fun with this project than any other I've been a part of, and our off-key sing-a-longs are now a late-night standard in the New Lab.

Roberto Onofrio was the first to take me under his wing, showing me how to run the machine. Roberto's easy-going nature was a calming force in a lab known for its "strong personalities". His sense of humor kept us going during many frustrating nights. In particular, his impressions of members of the greater atomic physics community are second to none. Additionally, I thank him for his continued support and advice throughout my career.

Johnny Vogels and I had differing styles to say the least. This led to many "disagreements", but just like family we always resolved our differences quickly. One

similarity that Johnny and I did share was our eagerness in lab. Johnny's spirit was contagious, and he always kept things lively and fun. His free thinking led him to pursue many crazy ideas that didn't work and even crazier ones that did. It's taken me years of experience in the lab to fully appreciate Johnny's brilliance.

My time working with Chandra Raman was unforgettable. For my development as an experimental physicist I owe the greatest debt of gratitude to him. Chandra taught me most everything I know about BEC experiment and almost every good habit I have in lab is due to him. I greatly appreciate that he would step back and give me time in lab to work things out until I got them right. It was comforting to know that he was always there to put me back on track when I was confused or frustrated. His grad students are lucky to have him.

I'd like to thank Chris Kuklewicz for "showing me the ropes" in lab, and at MIT, when I first arrived. Special thanks also go to Dallin Durfee, and Michael Köhl. I didn't have the opportunity to work with either of them substantially, but I am grateful for their help in leaving such a wonderful experiment for me to work on.

Kaiwen Xu arrived in lab a year after me. At first I wasn't sure that we had much in common. But our mutual love of basketball quickly brought us together. Kaiwen and I endured much frustration working together on optical lattices, but we also had a lot of fun. Kaiwen's talent in both experiment and theory have made him an ideal coworker (and voice of reason). It's been a pleasure to work with him and I will sorely miss his fall-away jump shot and vastly underrated sense of humor.

Towards the end of my stay I had the pleasure of working with two wonderful, but vastly different individuals: Takashi Mukaiyama and Dan Miller. As a postdoc in the New Lab, Takashi established himself as a quiet leader. He was fun to work with and his intricate electronic inventions always amazed me. I learned a lot from Takashi, and I'm very sorry for what he learned from me. On one frustrating day I was horrified to find Takashi transcribing some of my particularly strong language in order to help himself learn English.

I can leave MIT confident that the quirky tradition and often erratic behavior of the New Lab is left in the buzz-saw hands of Dan Miller. Hollywood's eagerness and

sense of humor provided a much needed shot in the arm at a time when work in lab was particularly frustrating. Despite the obvious embarrassment it would cause him, Goose's gift of "Song 3" to the Ketterle Lab proved that he is the ultimate team player. I only hope that Soldier Boy's pain was worth the joy it brought to the rest of us. So C.O.G.S., I thank you for being a great labmate and friend.

Any discussion of the New Lab would not be complete without mentioning its forgotten member. My first memories of MIT are the times I spent talking to Zoran Hadzibabic. Zoran's "strange" sense of humor always kept me entertained. I will always regret not having the opportunity to continue working with him. However, we did have our fare share of communication outside of lab. Zoran and I had many profound discussions. The shortest being a knowing glance to me as he passed by my office, and the longest going from lab to the Miracle to the cold streets of Cambridge for another 4 hours.

I had the honor of entering MIT alongside Aaron Leanhardt. I could not have picked a better person to go through this experience with. Although I'm sure that it was an easy choice, I will always be indebted to Wolfgang and Dave Pritchard for choosing him. I could write several pages about Aaron, but I'll try to keep it brief. Aaron has been a great labmate, roommate, and friend to me. Over the past 5 years we've done problem sets, played and watched about every sport, worked, ate and lived together. Most of my favorite memories at MIT involve him. Cooking Thanksgiving dinner for the lab, watching him make the opposition look silly in IM football, filling our apartment up with a half ton of sand, and going with him to the emergency room after he shattered the lab obstacle course record (and the glass in Bldg. 36), are just a few. Inside and outside of lab Aaron never ceases to amaze me. His skills as a physicist are unquestionable. But besides being able to answer any question you throw at him, experimental or theoretical, Aaron also makes a better Christmas wreath, runs faster, and consistently eats the same meal better than any graduate student I've ever seen. I've got high expectations for him and I hope that our work allows us to continue our friendship for many more years.

As the grad students one rung above me, Ananth Chikkatur and Deep Gupta

were great role models both inside and outside of lab. They helped Aaron and me get our first apartment at 4 Marion (right below theirs). My discussions with Ananth (which invariably ended with him telling me I was crazy) were a constant source of amusement. Deep's level-headiness when those around him were going crazy and his ability to strike very thoughtful poses always impressed me. I will always cherish their sendoffs from lab: Ananth drumming on his back in a pile of sand in my living room and Deep's emergenece as the undisputed oil-wrestling champion of the lab.

The Old Lab/Science Chamber has had a revolving door of great students and postdocs. I always enjoyed discussing physics, politics, and basketball with Axel Görlitz. More recently Yong-Il Shin, Tom Pasquini, André Schirotzek, and Michele Saba have joined the effort. Besides being a great physicist, Yong's skills as a midfielder have provided our soccer team some much-needed credibility. Tom has gone above and beyond the call of duty in his short time at MIT. He spearheaded a successful effort to provide free healthcare for MIT graduate students. As a true Berkeleyan, he fought the good fight and I eagerly await his return to the East Bay. In addition to being a great guy, Andre provided solid blocking for our IM football and I thank him for never taking me up on my numerous offers to box/wrestle/fight him. Michele's cheeriness and good humor have been a great addition to the lab and he has also provided the soccer team with some much-needed ball control.

Now, on to the Lithium Lab. What's always impressed me about Claudiu Stan is his deep sense of electronics aesthetics. Claudiu's boxes appear as though they're built by the hands of God. Christian Schunck and Sebastian Raupauch are without a doubt the two nicest members of lab. Christian always has a bright smile and Sebastian's character and thoughtfulness are second to none.

I had the pleasure of knowing Martin Zwierlein first as an officemate and later as a labmate. My short partnership with Martin was very memorable, especially our $17 breakfasts at Fresco's (if you're familiar with Fresco's prices you know this is no small feat). I'll never forget Martin's deafening laugh and use of Rubik's cube imagery to describe social encounters. In addition, I'll miss our 4 a.m. coffee breaks, watching him chase a double espresso with a Red Bull and Snickers, and his pregame Bürger

König.

Every lab has to have a straight man, and Dominik Schneble has fulfilled this role for the Rubidium Lab. Dominik's easy-going nature and subtle humor will make him a great advisor for future grad students.

It's important to know that when a bad idea is too good to pass up, you always have someone there to encourage you to follow through. Which brings me to Micah Boyd. Micah and I have had many "memorable" moments (I'll leave it at that). He's been a great friend and partner in crime. I hope to continue our long and fruitful relationship of poor judgement at future conferences.

Gretchen Campbell is the little sister I never had. She does a lot for everyone and has brought some much need sweetness to the lab. I only hope that the rest of us don't rub off too much on her. Gretchen's dedication to work is incredible (and somewhat disturbing). Along with Aaron, those two make an unholy pair. Her cleverness and honesty will lead her to many great things and I eagerly anticipate reading of her future successes. I'll certainly be trying to convince her to join me out west when she's done at MIT. Finally, I must thank Gretchen for all the help she's given me while I finished up at MIT (including turning in this thesis).

The Ketterle lab has had a number of fine diploma students and undergraduates who deserve mention. The first of these is Robert Loew, with whom I spent many wonderful nights building our first AOM drivers together. Edem Tsikata was a hard worker and a great guy. I wish him much success at Harvard. Mimi Xue and Widagdo Setiawan both built a number of important boxes for the New Lab and also contributed a lot of youthful exuberance. Finally, Till Rosenband is in this group only by title. Till was a super-UROP and at one time the senior member of the Ketterle lab. His electronic skills are legendary. I wish I could have convinced him to stay at MIT, but I realize he needed to go off to the greener pastures of Boulder. I had a lot of fun working with him he gets some extra credit in Chapter 5.

Dave Pritchard deserves a lot of credit for graciously allowing us to take out our frustration as grad students on him. Despite agreeing with us, he still played it cool when Tom and I held sit-ins in his office or berated him for the actions of the

administration. Because of this, I forgive him for his incessant cheating in the lab pools.

There are a few other people from lab that also deserve mention: Dan Stamper-Kurn, Timan Pfau, Shin Inouye, Todd Gustavson, Christian Sanner, Eric Streed, Yoshio Torii, Jongchul Mun, Kai Dieckmann, Jamie Kerman, and Ellenor Emery.

Carol Costa was the surrogate mother to countless graduate students, postdocs, and professors. Carol always made sure that her family was happy and well-fed. She is deeply missed, but her legacy lives on in the sense of community that she helped to foster. As a hometown girl and diehard fan, I wish that Carol could have shared in the joy of our beloved Sox finally reversing the curse.

As the theorist of the hall, James Anglin was an invaluable source of information. James was always there to explain physics to me, and then re-explain it several times when I got confused. I particularly loved our discussions when James would partner up with Michael Crescimanno to play good cop/bad cop.

I arrived at MIT at the same time as Hydrogen group members Lia Matos and Kendra Vant. Much has changed in our time here, including the two of them becoming mothers. However, I will never forget the first semester we spent together doing late night problem sets. I was always pleased to pass Julia Steinberger in the corridor because she was quick to deliver some politically charged statement (of which I always agreed). The contributions of these three, and Cort Johnson, to the MIT community are commendable.

Unfortunately, the Vuletic group only recently joined our CUA family. I enjoyed getting to know Igor Teper, Adam Black, and Yu-ju Lin. Despite having been at MIT for my entire stay, I only recently got to know James Thompson. I had a great time playing IM sports with him and the excitement on his face when we successfully executed his hook-and-lateral play was priceless.

Finally, I would like to thank some people outside of lab who have helped in my development (not always in a positive way).

My high school friends are always there to simultaneously support and mock my efforts in physics. I am forever grateful to: Jeff Riley for phoning in live play-by-play

when I was missing important games because I had to be in lab. Dave Andreasen for keeping me grounded by sharply reminding me how uncool physics is. Lian Rameson for sarcastically opining on the sexiness of physics whenever I got too excited about it. Teresa Mendez for a providing me a link to the world outside MIT and briefing me before her book club events so I could pretend I had read the book. Jeff Shelton for reminding me that I better figure out a use for this stuff if I want to be employed. Dave Mayer for reliving the glory days with me, one old grad student to another. Brett Bezsylko for the time we spent together in college learning how to be good students. Better late than never.

At UCSB I had the good-fortune of sharing the college experience with Omer Ansari, Run Dul and Joe Gonzalez. I had a wonderful time with each of these guys. In addition, I'd like to thank Hau Hwang for preventing me from failing out during my second quarter and teaching me good study habits (i.e. read the book and do the homework). My first physics TA, Seth Rosenberg, showed me that physics was fun and really got me excited about the field. The courses I took from Roger Freedman were among the best I've had. I am greatly indebted to Phil Lubin and Jeff Childers for giving me my first lab experience. Jeff Childers took me under his wing, teaching me to leave all places better than I found them and that nice-looking electronics work better.

Shortly after arriving at Berkeley I met two other transfer students, Kelly Campbell and Eric Jones. I could not have met to better guys. I had a great time learning physics with them and sharing in disbelief as one of our professors destroyed a trash can during class. Stuart Freedman gave me my first shot at cold atom physics. I hope to repay him for this during my postdoctoral work. Paul Vetter taught me a great deal about cooling and trapping sodium. Because of him, I was able to make a quick transition to work at MIT.

My first year at MIT I lucked out by getting placed with three great roommates: Anton Thomas, Johann Chan, and Peter McNamara. It was a pleasure living with them and I wish them all the success. In particular, Anton is without a doubt the nicest guy I've ever met and now a great father too.

Despite the bitter cold, my last winter in Boston was made warm by Royce Brooks. God only knows why she would ever get mixed up with a boy from the wrong side of town, but I'm certainly glad she did. Royce's sense of humor and quick wits were always dazzling. I hope that she can one day forgive me for putting carrots in her sweet potato pie to make it extra sport-healthy.

It's fitting that Aaron and I shared an apartment with the fortuitously named Kate DuBose. In addition to providing me with sorely needed background vocals, Kate also had the unenviable job of taste-tester for all my culinary inventions. More importantly, she taught Aaron and me that there was nothing funny about physics. Besides all these things, our shared love for the worst in reality tv always made me eager to rush home. On a final note - Kate and Aaron were the greatest roommates ever. The night we got vortices and I called home at 4:00 a.m. to tell Aaron and her. When I got home at 6:00 a.m. they both jumped out of bed to congratulate me and share in my excitement. (Kate fondly remembers this moment because I made her celebratory pancakes for breakfast.)

Jamila Wignot has been a very important part of my life throughout the last 12 years. She's seen me at my best, but mostly at my worst, yet she has been a constant throughout. Her friendship means a tremendous amount to me and I was very lucky to have her share in this experience with me. Jamila's wit/charm/talent delight me to no end. She's always challenged me to be a better person, and hopefully after this experience I will be. I'll let her be the judge.

Finally, I would like to thank my family, for whom this work is dedicated. I owe everything to them. To my sister Nadya, who always seems to think what I do is great, no matter how stupid it actually is. She also deserves extra credit for providing some wonderful artwork for my thesis. My brother Amir, who always reminds me that physics is useless if you can't convey your message to others. My mother Anita, who has always been caring and nurturing, as evident by the 7 meals a day she fed me while I wrote this thesis from her kitchen table. And to my Father, Muhsin, who has been my greatest mentor, spending countless hours teaching me the right approach to physics and to life.

Contents

List of Figures

Chapter 1

Introduction

By convention color, by convention bitter, by convention sweet, in reality atoms and void.

-Democritus

The birth of atomic theory can be traced back to the 5th century B.C. when Greek philosophers Democritus and Leucippus postulated that matter and space were not infinitely divisible. Human perception leads to gross classifications based primarily on senses, such as 'hot' or 'cold'. The revolutionary postulate of the Greek atomists was that such outward qualities of matter are reducible and should be fundamentally determined by the species of atom and the amount of void that it is composed of. Many however, including Aristotle, rejected this idea, and so it lay dormant for centuries.

In the early 1800's atomic theory reemerged with John Dalton's observation that aggregate matter is reducible to elements, and that all atoms of a certain element have the same size and weight. Thus, it is with these two notions, classification and sameness, that I begin this work.

1.1 Identical Particles

The strange behavior of matter at low temperatures stems from Nature's desire to create like particles identically to one another. That is to say, there is no discernable difference between any two electrons, protons, atoms, etc. Indistinguishability

profoundly affects the behavior of quantum systems, leading to such phenomena as Bose-Einstein Condensation and superfluidity.

To see how this is manifest, consider two (non-interacting) identical particles occupying the single-particle states ψ_a and ψ_b. Suppose now we are charged with the task of constructing a composite wavefunction $\Psi(\vec{r_1}, \vec{r_2})$ to describe this system. Our naive choice might be to simply take the product of the two states.

$$\Psi(\vec{r_1}, \vec{r_2}) = \psi_a(\vec{r_1})\psi_b(\vec{r_2}) \tag{1.1}$$

This would certainly be the correct choice if the two particles were distinguishable. However, it is a bit more complicated for identical particles. Remember, we cannot distinguish between the two, so how can we say with certainty that particle 1 is in ψ_a and particle 2 is in ψ_b? We only really know that one particle resides in ψ_a and the other in ψ_b. To solve this dilemma, we look for eigenstates of the Hamiltonian describing the two-particle system.

Let us define an exchange operator $\mathcal{O}$ that, when applied to $\Psi(\vec{r_1}, \vec{r_2})$, swaps the two particles

$$\mathcal{O}\Psi(\vec{r_1}, \vec{r_2}) = \Psi(\vec{r_2}, \vec{r_1}) \tag{1.2}$$

Since these two particles are identical we know that the potential energy term $V(\vec{r_1}, \vec{r_2})$ in the Hamiltonian H must treat the two particles equally e.g. $V(\vec{r_1}, \vec{r_2})$=$V(\vec{r_2}, \vec{r_1})$. Therefore, the exchange operator $\mathcal{O}$ and H are compatible observables ($[H, \mathcal{O}] = 0$), and so eigenstates of $\mathcal{O}$ are also eigenstates of H. If we apply $\mathcal{O}$ twice to $\Psi(\vec{r_1}, \vec{r_2})$ we must return to the original state

$$\mathcal{O}^2\Psi(\vec{r_1}, \vec{r_2}) = \Psi(\vec{r_2}, \vec{r_1}) \tag{1.3}$$

Therefore, the eigenvalues of $\mathcal{O}$ are ± 1, which means our composite wavefunction $\Psi(\vec{r_1}, \vec{r_2})$ is either symmetric (+1) or antisymmetric (-1) under exchange.

$$\Psi(\vec{r_1}, \vec{r_2}) = \pm\Psi(\vec{r_1}, \vec{r_2}) \tag{1.4}$$

Our naive guess (Eq(1.1)) fails to meet this criteria

$$\Psi(\vec{r_1}, \vec{r_2}) = \psi_a(\vec{r_1})\psi_b(\vec{r_2}) \neq \pm\psi_a(\vec{r_2})\psi_b(\vec{r_1}) \tag{1.5}$$

Because our particles are identical, our intuition tells us that they must each be represented equally in both states. With this in mind we construct the following

$$\Psi_+(\vec{r_1}, \vec{r_2}) = \frac{1}{\sqrt{2}}[\psi_a(\vec{r_1})\psi_b(\vec{r_2}) + \psi_a(\vec{r_2})\psi_b(\vec{r_2})] \tag{1.6}$$

$$\Psi_-(\vec{r_1}, \vec{r_2}) = \frac{1}{\sqrt{2}}[\psi_a(\vec{r_1})\psi_b(\vec{r_2}) - \psi_a(\vec{r_2})\psi_b(\vec{r_1})] \tag{1.7}$$

Both of these states clearly obey the (anti-)symmetry condition of Eq(1.4). As was the case with our naive guess $\psi_a(\vec{r_1})\psi_b(\vec{r_2})$, superpositions of these two eigenstates are forbidden by Eq(1.4). Hence, we see that identical particles come in two distinct classes. Those symmetric under exchange, $\Psi_+(\vec{r_1}, \vec{r_2})$, we call "Bosons" and those antisymmetric under exchange, $\Psi_-(\vec{r_1}, \vec{r_2})$, we dub "Fermions".

All particles in nature *must* fall into one of these two categories (Democritus is redeemed!). The actual mechanism that makes them one or the other relates to their spin. The proof of this is beyond the scope of this simple treatment so I simply state the result:[1]

All Particles with integer spin (0, 1, 2 ...) are *Bosons.*

All particles with half-integer spin (1/2, 3/2, 5/2 ...) are *Fermions.*

Although implicitly stated above, I must stress that even composite particles such as atoms fall into one of these two classes. Since atoms are composed of Fermions (electrons, protons, neutrons), those with an odd number of constituent particles are Fermions and those with even number are Bosons.

[1]The spin-statistics theorem is a well-documented result of relativistic quantum mechanics.

1.2 Bosons and Fermions

The subtle distinction in symmetry leads to profoundly different behavior between the two species. To see this, consider the case of $\psi_a = \psi_b$. For Bosons we find that

$$\Psi(\vec{r_1}, \vec{r_2})_+ = \frac{1}{\sqrt{2}}[\psi_a(\vec{r_1})\psi_a(\vec{r_2}) + \psi_a(\vec{r_2})\psi_a(\vec{r_1})] = \sqrt{2}[\psi_a(\vec{r_1})\psi_a(\vec{r_2})] \tag{1.8}$$

However, for Fermions

$$\Psi(\vec{r_1}, \vec{r_2})_+ = \frac{1}{\sqrt{2}}[\psi_a(\vec{r_1})\psi_a(\vec{r_2}) - \psi_a(\vec{r_2})\psi_a(\vec{r_2})] = 0 \tag{1.9}$$

which is to say that Bosons may occupy the same quantum state, while Fermions cannot (the Pauli Exclusion principle). Because of this we sometimes attribute "social" characteristics to Bosons and Fermions. Fermions are introverts, avoiding their neighbors at all costs (see Figure 1-1). Bosons, on the other hand, are quite jovial and enjoy each other's company (bosonic enhancement).

1.3 Quantum Statistical Mechanics

The observation that Fermions obey Pauli exclusion, while any number of Bosons can occupy a single quantum state, leads to profound differences in their many-body states. However, we shall see that these differences are only manifest at very low temperatures. Without invoking the full machinery of quantum statistical mechanics, we can still get a general sense for this behavior by examining the ground states of both systems. At zero temperature, Bosons will fully accumulate in the lowest energy level, while Fermions "stack up", each occupying a distinct energy level (see Figure 1-1). The fact that every boson occupies the same quantum mechanical state hints at the strange nature of Bose-Einstein Condensates (BEC). More surprisingly though, we'll see that the macroscopic occupation of the ground state persists even as we raise the temperature.

Taking into account the quantum statistics for Bosons and Fermions, it is a

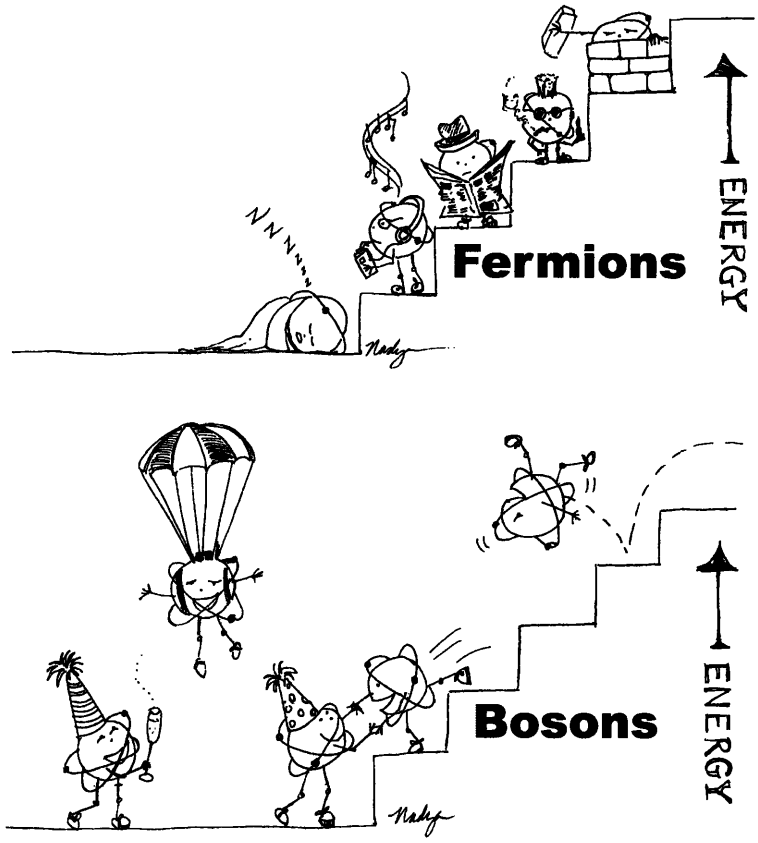

Figure 1-1: The "social nature" of Fermions and Bosons. Fermions are individualists, and refuse to mingle with one another (Pauli exclusion). Bosons are quite the opposite, enjoying each others company (Bosonic enhancement). *Illustration by Nadya Abo-Shaeer.*

straightforward affair to calculate the occupancy of a state of energy ϵ [48]:

$$< N(\epsilon) >_{m-b} = e^{-(\epsilon-\mu)/kT}, \; Maxwell - Boltzmann\ Distribution \quad (1.10)$$

$$< N(\epsilon) >_{b-e} = \frac{1}{e^{(\epsilon-\mu)/kT} - 1}, \; Bose - Einstein\ Distribution \quad (1.11)$$

$$< N(\epsilon) >_{f-d} = \frac{1}{e^{(\epsilon-\mu)/kT} + 1}, \; Fermi - Dirac\ Distribution \quad (1.12)$$

where μ is the chemical potential. We note that at high temperatures ($(\epsilon - \mu) \gg kT$) both distributions approach the classical limit given by the Maxwell-Boltzmann distribution. The differences between Bosons and Fermions are only manifest for

occupations $< N(\epsilon) >$ on the order of unity.

1.4 Bose-Einstein Condensation

At this point we leave Fermions behind and turn our full attention to Bosons.[2] Because it is well-known derivation, I will forego calculating the BEC transition temperature T_c, and simply state the result [48][3]

For free particles

$$k_B T_c = \frac{h^2}{2\pi m}\left(\frac{N}{\zeta(3/2)V}\right)^{2/3}, \tag{1.13}$$

where V is the size of the system and $\zeta(3/2) \approx 2.612$ is the Riemann Zeta function.

For harmonically confined atoms (as is the case for typical atom traps)

$$k_B T_c = \hbar\bar{\omega}\left(\frac{N}{\zeta(3)}\right)^{1/3}, \tag{1.14}$$

where $\zeta(3) \approx 1.202$ and $\bar{\omega} = (\omega_x\omega_y\omega_z)^{1/3}$.

A more intuitive picture for the onset of condensation relies on wave-function overlap. Only then will the particles' indistinguishability come into play. This occurs when the thermal de Broglie wavelength λ_T is roughly equal to the interparticle spacing $n^{-1/3}$, where n is the particle density, such that

$$n\lambda_T^3 \sim 1 \tag{1.15}$$

Aside from a numerical constant, this reproduces the results of Eq(1.13) and Eq(1.14)

[2]This is not due to a lack of interesting phenomena. One need only go two doors down from our lab to prove this.

[3]One integrates over the Bose-Einstein distribution to find the total number of thermally excited particles. This result is then subtracted from the total number of particles in the system, yielding the occupation of the ground state.

1.4.1 The Effect of Interactions

In the ultracold regime ($\sim 1\ \mu$K) atomic interactions are dominated by s-wave scattering. Here, the two-body Hamiltonian $V(\vec{r}_1, \vec{r}_2)$ can be approximated by the local Hamiltonian [81]

$$V(\vec{r}_1, \vec{r}_2) = \frac{4\pi\hbar^2 a}{m}\delta(\vec{r}_1 - \vec{r}_2) \tag{1.16}$$

where m is the atomic mass and a is the s-wave scattering length. The precise value of a depends on details of the interatomic potential, and very small changes can produce dramatic variation. The fact that the interaction strength depends critically on this single parameter a has very important consequences (see Chapter 6).

Interactions play an essential role in evaporative cooling and thermalization. As we shall see, they also also define the ground state characteristics of a BEC. Furthermore interactions lead to such phenomena as superfluidity, molecule creation, and nonlinear atom optics. (The subjects of this thesis.)

1.4.2 The Gross-Pitaevskii Equation

To construct a Schrödinger equation for a zero-temperature BEC we need to include the effect of the binary interactions discussed above. From Eq(1.16) we see that a test particle moving through a system with density n will have mean-field energy

$$\frac{4\pi\hbar^2 a}{m}n \tag{1.17}$$

Therefore, the wave equation takes on a nonlinear form given by

$$\left(-\frac{\hbar^2}{2m}\nabla^2 + V_{ext}(\vec{r}) + \frac{4\pi\hbar^2 a}{m}|\psi(\vec{r})|^2\right)\psi(\vec{r}) = \mu\psi(\vec{r}), \tag{1.18}$$

where $V_{ext}(\vec{r})$ is the external trapping potential, and $n = |\psi(\vec{r})|^2$. Thus, the many-body ground state is described by the macroscopic order parameter (wavefunction)

$$\Psi(\vec{r}, t) = \psi(\vec{r})e^{-i(\mu/\hbar)t} \tag{1.19}$$

Because the interaction energy of a condensate typically dominates its kinetic energy (the Thomas-Fermi regime), we may omit the kinetic energy from Eq(1.18), yielding

$$\left(V_{ext}(\vec{r}) + \frac{4\pi\hbar^2 a}{m}|\psi(\vec{r})|^2\right)\psi(\vec{r}) = \mu\psi(\vec{r}) \qquad Thomas - Fermi\ Limit \tag{1.20}$$

From here it is trivial to see that the density is given by

$$n(\vec{r}) = |\psi(\vec{r})|^2 = \frac{m}{4\pi\hbar^2 a}[\mu - V(\vec{r})] \tag{1.21}$$

and we arrive at the well-known result that the condensate density takes on the inverse profile of its trap (typically a parabola).

1.5 Outline of the Thesis

I had the benefit of arriving to the New Lab just six months after their first BEC. Although our machine has undergone many changes in the past five years, the basics remain the same. Because our apparatus has been well-documented previously [27, 62], I will omit this discussion in favor of more unique material. In particular, I include two tutorial chapters on vortex production and Bragg diffraction, which I hope will prove useful to my successors.

A major portion of my work at MIT has been devoted to the study of quantized vortices. Chapter 2 is intended as a primer for the basic theory and experimental techniques underlying vortex physics. Chapters 3-5 detail our studies of nucleation and dynamics of vortex lattices. More recently, I have worked on cold molecules created via Feshbach resonance. Chapter 6 explains the motivation for creating cold molecules, along with our initial experimental results. Chapter 7 is devoted to techniques of Bragg spectroscopy, which were important for our demonstration of coherent molecular optics (Chapter 8).

Finally, having spent the last five years of my life working on the 2nd floor of Building 26, I have had the pleasure of sharing in many triumphs and an equal

number of defeats. With this in mind, I will to try to convey some of the excitement we've felt, whether it be over something meaningful or something mundane.

This thesis is by no means a complete survey of Bose-Einstein Condensation. Indeed, the field has grown so rapidly in my time at MIT that I cannot even do justice to my particular areas of expertise. Fortunately, a large body of work already exists. In particular, I refer readers to the following useful references:

- *Bose-Einstein Condensation in Atomic Gases*
  Proceedings of the International School of Physics Enrico Fermi, Course CXL
  Edited by M. Inguscio, S. Stringari and C.E. Wieman (1999) Ref [49]

- *Bose-Einstein Condensation in Dilute Gases*
  C.J. Pethick and H. Smith (2002) Ref [81]

- *Laser Cooling and Trapping*
  H. Metcalf and P. van der Straten (1999) Ref [71]

In addition, a wealth of practical knowledge lies in the theses of my predecessors.

Chapter 2

Vortices in Bose-Einstein Condensates

...the well-known invariant called the hydrodynamic circulation is quantized; the quantum of circulation is h/m.

-Lars Onsager, on the behavior of a Bose gas at zero temperature. (1949)

As we shall see, this statement has very profound implications. The fact that Bose-condensed systems can be described by a macroscopic order parameter Ψ puts important restrictions on the way these fluids flow. The requirement that Ψ be single-valued (Figure 2-1) leads directly to Onsager's conclusion. When these "superfluids" are rotated, angular momentum can only enter the system in the form of discrete line defects.

I begin this chapter with a brief (and humble) explanation of the basic principles of vortices in BEC. As an obligation to my successors, I finish with a discussion of the "nuts and bolts" of vortex lattice generation. Chapters 3-5 are dedicated to the experimental study of vortices in superfluid systems.

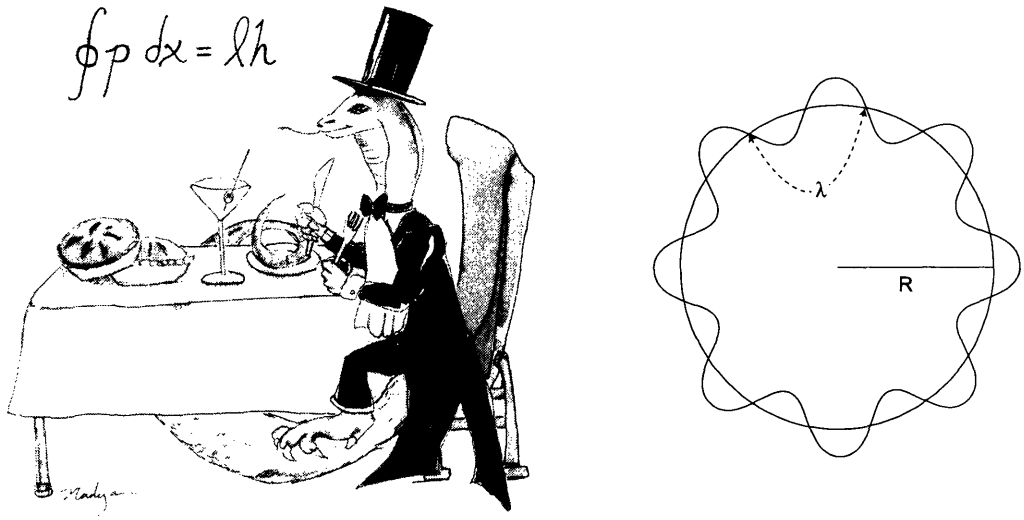

Figure 2-1: Uroboros dining on his tail. The Bohr-Sommerfeld Quantization condition requires that an integer number of wavelengths fit within any closed loop. This insures that the wavefunction is single-valued. *Illustration by Nadya Abo-Shaeer.*

2.1 Vortices - Simple Theory

The theory of vortex nucleation, dynamics, interactions etc. has been the subject of exhaustive study, first in liquid helium systems [26] and later for BEC [33]. While atomic BEC is in some ways fundamentally different from liquid helium (inhomogeneous density, weaker interactions), the similarities between the two systems has facilitated rapid theoretical development. One unifying feature of these two fields is that most of the theory is beyond my comprehension. With this in mind, I leave the details to the theorists, and present a phenomenological description of superfluid vortices.

In Chapter 1 we saw that the static properties of a zero-temperature dilute Bose gas are characterized by the time-independent Gross-Pitaevskii (G-P) equation (Eq(1.18)). To study the dynamic properties of the system, we must invoke the

time-*dependent* G-P equation

$$i\hbar\frac{\partial}{\partial t}\Psi = \left(-\frac{\hbar^2}{2m}\nabla^2 + V_{ext} + U_0|\Psi|^2\right)\Psi \tag{2.1}$$

where $U_0 = 4\pi\hbar^2/a$. To better represent the flow characteristics it is instructive to recast this equation in an equivalent quantum-hydrodynamical form. Multiplying through by Ψ^* yields

$$i\hbar\Psi^*\frac{\partial}{\partial t}\Psi = -\frac{\hbar^2}{2m}\Psi^*\nabla^2\Psi + V_{ext}|\Psi|^2 + U_0|\Psi|^4 \tag{2.2}$$

Subtracting Eq(2.2) from its complex conjugate yields

$$i\hbar\left(\Psi^*\frac{\partial}{\partial t}\Psi + \Psi^*\frac{\partial}{\partial t}\Psi\right) = \frac{\hbar^2}{2m}\left(\Psi\nabla^2\Psi - \Psi^*\nabla^2\Psi^*\right) \tag{2.3}$$

or more succinctly

$$\frac{\partial}{\partial t}|\Psi|^2 = \frac{\hbar}{2mi}\nabla\cdot(\Psi^*\nabla\Psi - \Psi\nabla\Psi^*) \tag{2.4}$$

Re-expressing Eq(2.4) as

$$\frac{\partial}{\partial t}n + \nabla\cdot(n\vec{v}) = 0 \tag{2.5}$$

helps to identify this as a continuity equation for compressible flow, where $n = |\Psi|^2$ is the fluid density and the fluid velocity is given by

$$\vec{v} = \frac{\hbar}{2mni}(\Psi^*\nabla\Psi - \Psi\nabla\Psi^*) \tag{2.6}$$

Without loss of generality, the order parameter can be expressed in terms of an amplitude and phase $\Psi = \sqrt{n}e^{i\phi}$ such that

$$\vec{v} = \frac{h}{m}\nabla\phi \tag{2.7}$$

Thus, we identify the velocity of the condensate with the gradient of the phase. The fact that the velocity is field conservative (known as potential flow) places restrictions

on the fluid motion. Provided that ϕ is not singular

$$\nabla \times \vec{v} = 0 \tag{2.8}$$

and the flow is irrotational. More generally, for the wavefunction to be single-valued, the phase accumulated around a closed loop must be an integer multiple of 2π.

$$\Delta\phi = \oint \nabla\phi \cdot d\vec{l} = 2\pi \tag{2.9}$$

This is just a restatement of the Bohr-Sommerfeld quantization condition (Figure 2-1). The circulation C around a closed loop is thus

$$C = \oint \vec{v} \cdot d\vec{l} = \ell\frac{h}{m} \tag{2.10}$$

and we arrive at Onsager's statement that circulation is quantized in units of $\kappa = h/m$. In general,

$$\nabla \times \vec{v} = \ell\frac{h}{m}\delta(\vec{r})\hat{z} \tag{2.11}$$

To demonstrate the implications of quantized circulation, we recognize from Eq(2.10) that the radial velocity profile is

$$v_r = \ell\frac{\kappa}{2\pi r} \tag{2.12}$$

Because the energy diverges at the origin, the density must go to zero there. Fluid is expelled, and a hole appears in the liquid. The size of this hole is determined by the balance of two competing processes. Mean-field repulsion seeks to fill in the hole, but the requirement of zero density at the core places a hard wall at the center. Therefore, we must balance the mean-field's desire to fill the hole with the kinetic "cost" of bending the wavefunction (recall that kinetic energy is given by the curvature of the wavefunction). For a feature of size ξ, the kinetic energy per particle is roughly $\hbar^2/2m\xi^2$. The size of the core is then determined by

$$\frac{\hbar^2}{2m\xi^2} = nU_0 \tag{2.13}$$

Thus, the characteristic size of the vortex is,

$$\xi = \frac{1}{\sqrt{8\pi n a}} \tag{2.14}$$

which is typically called the "healing length". In passing, we note that the flow velocity (Eq(2.12)) at the core (r=ξ) is equal to the local speed of sound c

$$c = \sqrt{\frac{2nU_0}{m}} \tag{2.15}$$

We conclude with a few remarks on the bulk properties of systems containing many vortices. In the limit of very high angular momentum, the quantum system will mimic the behavior of a classical fluid. That is, the "course-grained" flow field of the quantum fluid is identical to the rigid-body rotation of a classical fluid (Figure 2-2). Intuitively we know this must be true, because at some point the quantum and classical pictures must match up (Bohr correspondence principle). Now, using a well-known result from classical fluid dynamics for the kinetic energy per unit length of a hollow vortex of radius a and circulation C [26]

$$E = \int_a^{r_0} \frac{1}{2}\rho v^2 dr^2 = \frac{\rho C^2}{4\pi} ln \frac{r_0}{a} \tag{2.16}$$

we find that for a superfluid $E = (\rho \ell^2 \kappa^2 / 4\pi) ln(r_0/\xi)$. Because this energy is quadratic in the vortex winding ℓ, multiply charged vortices are unstable and will decay into vortices of unit circulation.[1] Due to this repulsive vortex-vortex interaction, we might expect vortices will distribute themselves in some sort of array to minimize energy. Indeed, numerical simulations [4, 98], followed by experiment [109, 67, 2] have proven this to be the case, with the lattice taking on a triangular configuration.

Lastly, we note that the angular momentum per particle a distance r from the origin is $mvr = \ell\hbar$. For rigid-body rotation $v = \Omega r$, where Ω is the (angular) rotation frequency. Now, a closed loop around the origin will encircle N vortices. Therefore,

[1] This result is also evident from Eq(2.12). The flow velocity is linear in vortex winding ℓ, therefore the kinetic energy is proportional to ℓ^2.

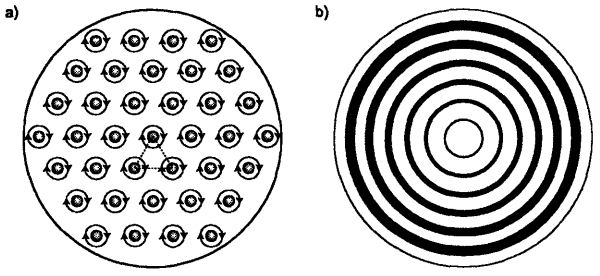

Figure 2-2: Bulk lattice flow fields. a) A system containing many vortices will arrange itself in a triangular lattice to minimize energy. b) The coarse-grained flow field of the lattice mimics rigid-body rotation.

the vortex density $N/2\pi r^2$ in the bulk is

$$n_v = \frac{2\Omega}{\kappa}. \tag{2.17}$$

2.2 Vortex Lattice Tutorial

When the New Lab began its effort to produce vortices the nucleation process was still somewhat mysterious (see Chapter 4). Indeed, we tried for 3-4 months before obtaining our first signal. Later, I witnessed Aaron Leanhardt go through similar struggles in his effort to imprint vortices topologically [65]. In both cases the difficulty was not in setting-up the experiment, but rather finding the proper parameter space to work in. In retrospect, we both agree that once you know where to look, making vortices is actually quite easy. Thus, the impetus for this section is to provide the reader with a "fool-proof recipe" for making vortices.[2] Many of the past techniques used by our group and others are needlessly complicated, and in some cases misleading. I will try to pare down the process to only its most essential elements.

The courage to write this section stems from my work with Martin Zwierlein during my final few months in lab. I made a promise to the Lithium Lab that I would "bring over the vortices" before I left. In my bravado, I also made strong claims

[2]Disclaimer: The information contained herein is provided as a public service with the understanding that the author makes no warranties, either expressed or implied, concerning the accuracy, completeness, reliability, or suitability of the information.

about the ease with which it would be done. Finally, I was forced to deliver on my claims, and as luck would have it, it was much easier than I had anticipated. The entire process took less than a day and it gave me confidence in the transferability of the techniques outlined below.

2.2.1 The Rotating Bucket

Vortices are created by rotating the condensate about its symmetric axis. We have made vortices in a variety of different "buckets", with aspect ratios varying from 2 to 30. However, it is wise to choose a smaller aspect ratio for two reasons:

1) Vortices are 3-dimensional objects. They can twist and bend. This behavior reduces imaging contrast. In addition, if the imaging axis is tilted with respect the condensate axis, the reduction in contrast is more severe for longer clouds. In our first two papers we used a "slicing" technique to image only the center of the condensate [2, 83]. However, the necessity of this technique is probably overstated a bit. It is only essential for imaging small numbers of vortices or vortices created in very long traps.

2) Smaller aspect ratios correspond to a larger radial size. Larger objects are less sensitive to stirrer alignment and therefore much easier to get rotating.

I prefer an aspect ratio of ~ 4, mostly because our Ioffe-Prtichard-type magnetic traps tend to be less round below these values (due to trap imperfections and gravitational sag). One should try to work in a regime where the trap is as round as possible. However, my definition of round is somewhat arbitrary. For instance, JILA's top trap is round to 1 part in 2000, while most of our work was done in a trap with asymmetry $\epsilon_r = (\omega_x^2 - \omega_y^2)/(\omega_x^2 + \omega_y^2) = 6.4\%$.

2.2.2 The Swizzle Stick

The condensate is stirred using the optical dipole force created by a detuned laser beam.

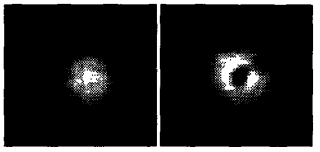

Figure 2-3: Bullseye. Alignment of the stirrer using *in situ* phase contrast imaging. The beam power exceeds the chemical potential of the condensate so atoms are fully expelled from the center.

The size of the stirring beam should be small compared to the size of the condensate!

Much of the mystery that surrounded early work on vortex nucleation stemmed from inefficient coupling of angular momentum to the condensate. The big beam "Rotating Bucket" approach only works well near the surface mode resonance. As demonstrated in Chapter 4, a small stirrer is efficient at coupling angular momentum to the condensate at all frequencies. If you are wedded to the rotating bucket analogy, think of the small beams as roughness on the surface of an otherwise smooth bucket (magnetic trap).

Because we are using small beams, a blue-detuned beam is necessary because it creates a repulsive potential. A red-detuned beam will act as an optical trap. The stirrer should be made as small as possible for the greatest flexibility. Gaussian beam waists ($1/e^2$) of 5 μm should be relatively easy to attain. Beam profile is not critical. The intensity of the stirrer should be enough to overcome the chemical potential μ of the condensate, such that the beam fully pierces the condensate (Figure 2-3).

The technical question that most often arises relates to how the stirring beam is actually rotated. The method is quite simple. The beam becomes a "swizzle stick" by passing it through a two-axis acousto-optic deflector. By frequency modulating the two channels 90° out-of-phase, the (1,1) order will rotate. The method is outlined in Figure 2-4. It is preferable to use two spots rather than one because symmetric stirring will induce less dipole oscillation. A lens *must* be placed a focal length

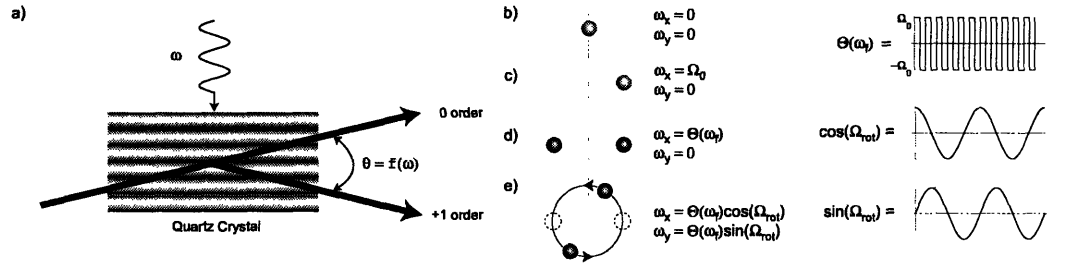

Figure 2-4: Optical "Swizzle" Stick. a) Light traveling through a quartz crystal can be deflected from its path by an acoustic wave. The acoustic wave creates a density modulation in the crystal off which the beam can Bragg scatter. The angle at which the beam is scattered is proportional to the acoustic wave drive frequency ω. b) For (ω_x, ω_y)=(0,0) the beam is undeflected. c) When (ω_x, ω_y)=$(\Omega_0, 0)$ the beam is deflected by a fixed amount. d) A fast square pulse will split the beam in two. This frequency should be much faster than the trap frequencies so that the condensate sees a time-averaged potential. e) By driving the channels 90° out-of-phase, the two beams rotate in space. The amplitude and frequency of rotation are Ω_0 and Ω_{rot}, respectively.

away from the deflector in order to image the separated beams onto condensate.[3] Course alignment of the beam can be done using mirrors after the deflector. Fine adjustments can then be made by changing the center frequency of each deflector. The final alignment should be made using the condensate as a guide. It is preferable here to use *in situ* phase-contrast imaging [57] to center the beam (see Figure 2-3). However, the alignment can also be done using absorption imaging by leaving the beam on in short time-of-flight (~2 ms). This is necessary to reduce the optical density.

2.2.3 Stirring it Up

Now that the machinery is in place, we turn our attention to stirring the condensate. Again, phase-contrast imaging is a valuable technique because the stirring can be monitored directly. Figure 2-5 shows a "movie" of the stirring process. As the stirrer

[3]These defelectors are large objects so this is a somewhat ambiguous statement. Getting it close is good enough. As the lens moves out of focus, the deflection sensitivity (beam separation per unit frequency) is degraded.

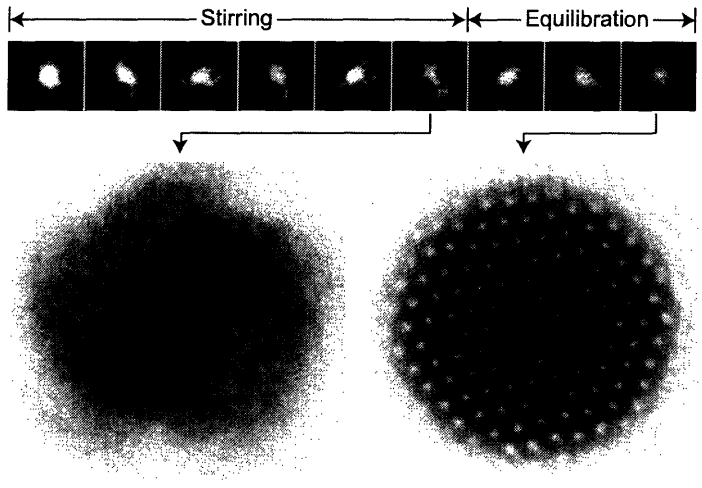

Figure 2-5: Stirring up a Bose-Einstein Condensate. Axial phase contrast images showing the condensate at 4.4 ms intervals. The "smoking gun" for vorticity is the build-up of fluid in front of the stirrer. These images demonstrate both the violent nature of the stirring and the resilience of the condensate. Representative absorption images are also included.

is turned on we see fluid begin to build-up in front of it. The beam is clearly exerting a torque on the condensate. The process may seem too violent, but this is exactly what you would like to see. From Figure 2-5 we see that the condensate is quite able to "heal" itself. One need not ramp up the power or rotation frequency of the stirrer. Simply "slam" on the beams, get angular momentum into the system, get out, and leave it to the condensate to do the rest. There is one caveat: In order for the condensate to heal itself it must have a sink for all the excess energy.

Keep the rf-knife on during equilibration!

In fact, we simply leave the rf-knife on at its final value during the entire process, stirring included.

2.2.4 The Golden Parameters

In my time working on vortices I have noticed that there seem to be universal parameters for making vortices. That is, parameters that work regardless of trap geometry.

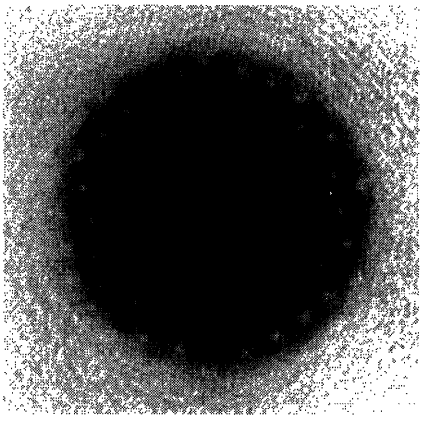

Figure 2-6: "Fool-proof" vortex lattice. Using the techniques outlined in this section, the Lithium lab had over 120 **sodium** vortices in less than a day. Shown here is the first shot.

As mentioned earlier, a lot of the difficulty in making vortices is finding the proper parameter space to work in. These values should provide a good starting point:[4]

Stir Power:	1.5μ
Stirring Time:	200 ms
Stirring Frequency:	$0.85\omega_r$
Stirring Radius:	$0.5R_{TF}$
Equilibration Time	500 ms

Table 2.1: Golden parameters for vortex creation.

In fact, Martin and I used these parameters in our first attempt at vortices and *voila!* (Figure 2-6).[5]

[4]These parameters are not pulled from thin air. Their origin can be found in the following 3 chapters.

[5]I will never forget Martin's reaction when this image appeared on the screen. He was so excited that he temporarily could only speak in German. It was a wonderful reminder of how Chandra and I felt the first time we made vortices.

Chapter 3

Vortex Lattices

Properties of vortex lattices are of broad interest in superfluids, superconductors and even astrophysics. Fluctuations in the rotation rate of pulsars are attributed to the dynamics of the vortex lattice in a superfluid neutron liquid [31, 26]. Here we show that vortex formation, and the subsequent self-assembly into a regular lattice, are robust features of rotating BECs. Gaseous condensates may serve as a model system to study the dynamics of vortex matter.

This chapter supplements work reported in the following publication:

J.R. Abo-Shaeer, C. Raman, J.M. Vogels, and W. Ketterle
"Observation of Vortex Lattices in a Bose-Einstein Condensate,"
Science 292 p.476-479 (2001).
(Included in Appendix A) Ref [2]

3.1 Perspective

When I began my work at MIT in the summer of 1999, one of the major efforts in the field was to demonstrate that BEC was a superfluid. There was not much doubt that this was the case, however the proof was still very important. At the time, two papers simultaneously provided the first evidence for superfluidity. One, from E. Cornell's group at JILA, used a phase-engineering technique to observe quantized

circulation (a vortex) in a two-component condensate [70]. The second, from the New Lab, used a "stirring" beam to demonstrate a critical velocity for the onset of dissipation. A more dramatic demonstration of superfluidity came half a year later from J. Dalibard's group at ENS. Uniting the work of JILA and MIT, the ENS group used a rotating stirrer to generate up to 4 vortices in their condensate [67]. The results were quite stunning. As a consequence of vortex-vortex interactions, the vortices arranged themselves into symmetric arrays. In addition, the vortices were more robust than had been expected, with lifetimes over 1 s.

While our critical velocity results indicated that the dissipative mechanism was indeed vortex creation, our direct entry into vortices did not begin until the summer of 2000. At this time Wolfgang suggested we attempt to image the vortices created via our stirring technique. The prospects were exciting because our experiment had 25 times more atoms than the ENS experiment. My rough calculation predicted we could see as many as 136 vortices.[1] However, we were hoping for around 30, which still seemed very ambitious.

The road leading to the actual observation of vortex lattices was very rocky. Chandra and I spent 3-4 months trying to make vortices. We spent many long nights wondering where the vortices were. Finally, Chandra decided we needed put an end to the experiment. I was disappointed, but I begrudgingly agreed on the condition that we give it one last shot.[2] Methodically, we went through the process of aligning the stirring beams to the condensate. The beam size was tailored to what we believed was the ideal size. The final, and most crucial, step was to verify that the condensate was actually rotating.

The mistake we made from the outset was to assume that a larger set of stirring beams (similar to ENS's set-up) would be superior to a small stirrer (similar to our critical velocity set-up) for making vortices. We thought that it was probably better to gently rotate the entire fluid, rather than to simply tear through a section of

[1] My methods for arriving at this value were primitive and lacked any physical understanding of vortices. I was clever enough to recognize that this number was too high. Under the calculation I noted "This is Ridiculous!" Ironically, for quite awhile our record number of vortices stood at 134.

[2] I agreed recognizing that Chandra was soft-hearted and would probably have continued with the experiment so as not crush me.

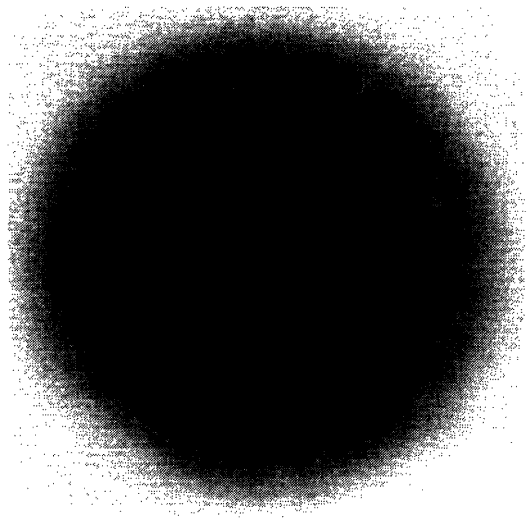

Figure 3-1: First signal of vortices. The best image from the night we observed vortices.

it. As we will see in Chapter 4, large beams are only effective at stirring over a narrow frequency range, corresponding to the surface mode resonance [78]. In our past attempts to stir we chose our frequency arbitrarily. This time we set our stirring frequency to the surface mode frequency and observed *in situ* that our condensate was rotating (See ref.[78] for an explanation of how this is done.). When we released the condensate from the trap, we noticed a marked difference from our past attempts to stir. The surface of the condensate was very rough, possibly due to vortices. After another few shots we had convinced ourselves that they were indeed vortices. Our best image that night was no thing of beauty (see Figure 3-1). Nonetheless, I was able to count around 30 vortices in the image. Chandra and I were overjoyed.[3] The next day we were surprised to find that by varying the stirring parameters a bit and allowing 500 ms of equilibration time after the stir, a beautiful lattice of (85) vortices formed. Our next two weeks in lab are the subject of the present chapter.

As a side note, prior to the work at ENS, vortex physics (in BEC) was driven mainly by theory. Indeed, JILA's method for observing the first vortex came from a

[3]I regret that were unable to share in this excitement with our former colleague Roberto Onofrio, who had completed his tour in the lab 6 months earlier. His work in the the New Lab helped to motivate this study.

theoretical proposal by Williams and Holland [105]. Most theory at this time focused on systems of one or two vortices. (Because vortices had proven so difficult to create, it might have seemed too ambitious to consider systems with many.) The experimental results of ENS and our lab surpassed expectation. Theorists were forced to play catch up, developing new tools to model the *bulk properties* of vortices. However, the theorists fought back,[4] proposing new experiments requiring as many vortices as particles [47]. Our current experiment is still 99,999,828 vortices away from this regime, which should give theorists plenty of time to catch their breath.

3.2 Observation of Vortex Lattices

A detailed description of our observation of vortex lattices can be found in Appendix A. Here I will only highlight important results that set the foundation for future studies.

The main result (Figure 3-2) shows highly-ordered triangular lattices of variable vortex density containing up to 130 vortices. Such "Abrikosov" lattices were first predicted for quantized magnetic flux lines in type-II superconductors [4]. A slice through images shows the visibility of the vortex cores (Fig. 3-3), which was as high as 80%. The lattice had a lifetime of several seconds, with individual vortices persisting up to 40 s. We can estimate from Eq(2.15) that during its lifetime, the superfluid flow field near the central vortex core had completed more than 500,000 revolutions and the lattice itself had rotated approximately 100 times.

At the time, this represented a marked improvement for superfluid vortices. Prior to this work, the direct observation of vortices had been limited to small arrays (up to 11 vortices), both in liquid ^{4}He [108] and in rotating gaseous Bose-Einstein condensates (BEC) [67, 68]. This new regime enabled us to explore the properties of bulk "vortex matter", including dynamics, local structure, defects, and long range order.

A remarkable feature of these lattices is their extreme regularity, free of any major

[4] An alternate view is that the dramatic strides made them overly optimistic.

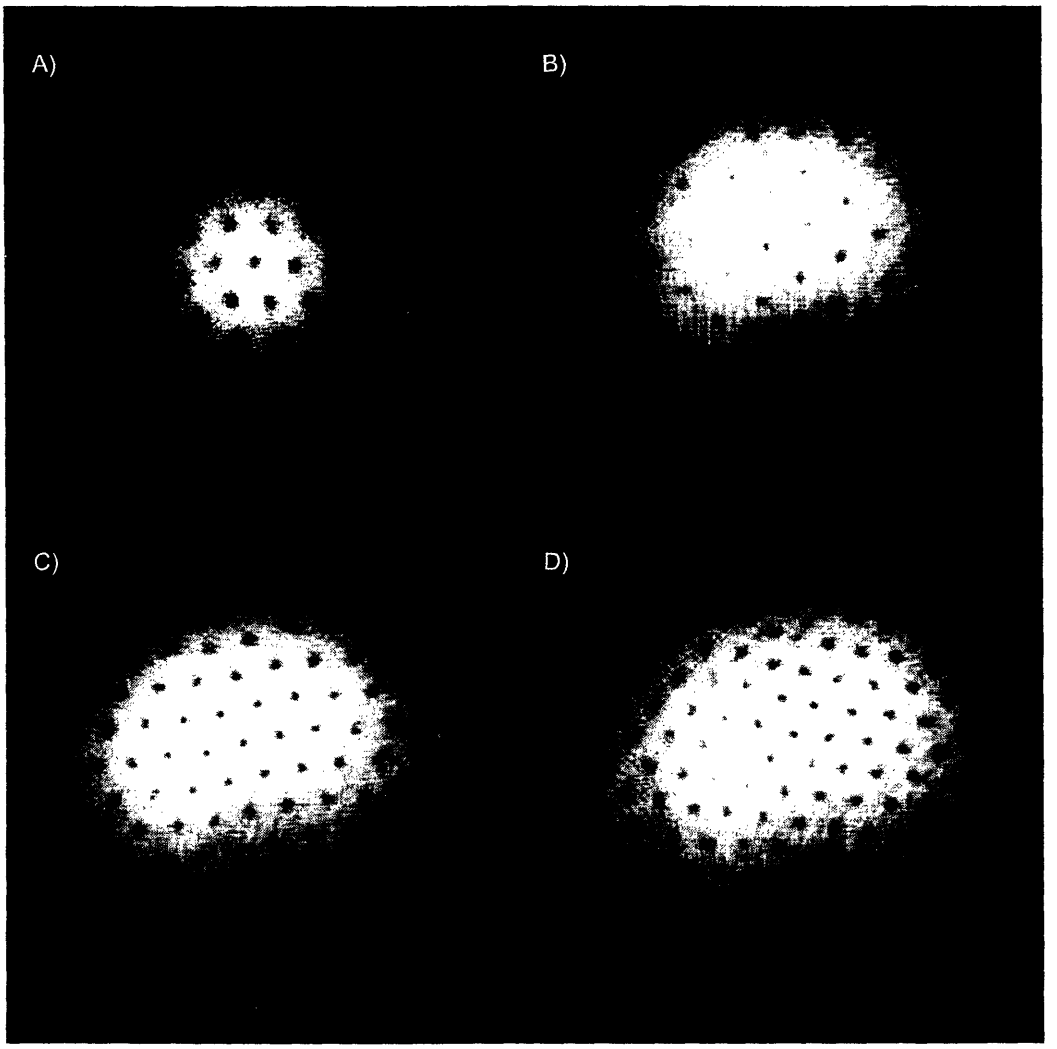

Figure 3-2: Observation of vortex lattices. The examples shown contain (A) 16 (B) 32 (C) 80 and (D) 130 vortices. The vortices have "crystallized" in a triangular pattern. The diameter of the cloud in (D) was 1 mm after ballistic expansion which represents a magnification of 20.

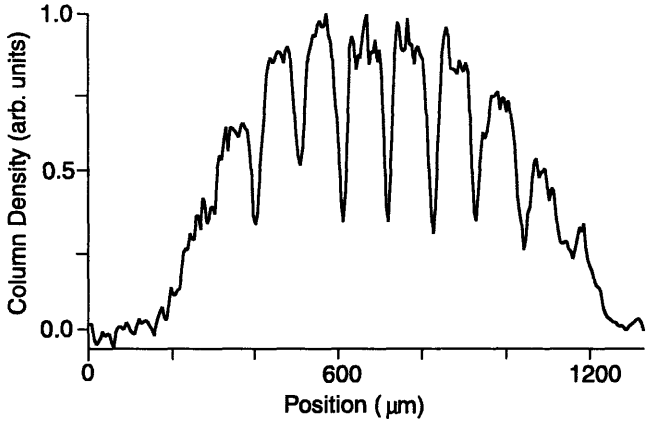

Figure 3-3: Density profile through a vortex lattice. The curve represents a 5 μm wide cut through a 2D image similar to those in Fig. 3-2 and shows the high contrast in the observation of the vortex cores.

distortions, even near the boundary. This was a very surprising result for three reasons:

1) *The condensate density is inhomogeneous.* Why then should this not distort the radial symmetry?

2) *The condensate has a hard boundary.* Why are no edge effects manifest?

3) *Numerical simulations under more ideal conditions (uniform density, infinite system) show distortion.* Campbell and Ziff [13] tell us that in an infinite system of uniform density, a configuration with perfect triangular symmetry can lower its energy by rearranging the outermost rings of vortices into circles (see Figure 3-4).

This third reason only added to our bewilderment. Was nature really conspiring *with* us?[5] In a way it was comforting to see images like that in Figure 3-4c. Indeed, we did observe more complex lattice configurations in a fraction of the images. Some show patterns characteristic of dislocations (Fig. 3-5a), grain boundaries (Fig. 3-5b), and partial crystallization (Fig. 3-6b).

[5]I didn't want to look a gift horse in the mouth, but times like this made me question whether Chandra had made a deal with the Devil. Only time will tell.

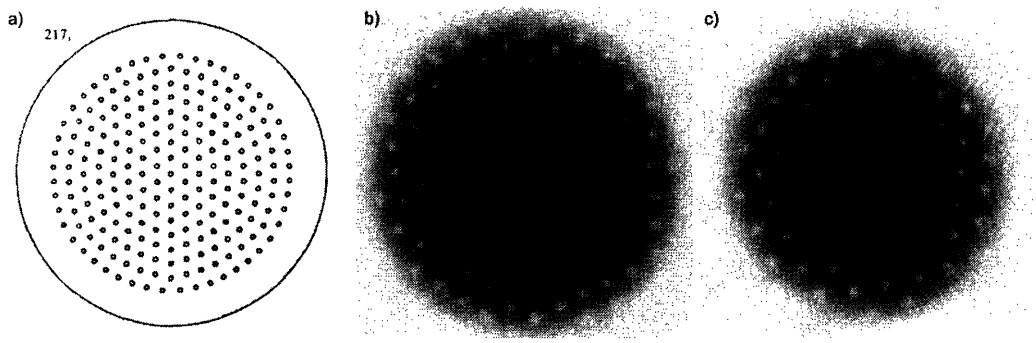

Figure 3-4: Structure of a vortex lattice. a) Numerical Simulation of the lattice structure in an infinite system with uniform density (taken from Ref[13]). The outermost vortices lower the energy of the system by shifting slightly off-site. b) The real-world situation is typically free of distortion. c) However, not every lattice is perfectly triangular. (We now recognize these types of features as collective modes of the lattice. More on this in Chapter 5.)

3.3 Formation and Decay of a Vortex Lattice

The feature of our work that most fascinated me was the crystallization process (Figure 3-6). It is quite remarkable that such a turbulent system can relax into a perfect lattice. The mechanism that "freezes out" the vortices was quite mysterious then, and is still somewhat today. An in-depth analysis of this process is the subject of Chapter 5.

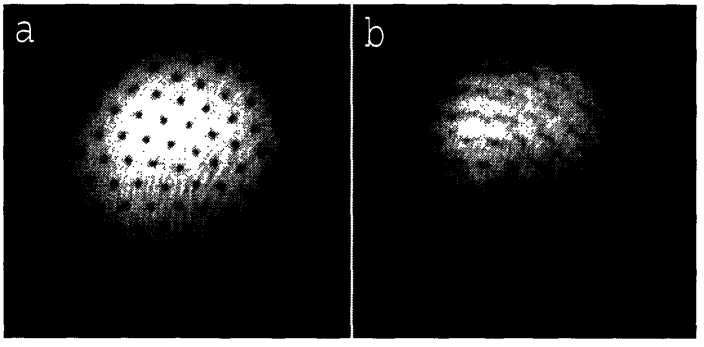

Figure 3-5: Vortex lattices with defects. In (A) the lattice has a dislocation near the center of the condensate. In (B) there is a defect reminiscent of a grain boundary.

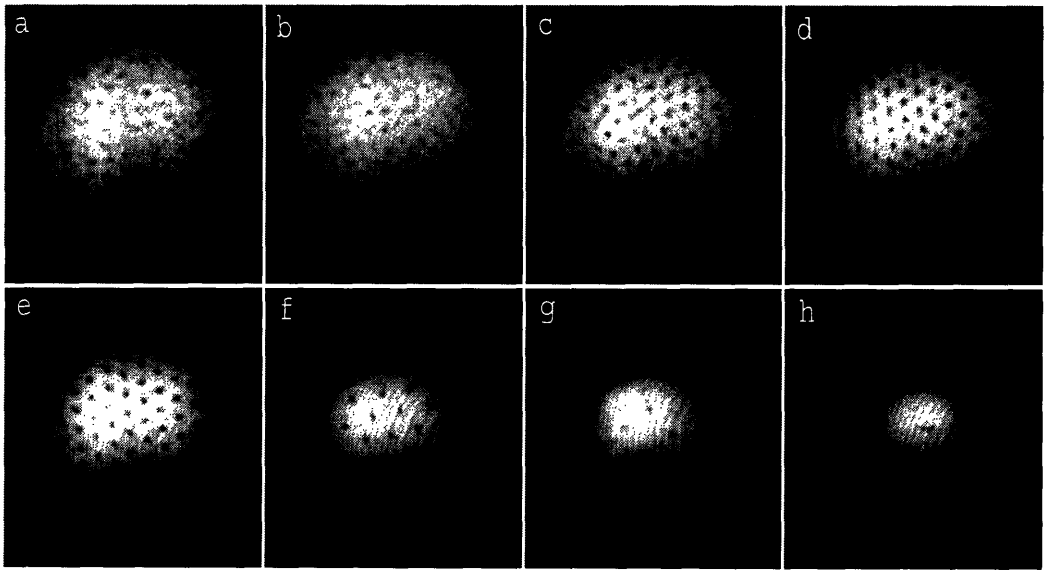

Figure 3-6: Formation and decay of a vortex lattice. The condensate was rotated for 400 ms and then equilibrated in the stationary magnetic trap for various hold times. (A) 25 ms (B) 100 ms (C) 200 ms (D) 500 ms (E) 1 s (F) 5 s (G) 10 s (H) 40 s. The decreasing size of the cloud in (E)-(H) reflects a decrease in atom number due to inelastic collisions. The field of view is approximately 1 mm $\times$ 1.15 mm.

Chapter 4

Vortex Nucleation

Since the realization of BEC in 1995, the nature of quantized vortices has been the subject of much debate within the community. The first questions centered on creation and detection of vortices. How does one put angular momentum into the system? How would vorticity manifest itself? Initial difficulties in creating vortices led many to question whether they were even stable. While work at JILA showed promise [70], all doubts were laid to rest by the pioneering work of the ENS group [67]. However, their work did raise new questions, specifically about the anomalously high critical frequency for nucleation. It is at this point that this chapter picks up.

This chapter supplements work reported in the following publication:

C. Raman, J.R. Abo-Shaeer, J.M. Vogels, K.Xu, and W. Ketterle

"Vortex Nucleation in a Stirred Bose-Einstein Condensate,"

Phys. Rev. Lett. 87 210402 (2001).

(Included in Appendix B) Ref [83]

4.1 Perspective

Work in this chapter was borne out from the desire to reconcile the results of our studies of critical velocity [84, 79] with our work on quantized vortices [2]. Even before we had actually observed vortices, we were confident that the critical velocity

we measured could be attributed to the creation of vortices. Indeed, numerical simulations of our system predicted the appearance of vortex pairs at a critical velocity very close to what we had observed [52]. These simulations relied on an energetic argument given by the Landau criterion, which states that above a certain stirring velocity excitations are energetically possible. The Landau critical velocity is given by [48]

$$v_c = \min_p(\epsilon_p/p). \tag{4.1}$$

where ϵ_p is the energy of the excitation with momentum p. However, initial results by the ENS group [67] seemed to indicate that vortices were nucleated only at rotational frequencies much *higher* than those expected from the Landau criterion. At the time this was a confusing result, and several ideas were proposed to explain it [30, 35], including tunnelling barriers that required a higher rotation frequency to stabilize the vortex. However, the ENS group correctly recognized that this discrepancy was actually due to the stirring process itself. Their idea was that vortices were formed via a dynamic instability (breakdown) of a surface wave. Surface mode resonances occur at $\omega_r/\sqrt{\ell}$, where ω_r is the radial trap frequency, and ℓ is the polarity of the mode. Therefore, because their two-point stirrer could only efficiently drive the $\ell = 2$ surface mode, this is the only region where they could produce vortices. However, stirrers of higher polarity should generate vortices at lower frequencies until the Landau criterion is met.

$$\Omega_s = \min_l(\omega_r/\sqrt{l}). \tag{4.2}$$

Expressed here in terms of critical rotation frequency, but formally equivalent to Eq(4.1).

In our first paper we observed this same resonant production, however we also showed that vortices could be generated at much lower frequencies than $\omega_r/\sqrt{2}$, simply by driving the surface mode off resonance (essentially power broadening it) [2]. However, the number of vortices we observed was always much smaller than the equilibrium value corresponding to rigid-body rotation.

In the present work we demonstrate that increasing the polarity of the stirrer does

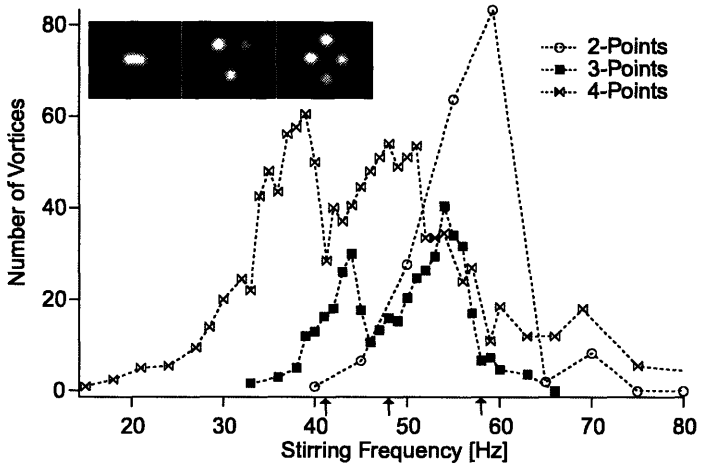

Figure 4-1: Discrete resonances in vortex nucleation. The number of vortices created by multi-point patterns is shown. The arrows below the graph show the positions of the surface mode resonances $\omega_r/\sqrt{l}$. Inset shows 2-,3-, and 4-point dipole potentials produced by a 25 μm waist laser beam imaged onto the CCD camera.

indeed lower the frequency at which the maximum number of vortices are produced (Figure 4-1). More importantly, we demonstrate that the "global" surface wave resonances are not a necessity for creating vortices. Rather, they only act as an efficient means for coupling angular momentum into the system. The proof of this comes when we reduce the size of the stirring beams. In this case we no longer address the condensate globally. Rather, vortices are generated via *local* instabilities. As expected from our work on critical velocity, the number of vortices produced in this regime simply increases linearly with rotation frequency (velocity).

As is often the case, what was once very confusing, is obvious in retrospect. Vortices can be generated both locally, and globally, but the two mechanisms are fundamentally the same. At the time, this work went a long way in demystifying the vortex making process. Indeed, we found that not only was it not necessary to drive the surface modes, it was actually an inferior scheme to creating the vortices locally. Our findings can be summed up succinctly by two statements, one attributed to James Anglin, and the other to Wolfgang Ketterle.[1]

[1]These statements must be qualified. They only relate to vortices generated via *stirring*. Vortices created using phase-engineering techniques [70, 65] need not meet these requirements.

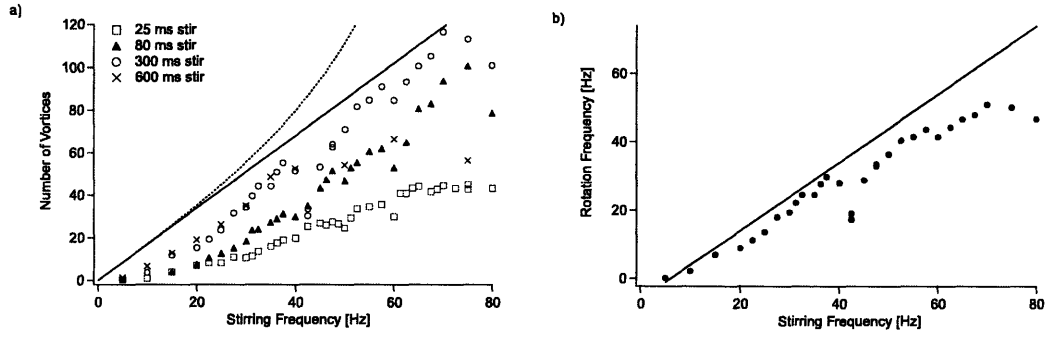

Figure 4-2: Nonresonant nucleation using a small stirrer. a) Average number of vortices created using a 2-point pattern positioned at the edge of the condensate. b) Effective lattice rotation frequency. The lines in both graphs indicate the rigid-body limit (shifted to account for the critical velocity for nucleation.)

- ***Vortices are generated at surfaces!*** Whenever questions arose about the difference between local and global vortex excitation, James would emphatically make this statement. At the time it seemed a bit reductionist to me. Now I cannot decide whether it is profound or trivial. In essence the statement is this: There is no *a priori* reason to believe that vortices can only be generated at the Thomas-Fermi surface of the condensate. The surface created by a small stirrer passing through the condensate is just as good.

- ***Vortices are generated by surface instabilities.*** Wolfgang was fond of making this statement in talks while showing the slide in Figure 4-3. It is essentially a restatement of the Landau criterion: above a certain critical velocity, the flow at the surface becomes turbulent and breaks apart into vortices.

4.1.1 A Brief Aside...

The resonances in Figure 4-1 were close to the frequencies of excitation of l =2, 3 and 4 surface modes ($\omega_l/l = \omega_r/\sqrt{l}$) [19]. A second, higher resonance appeared in the 3- and 4-point data. We originally postulated that this structure "*could be due to additional coupling to the quadrupole ($l = 2$) mode caused by misalignment of the laser beams [16]. The extra peaks and the shift of the resonances from the frequencies*

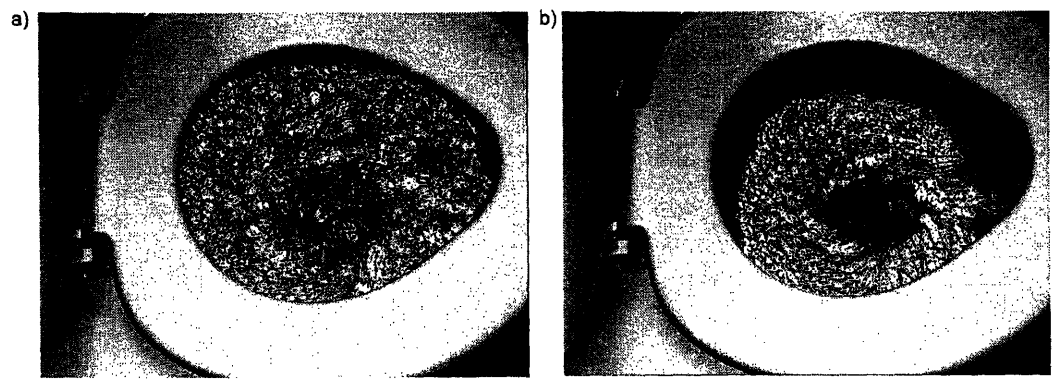

Figure 4-3: Surface instabilities nucleate vortices. a) As the fluid is excited, surface instabilities begin to appear. b) At some critical excitation amplitude a vortex state is energetically favored. The field of view is 20" × 15". *Experimental data courtesy of W. Ketterle.*

ω_l/l may be due to the presence of vortices and the stirrer, both of which make an unperturbed surface mode analysis inadequate."

I would like to add an additional note that again seems obvious in retrospect. The most likely explanation for the the structure in the 3- and 4-point data is that the system was overdriven. (The 2-point data was taken at much lower stirring power and hence does not exhibit this same behavior.) The coupling was so strong on resonance that vortices were ejected from the system. Thus, the number of vortices dips sharply on resonance. We see similar behavior when we stir the condensate near the trap frequency. This simple explanation did not occur to any of us at the time. It actually came about three years later when I showed the data to Martin Zwierlein, who upon glancing at the curves said something to the effect of "Aaahhh, this is where you super power-broadened the resonances." to which I responded with an "Oohh —-(expletive)!"

4.2 Vortex Structure

At low rotational velocities, vortices should not be rectilinear as assumed in many theoretical calculations but bent [36, 5]. Such bent vortices should have lower visibility

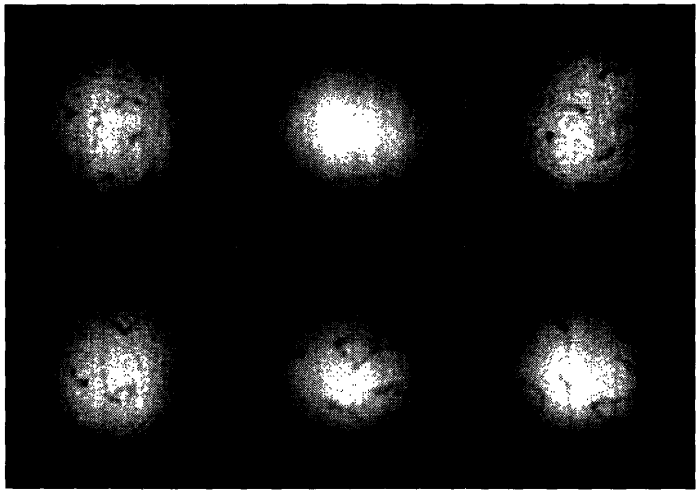

Figure 4-4: Three-dimensional structure of vortices. Shown are several examples of time-of-flight pictures of condensates at low rotational frequencies, where "smeared-out" vortex cores and elongated features were observed. The condensate radius was 510 μm.

due to the line of sight integration across the optically pumped condensate slice. Figure 4-4 shows several examples. Some appear as vortex lattices with tilted vortex cores. Other images show structures reminiscent of half rings and coiled vortices. However, it is not obvious how some of the observed time-of-flight features are related to spatial structures in the trapped condensate.

4.3 Effects of Rotation

In our earlier work we observed that the size of a condensate with vortices exceeded the size of the non-rotating condensate [2]. Figure 4-5 shows an enhancement of the cloud size R in time-of-flight by up to 25% due to additional rotational kinetic energy. Rotation adds a centrifugal potential $-\frac{1}{2}M\Omega^2 r^2$, leading to an effective radial trapping frequency of $\sqrt{\omega_r^2 - \Omega^2}$.[2] Let us keep this effect in mind as we move to the next chapter.

[2]This, of course, sets the trap frequency ω_r as the limit to how fast we can rotate the condensate before losing confinement.

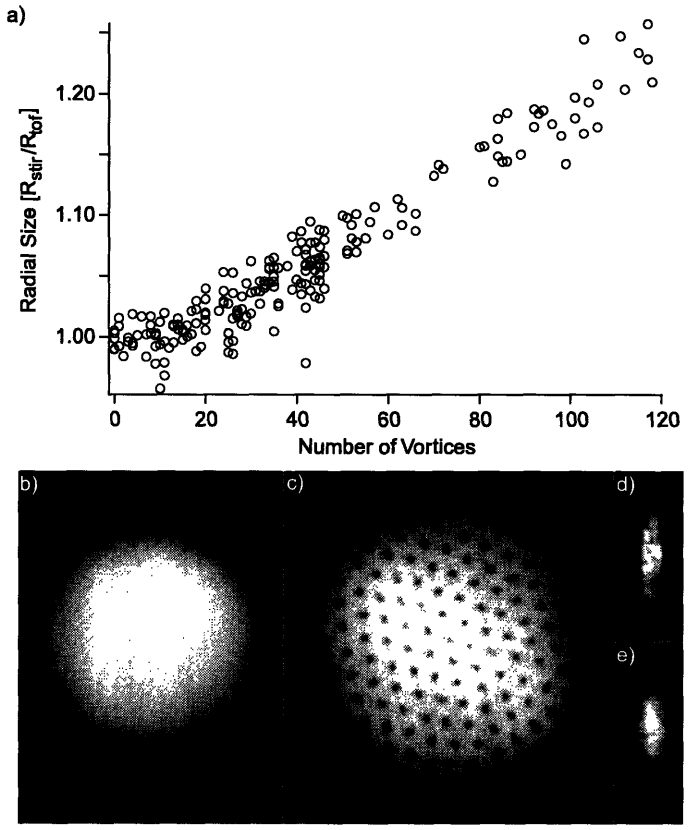

Figure 4-5: Centrifugal effects on a rotating condensate. a) Observed radial size of the condensate, as determined from a parabolic fit to the time-of-flight distribution after 41.5 ms. (b,c) Comparison of a non-rotating condensate ($R_{\rm tof}$ = 570 μm) and one with 160 vortices. Radial in-situ phase contrast imaging of d) a condensate at rest, and e) in rotation at a frequency of 75 Hz, showing the modified aspect ratio. The length of the condensate in d) was 200 μm.

Chapter 5

Formation and Decay of Vortex Lattices

The striking regularity of vortex lattices may be viewed as a rather auspicious feature of nature. While Abrikosov and Tkachenko showed that these triangular lattices are energetically favored, it was unclear whether the dynamics of the system would allow a disordered state to "crystallize". Here we investigate the time scales and mechanisms for this crystallization. In contrast to the decay of the vortex lattice, temperature appears not to play a critical role in its formation.

This chapter supplements work reported in the following publication:

J.R. Abo-Shaeer, C. Raman, and W. Ketterle

"Formation and Decay of Vortex Lattices in Bose-Einstein Condensates at Finite Temperatures,"

Phys. Rev. Lett. 91 070409 (2002).

(Included in Appendix C) Ref [1]

5.1 Introduction

Here we report the first quantitative investigation of vortex dynamics at finite temperature. The crystallization and decay of a vortex lattice have been studied and

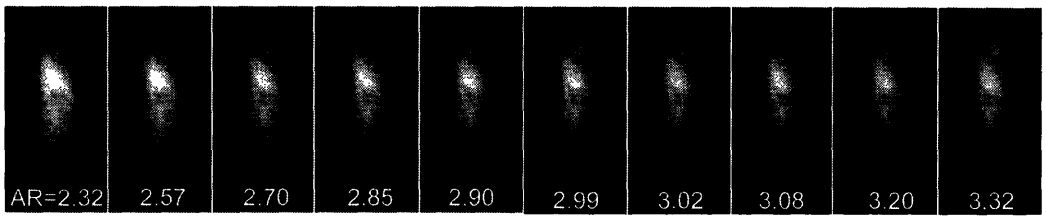

Figure 5-1: a) Spin down of a rotating condensate in a static magnetic trap. The first phase contrast image is taken 200 ms after turning off the drive, with each subsequent image spaced by 200 ms. The rotating vortex lattice caused a radial swelling of the condensate, reducing the aspect ratio. As vortices leave the system the aspect ratio approaches its static value of 4.2. The field of view is 25 μm by 75 μm.

a striking difference is found between the two processes: while the crystallization is essentially temperature independent, the decay rate increases dramatically with temperature.

As mentioned in Chapter 4, the condensate's rotation rate can be inferred from its centrifugal "bulge". Because of this, the decay rate can be determined by taking a series of *in situ* images of a single condensate.

In studying the formation process an interesting experimental challenge arises: How exactly can we quantify formation? A clever method devised by my colleague T. Rosenband will be introduced, and then revisited in more depth later. Results from the formation analysis will allow us to draw some surprising conclusions about the mechanism driving formation.[1]

5.2 Decay of Vortex Lattices

The decay of the vortex lattice can be observed by monitoring the centrifugal distortion of the cloud due to the presence of vorticity. This is a quantitative measure for the rotation frequency, Ω, of the lattice, and therefore the number of vortices [77]. Such distorted shapes have been observed previously for rotating clouds[2, 41, 83].

The shape of a rotating condensate is determined by the magnetic trapping po-

[1] As is often the case in physics, what seems surprising to some is obvious to others. However, to the best of my knowledge, this formation mechanism is still an open-ended question.

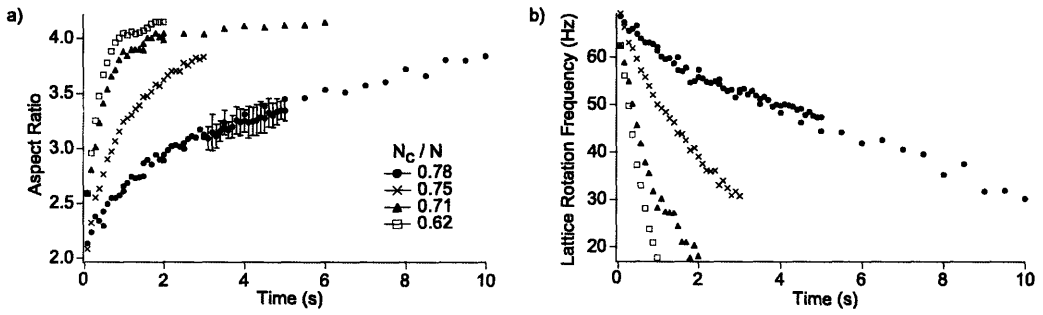

Figure 5-2: Decay of a vortex lattice at finite temperatures. a) The aspect ratio of the condensate approaching its static value. b) The decay of the rotation rate of the lattice for the same data using Eq. (5.1). The decay of the rotation depends strongly on the thermal component.

tential and the centrifugal potential $-\frac{1}{2}M\Omega^2 r^2$, where M is the atomic mass. From the effective radial trapping frequency $\omega_r \rightarrow \omega_r' = \sqrt{\omega_r^2 - \Omega^2}$, one obtains the aspect ratio of the rotating cloud, $A' = \omega_r'/\omega_z$, as

$$A' = A\sqrt{1 - (\Omega/\omega_r)^2}. \tag{5.1}$$

The damping rate of the vortex lattice, obtained from exponential fits to the data, was studied at different temperatures by varying the condensed fraction of atoms in the trap.

Figure 5-2a shows how the aspect ratio of the condensate approaches its static value as the vortex lattice decays. The decrease of the angular speed appears to be exponential (Figure 5-2b) and strongly depends on temperature (Figure 5-3). It should be noted that the exponential nature of the decay is related to the co-rotation of the thermal cloud with the condensate. When the thermal cloud is fixed, theoretical [112] and experimental [67] studies show nonexponetial behavior.

5.3 Formation of Vortex Lattices

In addition to the decay process, the formation of the vortex lattice has also been examined. After rotating the condensate it typically took hundreds of ms for the

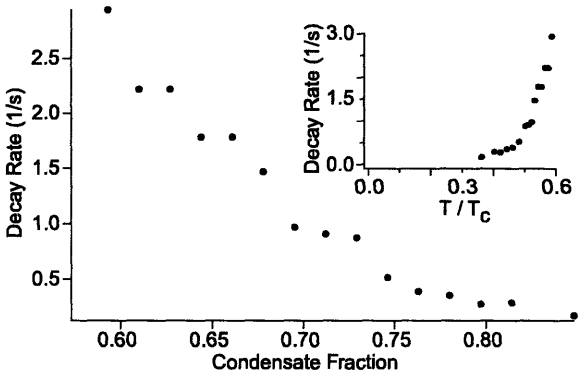

Figure 5-3: Decay rates for vortex lattices at several temperatures. The rates are determined from data taken during the 1st second of equilibration.

lattice to form (see Figure 4 in ref. [2]). One may expect the lattice to form in the rotating frame during the stirring because the lattice is the lowest energy state for a given angular momentum. The absence of equilibration in the rotating frame is presumably due to heating and excitation of collective lattice modes by the stirring beams. The crystallization of the vortex lattice was studied by determining the contrast or visibility of the vortex cores as a function of equilibration time. To avoid any bias, we used an automated vortex recognition algorithm. First, each image was normalized by dividing it by a blurred duplicate of itself. A binary image was then created, with a threshold set to the value at which the algorithm reliably detected almost all vortices that were identified by visual inspection of equilibrated images (there was less than 5% discrepancy). Clusters of contiguous bright pixels within a circular area were counted as "visible" vortices. Figure 5-4a shows three vortex lattices after different equilibration times with the visible vortices identified.

Figure 5-4b,c show that the formation of the lattice depends very weakly, if at all, on temperature over the range studied. The larger number of vortices crystallized at lower temperatures (Figure 5-4b) is due to the strong temperature dependence of the lattice decay rates, which differed by more than a factor of 5. We can correct for this by estimating the number of vortices $N_v(t)$ as a function of time from the centrifugal distortion measurements described above as $N_v(t) = 2\Omega(t)/\kappa \cdot \pi R(t)^2$, where $\kappa = h/M$

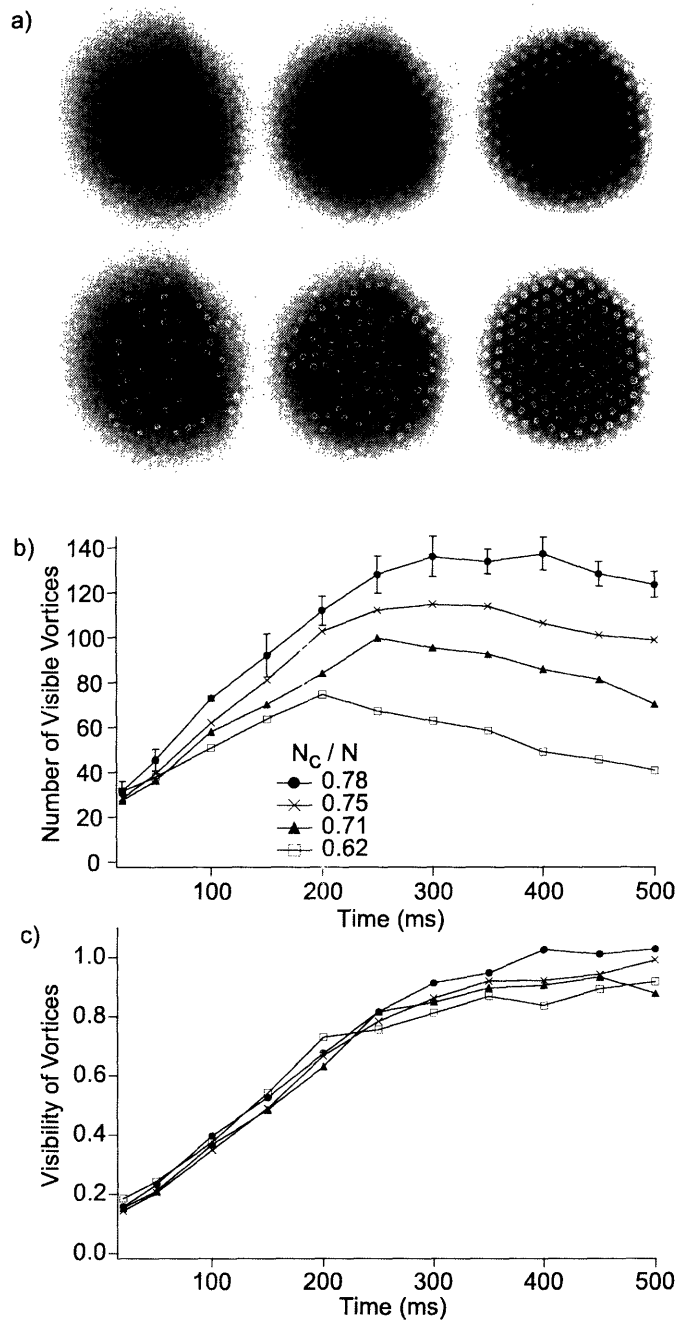

Figure 5-4: Crystallization of the vortex lattice. a) The top row shows three condensates that have equilibrated for 50, 150 and 300 ms, respectively, and have 48, 86 and 140 vortices recognized as "visible" by our algorithm. The bottom row shows the same condensates with the "visible" vortices circled. The field of view was 1.4 mm by 1.6 mm. b) Growth of the number of visible vortices for several temperatures expressed by the condensate fraction (N_c/N). c) Visibility of vortices derived from the data in figure b, normalized by the number of vortices inferred from centrifugal distortion measurements.

is the quantum of circulation, M the sodium mass and R the radial Thomas-Fermi radius. By normalizing the number of visible vortices by this estimate, we deduce the vortex visibility as a function of time. These lattice formation curves overlap almost perfectly for different temperatures (Figure 5-4c).

5.3.1 Damping Mechanism

In contrast to the decay, the crystallization process of the vortex lattice was essentially independent of temperature. This was unexpected because all dissipative processes observed thus far in BECs, including the decay of the vortex lattice, have shown a strong temperature dependence [53, 92]. D. Feder has numerically simulated a stirred condensate using only the Gross-Pitaevskii equation. The results show that the absence of dissipation leads to rapid, irregular motion of the vortices. The addition of a phenomenological dissipative term in ref. [99] resulted in the formation of triangular vortex lattices. However, the origin of the dissipation was not identified. Our results suggest that the time-limiting step for the evolution of a vortex tangle into a regular lattice does not depend strongly on temperature. One possibility is that the thermal cloud is not directly involved. This may be similar to the reconnection of vortices or the damping of Kelvin modes, where the spontaneous creation of excitations act as a dissipative mechanism [63]. Another possibility is that the rearrangement of the vortices into a rectilinear lattice is slow and not limited by dissipation. Our quantitative analysis of the formation process seems to contradict qualitative observations made in Paris [67], in which the lattice ordering appeared to have temperature dependence. This indicates that further study may be necessary to fully characterize the role of the thermal cloud in the formation process.

5.4 "Visible" Vortices Revisited

The algorithm for defining a "visible" vortex was touched upon earlier. I revisit it here because it was not only crucial to the experiment, but because it made such a qualitative difference in our lives. Vortex lattices were both a blessing and a curse

for Chandra Raman and me. This algorithm grew out of our desire to automate the vortex counting. For the previous paper on vortex nucleation [83], the two of us spent endless hours methodically counting the vortices as they appeared on our monitor. For that paper alone we counted over 50,000 vortices by hand. By my estimate, Chandra and I counted over 1 million total! Throughout this time Till Rosenband, UROP extraordinaire, kept telling me he could write a program to do the counting for us. Finally one night I demanded that he deliver. By the time I came to work the next morning Till had a working program.

5.4.1 Vortex Counting Algorithm

How can we quantify the formation process? The answer is relatively simple: count the number of vortices that become "visible" over time. The obvious question then becomes: What defines a "visible" vortex? This answer is again simple. It does not matter how you define a visible vortex as long as the following criteria are met:

- There should be some time dependence on the number of "visible" vortices. We know that as the lattice crystallizes, the visibility increases. Thus, our program should detect this qualitative behavior
- Under identical conditions, the visibilty should be consistent from shot-to-shot.
- The number of vortices that the program counts after crystallization should be consistent with hand counts.

Any algorithm that meets these three criteria works. Figure 5-5 details our approach.

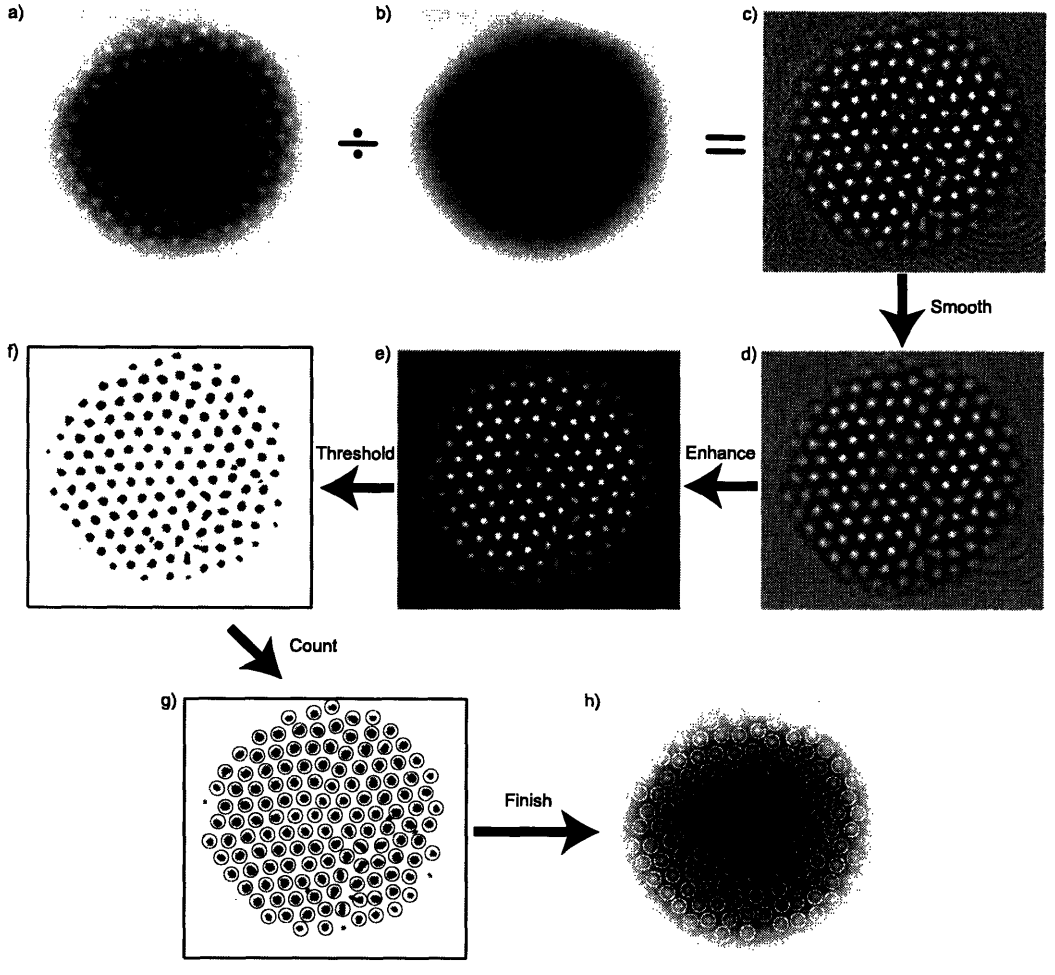

Figure 5-5: Vortex counting algorithm. The raw image in (a) is divided by the image in (b), a blurred duplicate of itself, resulting in the image in (c). This removes the density profile of the condensate and normalizes the brightness of each vortex. This image is then smoothed to remove noise, resulting in image (d). Bright features (vortices) are enhanced by taking the exponential of image (d). A binary threshold is then applied to image (e) such that all pixels below a certain value are set to zero (white), while those above are set to 1 (black). (f) Clusters of contiguous bright pixels above a certain area are counted as "visible" vortices. (g) The location of each "visible" vortex is marked on the original image. In this example the computer counted 133 vortices, while a hand count yielded 134.

Chapter 6

Formation of Ultracold Sodium Molecules

Extending the ultralow temperature regime from atoms to molecules has been a primary goal for atomic physicists. Ultracold molecules offer promise for tests of fundamental symmetry and coherent quantum chemistry. Here I discuss experiments in which quantum-degenerate molecules are created from cold atomic samples.

This chapter describes work reported in the following publications:

K.Xu, T. Mukaiyama, J.R. Abo-Shaeer, J.K. Chin, D.M. Miller, and W. Ketterle *"Formation of Quantum-Degenerate Sodium Molecules,"* Phys. Rev. Lett. 91 210402 (2003).

T. Mukaiyama, J.R. Abo-Shaeer, K. Xu, J.K. Chin, and W. Ketterle *"Dissociation and Decay of Ultracold Sodium Molecules,"* Phys. Rev. Lett. 92 180402 (2004).

(Included in Appendix D) Ref [76]

6.1 Why Cold Molecules?

The motivation for producing ultracold molecules is many-fold. Atomic Bose-Einstein condensates are an ideal system for studies of macroscopic quantum phenomena, including tests of coherence, superfluidity, and collective excitations. The production of *molecular* condensates could facilitate an entirely new class of experiments. Promising areas include quantum gases with anisotropic dipolar interactions, tests of fundamental symmetries, and "Superchemistry", where chemical reactions are stimulated via macroscopic occupation of a quantum state [44].

Despite substantial effort, the creation of molecular condensates has proven difficult. Unfortunately, some techniques that are successful for atom cooling are not easily applied to molecules. Laser cooling is one example of this. Because molecules lack closed (cycling) transitions, it is difficult to coax them into repeatedly scattering resonant light [8]. Until recently, efforts to cool molecules focused mainly on buffer gas loading [104] and Stark deceleration [9]. However, these techniques are still several orders of magnitude from a phase-space density of unity.

Recently, the difficulty in cooling molecules directly has been circumvented by preparing molecules from quantum-degenerate *atomic* samples. This, of course, requires that the molecules are formed without release of energy. Two methods have proven successful for doing this: photoassociation [106, 87] and magneto-association [28, 45, 107, 85, 55, 113, 18, 96] (Figure 6-1). Photoassociation is a process whereby two colliding atoms collectively absorb a pair of photons, forming a bound molecule.[1] Magneto-association occurs when the energy of two colliding atoms is magnetically shifted into resonance with a molecular state. While the translational temperature of these molecules is commensurate with their source atoms, both methods create molecules in highly-vibrational states. In the case of photoassociation, poor wavefunction overlap limits coupling to the last few levels of the ground state potential (The Franck-Condon principle). For magneto-association, the vibrational levels are limited to those that are (magnetically) accessible. The closest states to threshold

[1]This is a specific case of photoassociation. Single photon transitions are also possible, however molecules can only be formed in an excited molecular state (due to selection rules).

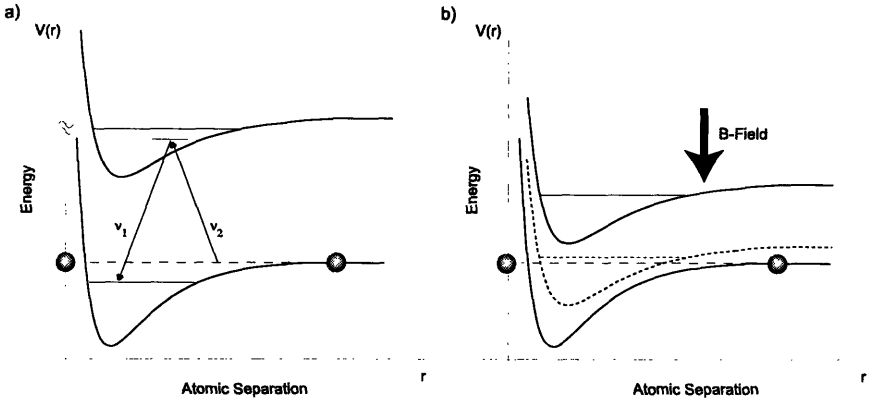

Figure 6-1: Methods for producing ultracold molecules. a) Photoassociation: By choosing ν_1, ν_2 properly, one can induce Raman transitions between free-atom and bound molecular states. b) Magnetoassociation: An applied magnetic field shifts a closely-lying molecular state into resonance with a free-atom state. As the molecular state passes below the free-atom state, atoms are converted to molecules. As discussed in the text, both processes create molecules in *translationally* cold, but high vibrational states.

are typically the highest vibrational states of an excited molecule (on the order of the hyperfine splitting). Because the vibrational ground state of the excited molecule is $\sim$ 50 GHz below these states, a field of $\sim$ 5 T is required bring it into resonance.

It is important to note that these ultracold samples are *not* molecular condensates (at least not directly after creation). For Fermionic molecules[2] the reason is simple, they were not a condensate to begin with. Indeed, these molecules simply inherit the momentum distribution of their source (a degenerate Fermi gas). For Bosonic molecules the reasons are more subtle and may even depend on how one defines a BEC.

I begin this chapter with a discussion of basic principles underlying Feshbach resonances. Feshbach resonances are currently the most popular method for generating ultracold molecules. Next, I describe the experimental realization of quantum degenerate sodium molecules. Some important (and unfortunate) properties are covered, such as initial phase-space density and lifetime. Finally, I conclude with a discus-

[2]To clarify, I use the terms "Fermionic molecules" to describe molecules composed of Fermionic atoms and "Bosonic molecules" to describe molecules composed of Bosonic atoms. Of course, both classes of molecules are Bosonic. The terminology is a bit sloppy, but it greatly simplifies the text.

sion of the characteristics that define a Bose-Einstein Condensate, and why Bosonic molecules have (thus far) failed to meet these criteria.

6.2 Feshbach Resonances

The analysis of atom-atom interactions is fairly simple in the ultracold regime ($\sim$ 1 μK). At these temperatures the de Broglie wavelengths ($\sim 10^4 a_0$) of colliding atoms extend much further than their atomic diameters ($\sim 10^2 a_0$). Because waves impinging on small objects (compared to their wavelength) produce primarily isotropic scattering, it is appropriate to limit our treatment of ultracold interactions to the s-wave regime. In this case the two-body Hamiltonian $V(\vec{r}_1, \vec{r}_2)$ can be approximated by the local Hamiltonian [81]

$$V(\vec{r}_1, \vec{r}_2) = \frac{4\pi\hbar^2 a}{m}\delta(\vec{r}_1 - \vec{r}_2) \tag{6.1}$$

where m is the atomic mass and a is the s-wave scattering length. The precise value of a depends on details of the interatomic potential, and very small variations can produce dramatic variation. Recall from Chapter 1 that the magnitude and sign of a dictate the macroscopic properties of the condensate, including the density profile and stability. When the scattering length is positive, atoms bounce off one another like hard spheres of radius a. When the scattering length is negative, atoms tend to attract, and the condensate is stable only for small numbers of atoms [86].

The fact that the interaction strength depends critically on this single parameter a has very important consequences. As we shall see, both the *magnitude* and *sign* of a can be externally controlled, providing experimentalists with unprecedented control over the properties of the system. The feature that allows us to "tune" a is known as a Feshbach Resonance [32]. In the vicinity of these resonances a diverges to $\pm\infty$ (Fig. 6-2). Feshbach resonances occur when the total energy of two colliding atoms equals the energy of a molecular state. Therefore, if the magnetic moment of the molecular state differs from the atomic state, one can use a magnetic field to Zeeman shift the two states into resonance. The use of Feshbach resonances to tune atomic interactions was first suggested in 1992 by B. Verhaar and colleagues [97].

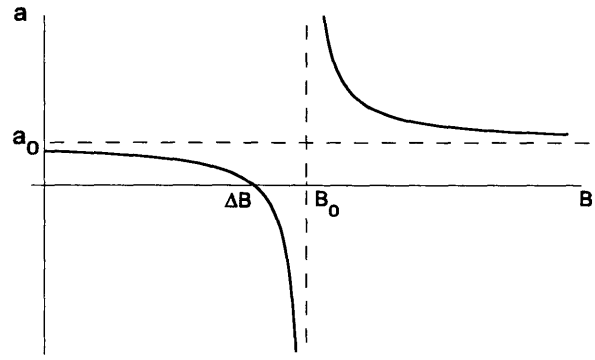

Figure 6-2: Resonant enhancement of the scattering length in the vicinity of a Feshbach resonance. Resonances of this type occur when a new bound state is introduced to the system. The lineshape has functional form $a = a_0[1 - \Delta B/(B - B_0)]$, where a_0 is the background scattering length, ΔB is the width of the resonance, and B_0 is the resonance center.

6.2.1 Model of Feshbach Resonance

To understand why scattering is enhanced in the vicinity of a Feshbach resonance we turn our attention to a simple model for colliding atoms at threshold (Figure 6-3) [20]. The van der Waal potential, typical of interatomic interactions, is replaced by a spherical box of depth V_0 and extent b. Since we are considering only s-waves we look for solutions to the Schrodinger equation with $\ell = 0$.

$$\psi''(r) - \frac{2\mu V(r)}{\hbar^2}\psi(r) = 0 \tag{6.2}$$

where μ is the reduced mass of the system. Defining $k = \sqrt{2\mu V_0}/\hbar$, the solutions to Eq(6.2) are

$$\psi(r) = \begin{cases} A(r-a) & r \geq b \\ Bsin(kr) & r < b \end{cases} \tag{6.3}$$

Therefore, the scattering length has form

$$a = b - \frac{tan(kb)}{k} \tag{6.4}$$

A plot of this function is given in Figure 6-3c. From this we note the following:

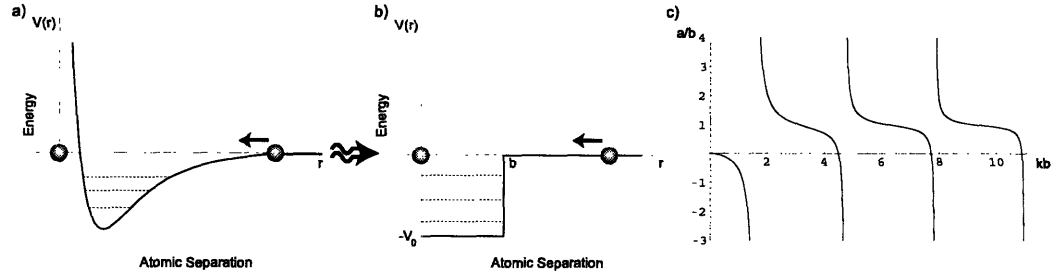

Figure 6-3: Toy potential to illustrate resonant scattering. a) The van der Waal potential is typical of interatomic interactions. This potential is modelled by b) an exactly-solvable toy potential. c) As the potential depth V_0 is increased, the scattering length diverges each time a new bound state is introduced to the system.

1) As the depth of the well V_0 is increased, the scattering length diverges whenever $kb = (2n + 1)\pi/2$. This is equivalent to the condition that the spherical well possesses a zero-energy bound state. Thus, we see that *resonances occur upon the appearance of a new bound state.*

2) Away from the resonances the scattering length approaches the background value b, the same behavior we observed in Figure 6-2.

3) Slightly below the threshold for the appearance of a bound state, a becomes large and negative. Above threshold a switches sign. Therefore, in order to make molecules we should sweep the atoms from the negative side of the resonance to the positive side.

To be clear, the model used here is that of a single-channel resonance. Feshbach resonances are inherently two-channel features. However, the characteristic behavior is identical.

6.2.2 Experimental Notes

The first observations of Feshbach resonances were not made by observing molecule creation directly, rather by measuring enhanced losses and a dispersive variation of the scattering length in the vicinity of the resonance[50, 93]. Typically, the main loss

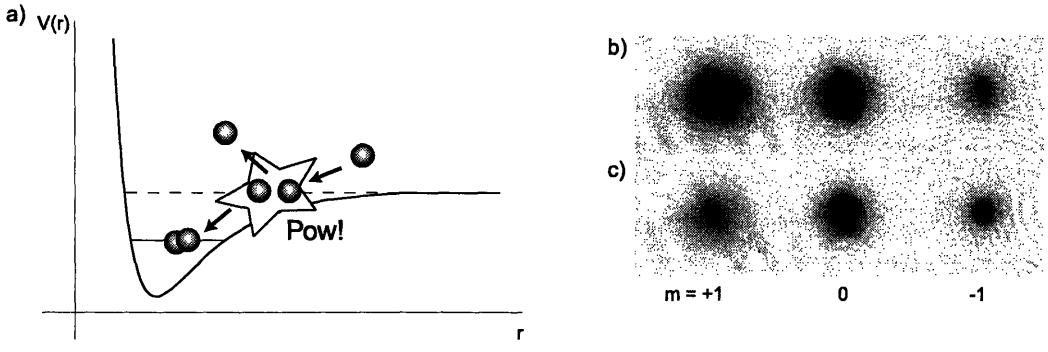

Figure 6-4: Loss mechanism in the vicinity of a Feshbach resonance. a) In three-body recombination two atoms form a deeply bound molecule, with the third carrying away the excess energy. When the scattering length is increased, the probability that three atoms will come in contact also increases. b) The three hyperfine states just below the 907 G resonance of $|1,1>$ state. c) Passing through the resonance, atoms in the m $= +1$ are preferentially lost.

mechanism for a condensate is three-body recombination (Figure 6-4). In this process three atoms come together to form binary molecule, with one atom carrying away the binding energy. Because this process requires three atoms to come in contact, its occurrence is rare.[3] However, at the Feshbach resonance $|a|$ is greatly enhanced, and thus, so to is the likelihood of contact. Therefore, the primary signature of Feshbach resonances in bosonic systems is strong inelastic decay.

6.3 Production of Molecules

To generate the molecules, sodium condensates in the $|F = 1, m_F = -1\rangle$ state were prepared in an optical dipole trap. The radial and axial trap frequencies of $\omega_r = 2\pi \times 290$ Hz and $\omega_z = 2\pi \times 2.2$ Hz, respectively, gave Thomas-Fermi radii of $R_r = 5$ μm and $R_z = 650$ μm, and a peak density of 1.7×10^{14} cm^{-3} for 5 million atoms. An adiabatic radio frequency sweep was used to transfer the atoms into the $|1,1\rangle$ state, which has a 1 G wide Feshbach resonance at 907 G [50, 100].

After 1 second equilibration in the optical trap, the molecules were generated

[3] At least this is the case for typical peak densities of $\sim 2\ 10^{20}$ m^{-3}.

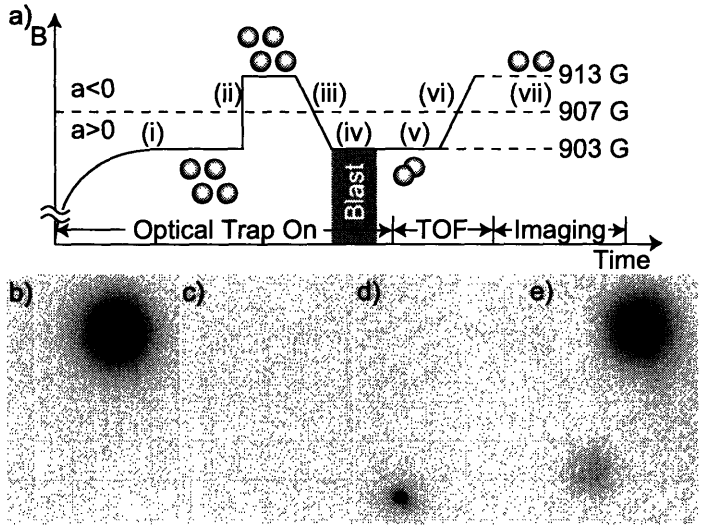

Figure 6-5: (a) Experimental method for producing and detecting ultracold molecules. (i) Bose condensed atoms in an optical dipole trap are exposed to a magnetic field just below a Feshbach resonance. (ii) The field is quickly stepped through the resonance to minimize atom loss. (iii) The field is then swept back through the resonance, creating an atom-molecule mixture. (iv) Unpaired atoms are removed from the trap with resonant light, yielding a pure molecular sample. (v) The trap is switched off, allowing the molecules to expand ballistically. (vi) Finally, the magnetic field is swept back across the resonance to reconvert the molecules to atoms for imaging (vii). (b) Image of the *atomic* sample after ramping the field to produce molecules; (c) after the resonant light pulse has removed all unpaired atoms; (d) after the *molecules* ($\sim 10^5$) have been reconverted to atoms. (b-c) were taken along the weak axis of the trap after 17 ms ballistic (time-of-flight – TOF) expansion. (e) An image showing both atomic (top) and molecular (bottom) clouds after 14 ms ballistic expansion, spatially separated by a magnetic field gradient. With 4 ms field ramp-down time, some molecules survived even without the blast pulse, but are much more heated. The field of view of each image is 1.8 mm $\times$ 1.3 mm.

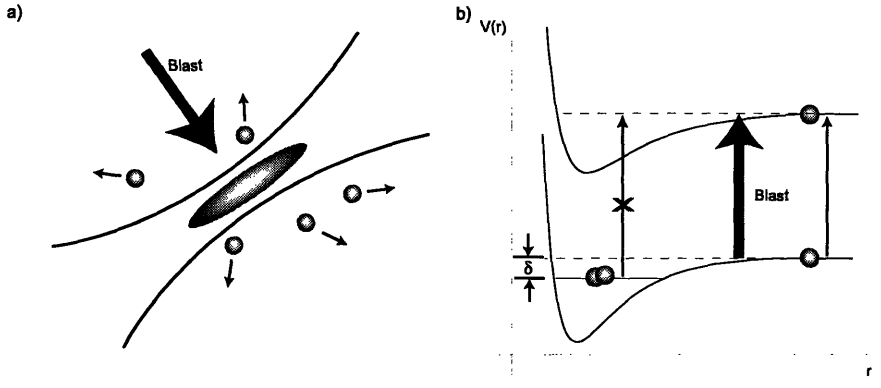

Figure 6-6: "Blast" pulse for removing unpaired atoms. a) To remove unpaired atoms from the trap, the sample was irradiated with a 10 μs pulse of resonant light. b) Because the blast was done at a field far from the Feshbach resonance, the mixing between atomic and molecular states was small, and therefore molecules were transparent to pulse.

using the field ramping scheme illustrated in Figure 6-5a. An applied magnetic field was ramped in ~100 ms to 4 G below the 907 G Feshbach resonance. The field was generated using a pair of large bias and small anti-bias coils. Because molecules are only created when sweeping across the resonance from negative to positive scattering length, the field was stepped up to 913 G as quickly as possible (~1 μs) to jump over the resonance with minimal atom loss. After allowing 2.5 ms for transient field fluctuation to damp out, the field was ramped down in time τ_{Down}. Due to atom-molecule coupling, part of the atomic population was transferred into the molecular state following the Landau-Zener avoided crossing. With the given width of the resonance and the atomic density, we use a simple Landau-Zener model to calculate a ramp speed of $\sim 10^4$ G/s to transfer roughly half the atoms to the molecular state [72, 101, 110]. However, inelastic collisions led to fast decay for both the atoms and the molecules near the resonance. We found that a faster ramp speed of $\sim 10^5$ G/s (corresponding to $\tau_{Down} = 50$ μs) gave optimal results. The conversion efficiency of atoms to molecules was ~4%. Slower ramp speeds resulted in a similar number of molecules, but at higher temperature (see Figure 6-5e).

The blast pulse was applied along the radial axis of the trap to minimize collisions

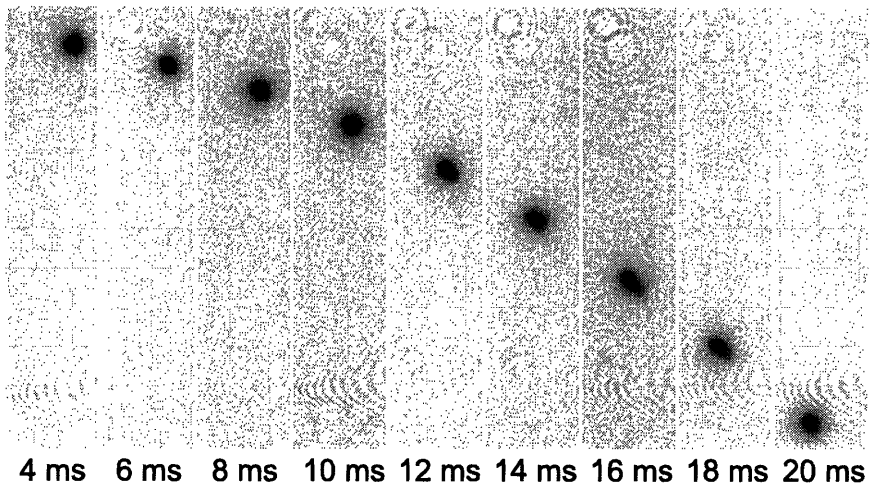

Figure 6-7: Ballistic expansion of a pure molecular sample. Absorption images of molecular clouds (after reconversion to atoms) are shown for increasing expansion time after switching off the optical trap. The small expansion velocity corresponds to a temperature of ~30 nK, characteristic of high phase-space density. The images are taken along the weak axis of the trap. The field of view of each image is 3.0 mm × 0.7 mm.

between the escaping atoms and the molecules at rest (see Figure 6-6a). A 20 μs pulse of resonant light removed all atoms from the optical trap, leaving behind a pure molecular sample (see Fig. 6-5). At only 4 G below the Feshbach resonance, the light was still close to resonance with molecular photodissociation to low-velocity atoms, but the overlap matrix element was sufficiently diminished to leave the molecules unaffected (see Figure 6-6b). After a variable hold time, the optical trap was switched off and the molecules expanded ballistically for between 4 to 20 ms. The molecules were detected by converting them back to atoms with field ramp-up in $\tau_{Up} = 100$ μs at the end of expansion. Varying τ_{Up} between 50 μs and 4 ms did not affect the recovered atom number, though shorter τ_{Up}'s recovered atoms with larger kinetic energy [76]. Thus we assume all molecules are converted back to atoms. A resonant absorption image was taken after an additional 500 μs, which allowed the imaging field to settle. The rapid conversion of molecules to atoms after a long expansion time ensured that the absorption images accurately depicted the momentum distribution of the *molecular* cloud.

Atoms and molecules were separated during the ballistic expansion by a Stern-Gerlach technique (Figure 6-5e). Due to trap imperfections, the large bias coils provided an additional radial gradient of the axial field of ~2.8 G/cm in the vicinity of the condensate. This value was determined from the trajectory of the falling atoms. Since the molecules have a different magnetic moment, they separate from the atoms during the ballistic expansion (Figure 6-5e). From the separation of the atomic and molecular clouds at different times, we determined the difference between atomic and molecular magnetic moments to be $3.2\mu_B$ (μ_B is the Bohr magneton), in good agreement with theory [110].

6.4 Molecular Properties

6.4.1 Phase-Space Density

For different ramp down times τ_{Down}, the time-of-flight images of the molecular cloud exhibit drastically different momentum distribution. The coldest cloud was obtained with the fastest ramp down time possible, $\tau_{Down} = 50$ μs (Fig. 6.3). A gaussian fit was used to determine the molecular temperature T_m and the phase-space density. Due to the rapid ramp down, the molecules had no time to adjust to the external trapping potential or any mean-field interactions. Therefore, we assume the molecules were *uniformly* created with the Thomas-Fermi profile of the original atomic BEC. The peak phase-space density is then given by

$$PSD_{peak} = \left(\frac{h}{\sqrt{2\pi k_B T_m M_m}}\right)^3 \frac{N_m}{\frac{8\pi}{15} R_r^2 R_z} \tag{6.5}$$

where h is the Planck constant, k_B is the Boltzmann constant, M_m is the molecular mass, N_m is the number of molecules. The second factor in the equation is the peak density for a Thomas-Fermi profile.

Phase-space densities in excess of 20 were observed, much larger than the critical value of 2.6. This demonstrates that a quantum-degenerate cloud of atoms can be transformed into a quantum-degenerate molecular gas.

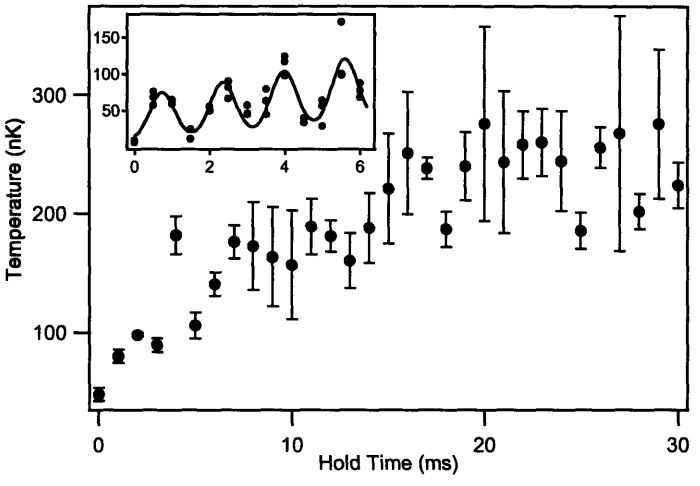

Figure 6-8: Temperature of the molecular cloud. After 15 ms, the temperature saturates at $\sim$ 250 nK. Error bars represent the statistical error (standard deviation). The inset shows finer resolution data for holding times up to 6 ms. The solid line is a guide to the eye.

6.4.2 Molecular Lifetimes

Further experiments with ultracold sodium molecules will critically depend on their collision properties. Therefore we studied heating and inelastic collision processes. As shown in Figure 6-8, we observed monotonic heating of the pure molecular sample over $\sim$ 30 ms. In addition, we observed short timescale oscillations (6 ms) in the fitted temperature (inset of Figure 6-8). Such breathing oscillations were excited because the molecules were formed over the volume of the atomic condensate and started oscillation around their equilibrium volume (see Figure 6-9). The equilibrium volume deduced from the observed released energy is much smaller than the initial volume. The absence of damping implies a collision time of at least 6 ms, or a molecular scattering length smaller than 17 nm (obtained using the expression for the collision rate $8\pi a^2 v_{th} n_m$ where v_{th} is the thermal velocity). It is unclear whether the oscillation disappeared due to collisions or limited signal-to-noise ratio.

The temperature of the molecular cloud saturated at $\sim$ 250 nK after 15 ms. A possible explanation is the balance between heating due to inelastic molecular decay and the evaporative cooling caused by the finite trap depth (1.7 μK). This would imply

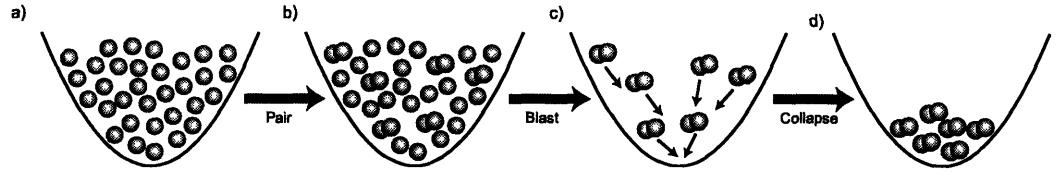

Figure 6-9: Collapse of a molecular cloud. a) The size of the atomic condensate is set by its mean-field energy. b) After passing through the Feshbach resonance a small fraction of the sample is converted to molecules. c) When unpaired atoms are blasted away the molecules no longer have sufficient mean-field energy to sustain their size. d) The molecules collapse and undergo breathing oscillations for a short period of time (see the inset of Figure 6-8) before reaching their new equilibrium size.

a collision time of 15 ms. However, we have no clear evidence that thermalization has occurred. Clearly, further studies of elastic collisions between ultracold molecules are necessary.

Molecules formed via an s-wave Feshbach resonance are created in the rotational ground state, but in high vibrational states. Therefore, one expects vibrational relaxation to be a strong, inelastic decay mechanism (Figure 6-10).

Figure 6-11(a) shows the decay of a pure molecular sample. The decay was analyzed with the rate equation

$$\frac{\dot{N}_m}{N_m} = -K_{mm} n_m. \tag{6.6}$$

Here N_m, n_m is the number and the density of the molecules respectively, and K_{mm} is the molecule-molecule collision rate coefficient. Because of the changing size and temperature of the molecular cloud during the first $\sim$ 15 ms (Fig. 6-8), we only fit data points at later times, assuming a thermal equilibrium volume for the molecules. The decay at earlier times is slower, consistent with a larger molecular cloud. The fit yields a molecule-molecule collision coefficient of $K_{mm} \sim 5.1 \times 10^{-11}$ cm^3/s, about 2 orders of magnitude larger than the typical values reported for fermions [54, 18].

Inelastic collisions between molecules and atoms were also observed by keeping atoms in the trap (Figure 6-11(b)). The decay was analyzed assuming that the loss of molecules occurred mainly due to collisions with atoms, resulting in an exponential

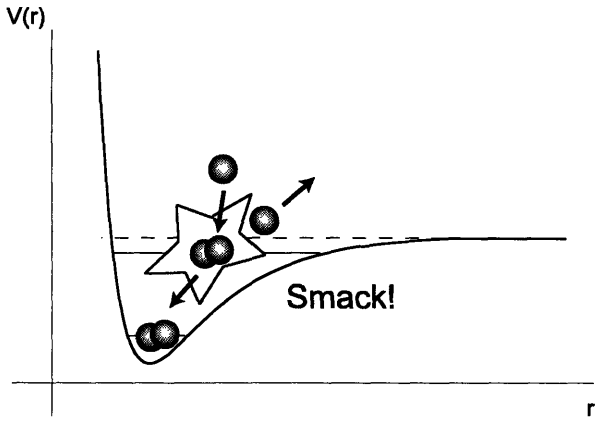

Figure 6-10: Decay mechanism for molecules. In the presence of atoms, molecules quickly decay due to inelastic collisions. A molecule colliding with an atom will decay into a lower vibrational state, with the excess energy converted to kinetic energy. For bosonic molecules, these collisions limit the conversion efficiency and prevent molecular condensation. In Fermi systems these collisions are suppressed by to Pauli blocking.

decay:

$$\frac{\dot{N}_m}{N_m} = -K_{am} n_a. \tag{6.7}$$

Here n_a is the density of atoms, and K_{am} is the atom-molecule collision rate coefficient. From the fit, we extract a lifetime of 106 μs and a rate coefficient $K_{am} \sim 5.5 \times 10^{-11}$ cm^3/s, which agrees well with theoretical predictions [111, 110].

The inelastic losses determine the maximum conversion efficiency from atoms to molecules. For an adiabatic ramp, one expects close to 100% conversion efficiency. Indeed, in experiments with fermionic atoms, efficiencies up to 85% have been observed [18]. Figure 6-12 shows the results for magnetic field ramps of different durations. The two sets of images show that applying the blast pulse dramatically improved the molecular number and temperature. Without it, a slower ramp time (4 ms) appeared to be more favorable for molecule formation (open circles in Fig. 6-12(c)). No molecules were observed for a 50 μs ramp time. However, with the blast pulse, a similar number of molecules was obtained for all ramp times between 50 μs to 4 ms (closed circles in Fig. 6-12(c)).

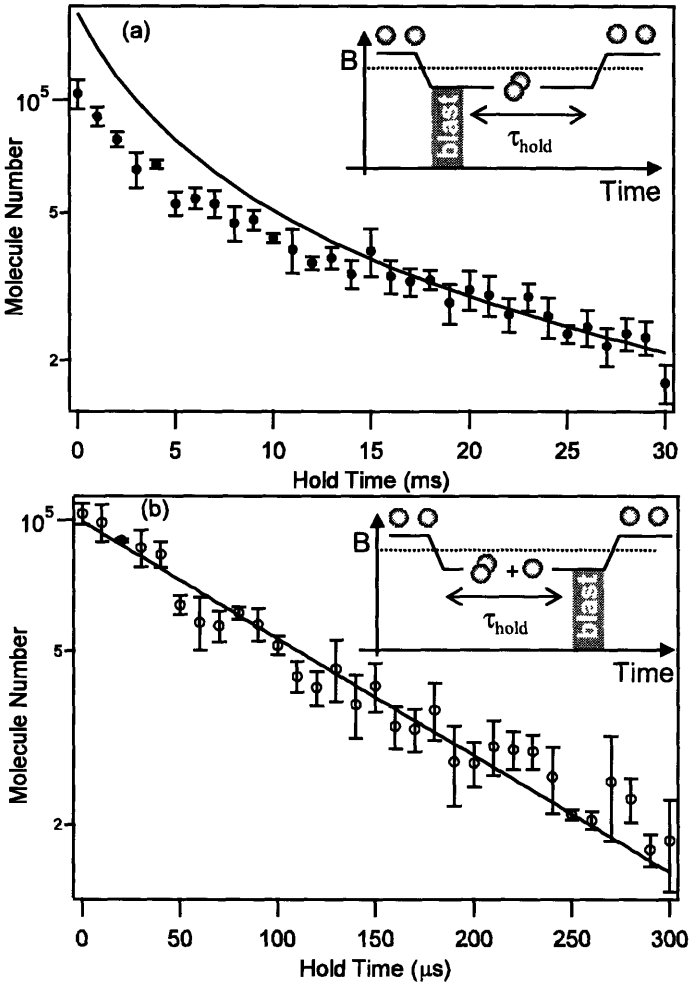

Figure 6-11: Decay of ultracold molecules trapped alone (a) or together with atoms (b). The solid lines in (a) and (b) are fits of eq.(6.6) and (6.7) to data, which assume vibrational relaxation in the collision of molecules (a) or collisions between molecules and atoms (b). The insets illustrate the experimental sequences.

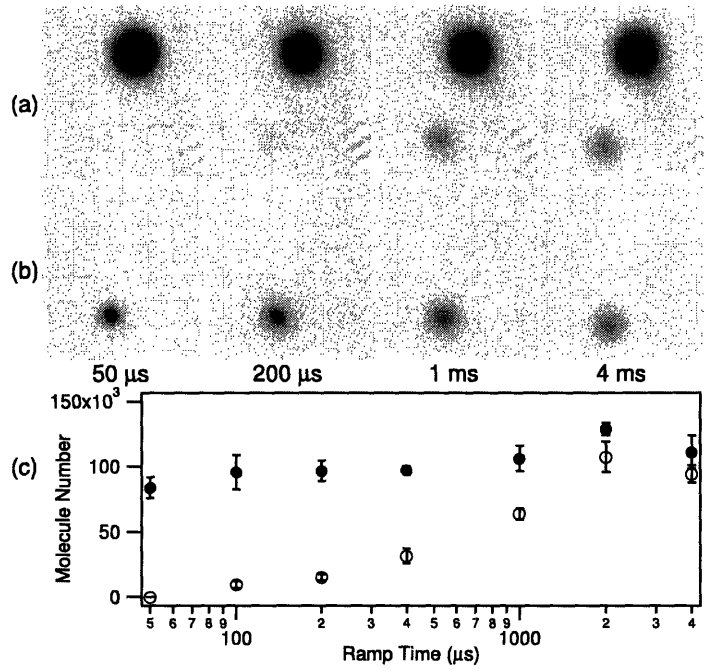

Figure 6-12: Conversion of atoms to molecules for various ramp times. During a given time, the magnetic field was swept by 10 G. Figures (a) and (b) show absorption images taken after 14 ms TOF. The molecules (bottom) were radially separated from the atoms (top) by a field gradient of 2.8 G/cm. The molecules were converted back to atoms only 0.5 ms before imaging by ramping the magnetic field back across the Feshbach resonance. This time was chosen to be long enough for any transient field fluctuations to damp out, but short enough such that the size of the imaged cloud reflected the molecular temperature, not the dissociation energy. (a) The atoms remained in the trap. (b) The atoms were removed by a resonant laser pulse immediately after the magnetic field ramp. (c) Number of molecules as a function of ramp time for (a) (open circles) and (b) (closed circles).

We assume that these results reflect the interplay of two competing processes. The adiabatic condition requires a relatively slow field ramp for efficient conversion. However, this means that the atoms and molecules spend more time near or at the Feshbach resonance, where inelastic collision rates are enhanced. In contrast to Fig.6-12(b), the absence of molecular signal in Fig. 6-12(a) for 50 μs ramp time reflects that the atomic density reduction due to the mean-field expansion is too slow for the molecules to survive the inelastic collisions with the atoms.

6.5 What Makes a BEC a BEC?

Now that we have seen how bosonic molecules behave we are ready to make statements about what they are (and what they are not). The translational temperature of the molecules is indeed (instantaneously) commensurate with their source (a BEC), and 30 nK is well below the transition temperature T_c for this number of molecules. Unfortunately, we also see that these molecules undergo fast vibrational relaxation. Whether our molecular sample is a condensate depends on one's definition of BEC. If phase-space density in excess of 2.6 (corresponding to a diagonal matrix element of the single-particle density matrix larger than one) is sufficient, then one may regard a short-lived atom-molecule superposition state [25] as a molecular BEC. However, following this definition, a small excited state admixture in an optically trapped BEC would qualify as BEC of electronically excited atoms. If one asks for the additional requirement of a pure molecular sample, we have achieved that in this work. Another definition would require phase coherence, which could again be observed even in short-lived samples. Should one also require a lifetime of the degenerate sample exceeding the collision time (to achieve local equilibrium), the trap period (to achieve global equilibrium), or the inverse mean-field energy (the typical dynamic timescale)? In our opinion, BEC requires thermal equilibrium. High phase-space density is necessary, but not sufficient.

6.5.1 A Final Note

As we have seen, vibrational relaxation not only prevents Bosonic molecules from condensing, it also severely limits their conversion efficiency [28, 45, 107]. The creation of molecules in highly vibrational states is not a problem if there is no decay mechanism to lower states. Indeed, this is the case for Fermionic molecules. Although Pauli blocking starts them off at a disadvantage temperature-wise (compared to their Bosonic counterparts), it also prevents three-body losses. Molecular condensation then proceeds via simple evaporative cooling [85, 55, 113].

Chapter 7

Bragg Scattering

In recent years Bragg scattering has become an increasingly important tool in cold atom physics. Its popularity can be attributed to its dual role as both an atom-optical and spectroscopic instrument. This dual role was established early on by two papers: In M. Kozuma et al. [60] Bragg scattering was used to coherently manipulate matter waves. Their rudimentary use of Bragg scattering for coherent beam splitting advanced the field of coherent atom optics and led to the development of nonlinear atom optics. J. Stenger et al.[94] established Bragg diffraction as a tool for condensate diagnostics. Here a measurement of the Bragg spectrum confirmed that the coherence length of the condensate is equal to its physical size [94]. Oftentimes experiments employ both aspects of Bragg, first using it to prepare the condensate in some initial state and then using it to "readout" the response of the system. An example is found in ref [102], where phonons were first imprinted with Bragg diffraction, and then their excitation spectrum was measured using another set of Bragg beams.

7.1 Bragg Scattering: A Practical Guide

This chapter is intended to give the basics of Bragg[1] for those interested in simple theory and experimental techniques. The results are general and, therefore, appli-

[1]Here I begin to use the colloquialism "Bragg" to encompass both Bragg processes (i.e. scattering and spectroscopy), which are fundamentally the same.

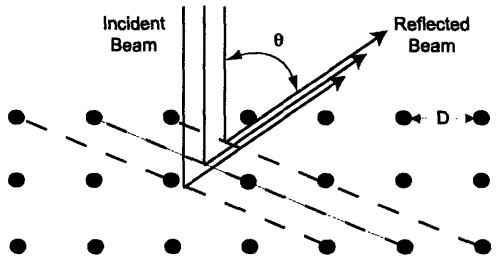

Figure 7-1: Bragg scattering of x-rays from a crystal. Due to superposition, x-rays reflected from the crystal planes constructively interfere only at certain angles. This same effect was demonstrated by Davisson and Germer (1927) using an electron beam, offering definitive proof of the wave nature of matter.

cable to atoms and molecules alike. The use of Bragg diffraction as a spectroscopic tool is discussed in detail. Included are discussions of line shifts and broadenings, both fundamental and technical. In addition, experimental techniques to limit noise are covered. This section is by no means a complete discussion of Bragg scattering. Rather, it is a summary of important results and technical issues that I found useful in our study of coherent molecular optics (see Chapter 8). For a review of the basic theory of Bragg scattering, I refer readers to ref [38]. A discussion of Bragg spectroscopy in the phonon regime can be found in ref [91].

In the most general sense, Bragg scattering arises from the diffraction of waves from a grating. Because waves superpose, there are only certain scattering angles at which they interfere constructively. This is true for both light and matter. However, because the Bragg diffraction of condensates employs gratings created by standing light waves, a second picture arises to describe the system: Bragg scattering as a stimulated Raman process. Both pictures are equally valid and rely on the same basic principles of energy and momentum conservation. However, for clarity, I will focus on the latter picture because coherent atom optics follows more naturally.

7.1.1 Grating Picture

Bragg scattering of matter waves is by no means a new technique. It has its roots in two important experiments from the early 20th century. In 1912 M. von Laue

and later W.L. Bragg demonstrated that the wavelength of x-rays could be measured by studying their diffraction from a crystal. Due to the wave nature of light, x-rays were observed to scatter only at certain angles given by the Bragg condition for constructive interference

$$n\lambda = Dsin\theta \tag{7.1}$$

where n is an integer and D is the atomic spacing (see Fig. 7-1). In 1927 C.J. Davisson and L.H. Germer used this same method to test de Broglie's hypothesis that *matter* also possesses wave-like properties. Using a monoenergetic electron beam, they observed the same directional scattering effect as had been demonstrated with light. In the words of Davisson and Germer [21]:

Because of these similarities between the scattering of electrons by the crystal and the scattering of waves by three- and two-dimensional gratings a description of the occurrence and behavior of the electron diffraction beams in terms of the scattering of an equivalent wave radiation by the atoms of the crystal, and its subsequent interference, is not only possible, but most simple and natural.

In essence, the result is explainable if one attributes a wavelength to the electrons. Furthermore, by changing the energy of their source, Davisson and Germer also confirmed the de Broglie wavelength relationship $\lambda_{dB} = h/p$, where p is the particle's momentum.

Bragg diffraction of atoms was demonstrated shortly thereafter (1930) [29]. However, only recently (1987) has it become a practical atom optical tool, with scattering from optical gratings demonstrated first with thermal atoms [69] and subsequently BEC [60]. In their simplest form, these optical gratings consist of two laser beams of wavelength λ_L, which form a standing wave of periodicity $\lambda_L/2sin(\theta/2)$, where θ is the angle between the beams. However, because condensates are produced in static traps, it is more straightforward to move the grating rather than the BEC. This is accomplished by applying a small, relative detuning, δ, between the beams. As a

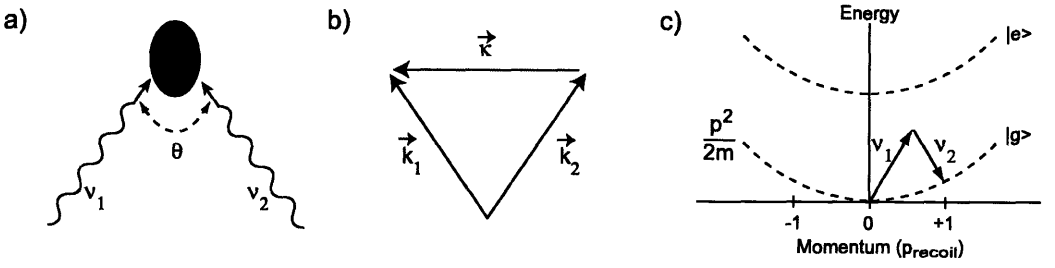

Figure 7-2: Bragg Scattering viewed as a stimulated Raman transition. a) Two beams with frequencies ν_1, ν_2 illuminate the condensate. b) The momentum imparted to the condensate is equal to the difference in momenta, $\hbar\vec{\kappa}$, between photons in the two beams. c) Transitions to higher momentum states occur only if $\vec{k}_1, \vec{k}_2$ are chosen such that energy and momentum are conserved.

consequence of energy conservation, scattering only occurs if the atoms' speed in the grating frame is conserved in the process (The condition for specular reflection).

7.1.2 Raman Picture

As stated earlier, Bragg scattering from an optical grating can also be viewed as a stimulated Raman transition between *momentum* states (see Figure 7-2). One can think of this process as an atom absorbing a photon from one beam and then being stimulated to emit into the other.[2] The difference in momenta between these two photons $\hbar\vec{\kappa}$, is transferred to the recoiling atom.

From Figure 7-2b we see that the recoil momentum and energy are given by[3]

$$\hbar\vec{\kappa} = \hbar(\vec{k}_1 - \vec{k}_2) = 2\hbar k sin(\theta/2)\hat{\kappa} \tag{7.2}$$

$$h\delta = h(\nu_1 - \nu_2) = \frac{2\hbar^2 k^2}{2m} sin^2(\theta/2) \tag{7.3}$$

where $k = 2\pi/\lambda_L$ is the photon wavenumber. Thus, the condition for Bragg scattering

[2]Strictly speaking, the correct view of this process is one of paired stimulated absorption and emission, resulting in the redistribution of a photon between the two beams.

[3]Here we approximate $|\vec{k}_1| = |\vec{k}_2| = k$, which is justified because $\delta \sim 100$ kHz, compared to the optical frequency of ~ 500 THz.

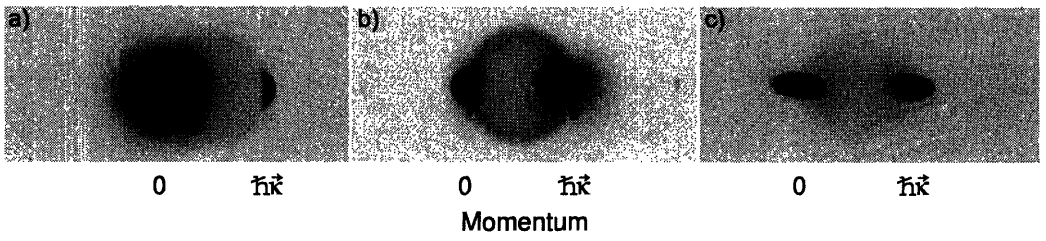

Figure 7-3: Bragg diffraction of a BEC. Time-of-flight images represent a momentum analysis of the condensate. Because the kinetic energy of the scattered atoms is much larger than the mean-field energy of the condensate, the momentum states are well-resolved in time-of-flight. a) The Bragg pulse scatters a fraction of the condensate into $\hbar\vec{\kappa}$ momentum state. (The image is taken in the plane of the Bragg beams.) b) By choosing the pulse duration correctly one can make a "50/50 beamsplitter" for matter waves. c) Out-of-plane view of the "50/50 beamsplitter". The halos are caused by collisions between the two momentum states [17]. From (c) it is evident that atoms on the inner edges undergo more collisions. This is to be expected because the two regions interact with one another longer.

is

$$\nu_0 = \frac{2h}{m\lambda^2} sin^2(\theta/2) \tag{7.4}$$

Of course, this derivation assumes that the atoms were at rest. For atoms moving with velocity $\vec{v}_i$, the resonance condition is

$$h\nu = h\nu_0 + \hbar\vec{\kappa} \cdot \vec{v}_i \tag{7.5}$$

where the second term represents the Doppler shift ($\delta\nu_m = \hat{\kappa}/\lambda_L \cdot \vec{v}_i$) of the resonance due to motion. The inclusion of this term illustrates the velocity selectivity of atomic Bragg diffraction and foreshadows its use as a spectroscopic tool.

7.1.3 Coherent Population Transfer

Based on the stimulated Raman picture, coherent population transfer between momentum states is expected. Assuming coupling only between the $|0\rangle$ and $|\hbar\vec{\kappa}\rangle$ momentum states, the system behaves like a two-level system. Thus, for a given pulse

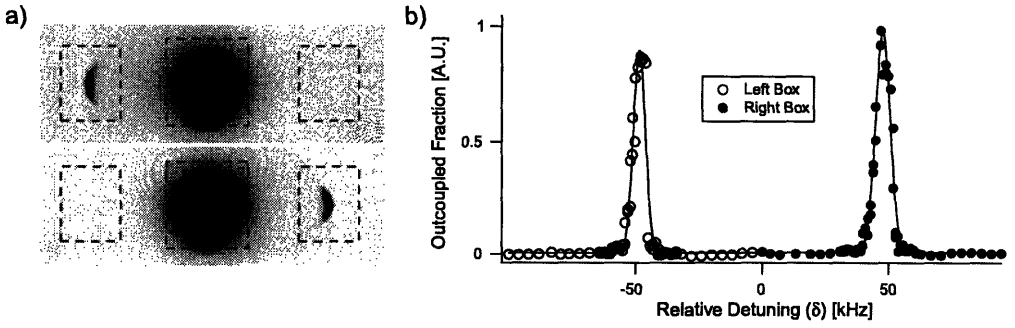

Figure 7-4: Bragg spectrum of a trapped condensate. (a) The spectrum is obtained by varying the relative detuning δ of the Bragg beams. The sign of δ determines the direction of scattering. For each image the number of particles in all three boxes are counted. The outcoupled fractions are determined by taking the ratio of particles in the left and right boxes to the center. (b) The locations and widths of the resonances result from a combination of mean-field interactions and finite size effects.

duration τ, the population of the excited state $|\hbar\vec{\kappa}\rangle$ is

$$P_e(\tau) = \frac{\omega_{r(2)}^2}{\Omega_{r(2)}^2} sin^2\left(\frac{\Omega_{r(2)}\tau}{2}\right) \tag{7.6}$$

where $\omega_{r(2)}$ is the two-photon Rabi rate and $\Omega_{r(2)} = \sqrt{\omega_{r(2)}^2 + [2\pi(\delta - \nu_0)]^2}$. Thus, the population will undergo coherent oscillations between the two momentum states at frequency $\Omega_{r(2)}$. By varying τ arbitrary populations can be produced in each state. On resonance ($\delta - \nu_0 = 0$) the Bragg beams act as a "50/50 beamsplitter" for $\tau = \pi/2\Omega_{r(2)}$ (see Figure 7-3b,c).

The treatment above must be qualified. As we shall see, atoms in a condensate have a distribution of energies and velocities. Thus, the Bragg beams do not address the entire condensate uniformly. Because of this, atoms in different regions of the condensate oscillate at slightly different Rabi frequencies. After many cycles, one expects equal populations in both states. In addition, collisions between the two states (see Figure 7-3) cause further decoherence.

7.2 Bragg Spectroscopy

Figure 7-4b shows a typical Bragg spectrum. The spectrum is taken by varying the relative detuning δ, and then measuring the fraction of outcoupled atoms. The sign of δ dictates the direction in which atoms are diffracted. By using both positive and negative detunings two resonances are observed.

Evident from Figure 7-4b, Bragg transitions have a finite width. Eq(7.5) hints that this width may result from a distribution of velocities in the condensate (see Figure 7-5a). As we shall see, mean-field interactions also contribute to the width. Therefore, to characterize the system accurately, it is important to understand how these effects, and others, can both broaden and shift the spectrum.

7.2.1 Width of a Thermal Distribution

The onset of Bose-Einstein condensation is characterized by a sudden narrowing of the atomic momentum distribution. For later comparison, it is useful to find the frequency width $\Delta\nu_T$ of a thermal distribution at temperature T. From kinetic theory

$$k_B T = m v_{rms}^2 \tag{7.7}$$

where v_{rms} is the RMS velocity. From Eq(7.5) we see that atoms moving at v_{rms} are Doppler shifted by the width of the resonance $\Delta\nu_T$

$$\hbar\vec{\kappa} \cdot \vec{v}_{rms} = h\Delta\nu_T \tag{7.8}$$

Thus, for a given temperature, the width of the distribution is

$$\Delta\nu_T = \sqrt{\frac{2k_B T}{m}} \frac{\sin(\theta_B/2)}{\lambda_L} \tag{7.9}$$

7.3 Broadening Mechanisms

Broadening mechanisms can be separated into two categories: fundamental and technical. Fundamental broadening is inherent to the system. For condensates, there are two contributors to the fundamental width $\Delta\nu_F$: the finite sample size and the mean-field. Both factors are related to the inhomogeneous density distribution of the trapped condensate. Technical broadening is caused primarily by random motion of the condensate and, in some cases, the finite duration of the Bragg pulses. With care, contributions from technical noise can be made insignificant.

To understand how each mechanism contributes to the total width, we must first consider how broadening mechanisms combine with one another. For simplicity we limit the discussion to gaussian distributions.[4] Consider the case of a transition of width γ and a probe beam of width δ. The measured lineshape $I(\nu)$ is the convolution of the two,

$$I(\nu) \propto \int_{-\infty}^{\infty} e^{-\frac{\nu^2}{\gamma^2}} e^{-\frac{(\nu+\varepsilon)^2}{\delta^2}} d\varepsilon \propto e^{-\frac{\nu^2}{\gamma^2+\delta^2}} \tag{7.10}$$

Thus, we expect that contributions from unrelated mechanisms to add to width in quadrature.

7.3.1 Finite-Size Broadening

Heisenberg's uncertainty relation requires that a sample with coherence length χ_c has a momentum spread given by $\Delta p \cdot \chi_c \sim \hbar$. Therefore, even if the coherence length is the size of the sample (as is the case for a condensate), the Bragg transition will still be Doppler broadened. To determine a precise value for the momentum width, we must account for the particular density distribution. For a condensate, the momentum distribution is given by

$$g(p_x) \propto \int dp_y dp_z \left| \int \Psi(\vec{r}) e^{i\vec{p}\cdot\vec{r}} d^3\vec{r} \right|^2 \tag{7.11}$$

[4]For our purposes this will be sufficient because the lineshapes of interest are well approximated by gaussian distributions.

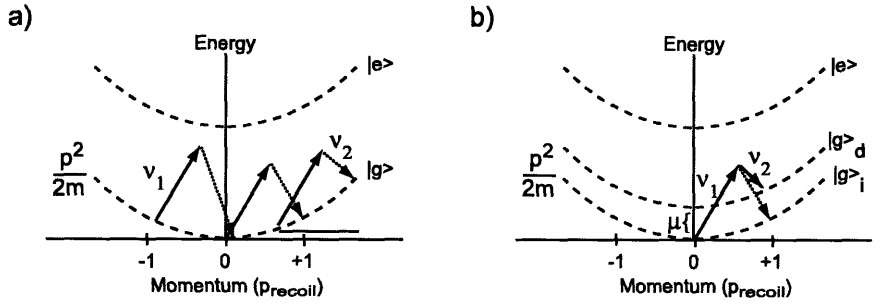

Figure 7-5: Broadening mechanisms for Bragg transitions. a) Atoms moving with different velocities require different frequencies ν_2 to complete the transition. The width of the Bragg transition, therefore, depends on the velocity distribution. b) Mean-Field Broadening. Because distinguishable particles experience twice the mean-field repulsion, the frequency at which the transition occurs is shifted. The transition is broadened as well because mean-field interactions are not uniform throughout the condensate (possibly show lines?).

Fitting a gaussian to this lineshape yields an rms width[5] of [95]

$$\Delta\nu_p = 3.16\frac{\hbar\sin(\theta_B/2)}{m\lambda_L x_0} \tag{7.12}$$

where x_0 is the Thomas-Fermi radius in the direction $\hat{\kappa}$.

7.3.2 Mean-Field Broadening

The dispersion relation for a weakly interacting uniform condensate is [48]

$$\nu = \sqrt{\nu_0^2 + 2\nu_0 nU/h} \tag{7.13}$$

where n is the particle density, U=$4\pi\hbar^2 a/m$, m is the atomic mass, and a the scattering length. For energies $h\nu \gg nU$, the excitation spectrum is particle-like (quadratic in momentum)

$$\nu = \nu_0 + nU/h \tag{7.14}$$

[5]In all cases we use the rms width σ as the figure of merit, defined by the normalized distribution $f(\nu) = \frac{1}{\sqrt{2\pi\sigma^2}}e^{-\frac{\nu^2}{2\sigma^2}}$

The mean-field shift nU/h results from the repulsion of excitations by the condensate. Distinguishable atoms experience twice the mean-field of condensed atoms [57]. Therefore, scattered atoms originating in the condensate (indistinguishable) ground state $|g\rangle_i$ end up in a distinguishable ground state $|g\rangle_d$, resulting in an overall shift of the Bragg spectrum. This effect is illustrated in Figure 7-5b.

In order to determine the shift for a *nonuniform* condensate, the inhomogeneous density distribution must be accounted for. This effect is easy to model using a local density approximation. The observed shift is simply an *average* of each individual particle's shift. Recall from Chapter 1 that the (normalized) density distribution of the condensate is given by

$$I(n) = \frac{15n}{4n_0}\sqrt{1-\frac{n}{n_0}} \tag{7.15}$$

where n_0 is the peak density. Using Eq(7.14), we replace the density n with the local density $h(\nu-\nu_0)/U$,

$$I(\nu) = \frac{15h(\nu-\nu_0)}{4n_0U}\sqrt{1-\frac{h(\nu-\nu_0)}{n_0U}} \tag{7.16}$$

The line shift is then given by the first moment

$$\delta\nu_n = <\nu> = \int \nu I(\nu)d\nu = \int \frac{15h\nu(\nu-\nu_0)}{4n_0U}\sqrt{1-\frac{h(\nu-\nu_0)}{n_0U}}d\nu = \frac{4n_0U}{7h} \tag{7.17}$$

In addition to the mean-field shift, the resonance is also broadened. This results from a smearing of the individual particle shifts caused by inhomogeneous mean-field interactions. The rms width is given by the second moment

$$\Delta\nu_n = \sqrt{<\nu^2> - <\nu>^2} = \sqrt{\frac{8}{147}}\frac{n_0U}{h} \tag{7.18}$$

7.3.3 Pulse Broadening

As demonstrated in 7.3, the probe itself contributes to the measured linewidth. The instrumental resolution is limited by the fourier spectrum of the pulse. The shorter the pulse duration, the broader the frequency distribution. Indeed, for short enough

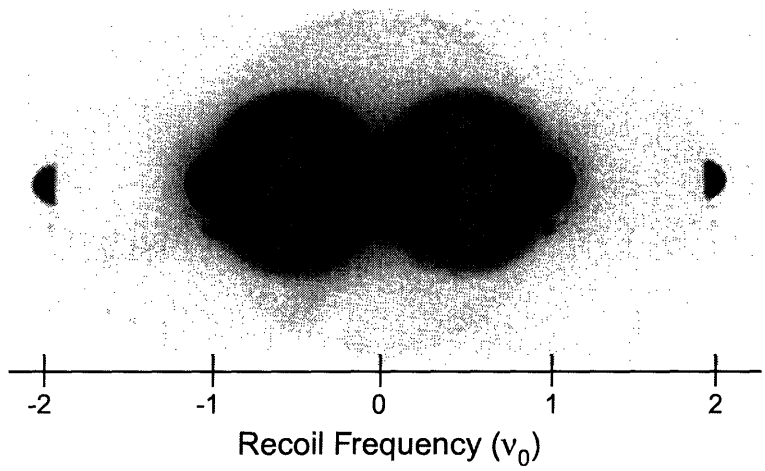

Figure 7-6: Kapitza-Dirac scattering of a BEC. Multiple momentum states are populated due to the broad frequency distribution of a short Bragg pulse (2 μs). The recoil frequency is $\nu_r \simeq 45$ kHz, while the pulse has frequency width $\Delta\nu_{pulse} \simeq 175$ kHz.

pulses, Bragg processes populate multiple momentum states (see Figure 7-6). This is known as the Kapitza-Dirac regime. For high resolution spectroscopy, it is important to quantify the probe resolution so that a suitable pulse duration can be chosen.

Figure 7-7 illustrates the instrumental resolution of Bragg. The beams are typically flashed on at fixed intensity for time τ, such that the average electric field is $\bar{E}(t) = E_0 f(t)$, where

$$f(t) = \begin{cases} f_0 & -\tau/2 \leq t \leq \tau/2 \\ 0 & Otherwise \end{cases} \tag{7.19}$$

The fourier transform of $f(t)$ gives the field amplitude in frequency space, $\bar{E}(\nu) = E_0 g(\nu)$, where

$$g(\nu) \propto \frac{sin(\pi\nu\tau)}{\nu} \tag{7.20}$$

The intensity $I(\nu)$ in frequency space is proportional to $|g(\nu)|^2$. A gaussian fit to $I(\nu)$ yields rms width

$$\Delta\nu_{pulse} = \frac{1}{\sqrt{8}\tau} \tag{7.21}$$

Thus, the instrumental resolution is given by Eq(7.21). As an example, the 2 μs

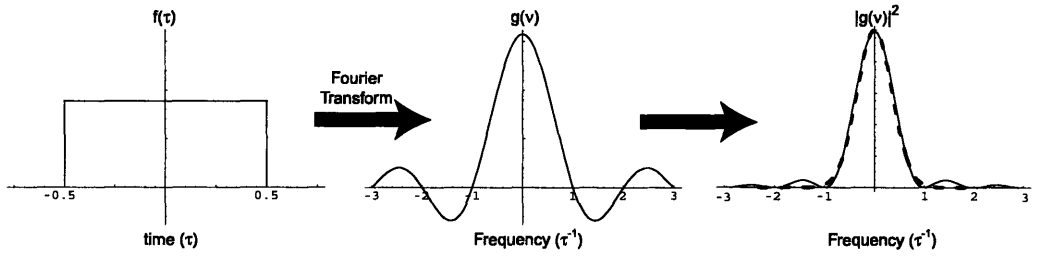

Figure 7-7: Frequency resolution of a finite pulse. For a square pulse of duration τ, the frequency distribution $g(\nu)$ is obtained by taking the Fourier transform of $f(t)$. The resolution of the pulse is obtained by fitting a Gaussian (dashed line) to $g(\nu)^2$

pulse used in Figure 7-6 has a frequency distribution of $\simeq$ 175 kHz, which is broad enough to populate momentum states separated by $\simeq$ 180 kHz. It should be noted that the pulse duration for in-trap Bragg spectroscopy should be less than a quarter trap period because initially scattered atoms will come to rest in this time. When this is the case, scattered atoms do not separate from the condensate during ballistic expansion.

7.3.4 Motional Broadening

Random center-of-mass motion from shot-to-shot will broaden the *measured* Bragg spectrum. The extent to which this motion contributes, $\Delta\nu_m$, depends on its amplitude X_{rms} ($= v_{rms}/\omega$). Following the derivation of 7.1.2 the Doppler shifted width is

$$\Delta\nu_m = \frac{2\omega_x \sin(\theta_B/2)}{\lambda_L} X_{rms} \tag{7.22}$$

7.4 Summary of Results

The important results of this chapter are given below:

The resonance condition for Bragg scattering is

$$\nu_0 = \frac{2h}{m\lambda^2} sin^2(\theta/2) \tag{7.23}$$

For a thermal distribution at temperature T the width of the Bragg resonance is

$$\Delta\nu_T = \sqrt{\frac{2k_BT}{m}} \frac{\sin(\theta_B/2)}{\lambda_L} \tag{7.24}$$

For a condensate the factors that contribute to the width of the Bragg spectrum are

$$Broadening\ Mechanisms \begin{cases} \Delta\nu_p = 3.16\frac{\hbar \sin(\theta_B/2)}{m\lambda_L x_0} & Finite\ Sample\ Size \\ \Delta\nu_n = \sqrt{\frac{8}{147}}\frac{n_0 U}{h} & Mean-Field\ Interactions \\ \Delta\nu_{pulse} = \frac{1}{\sqrt{8}\tau} & Finite\ Pulse\ Duration \\ \Delta\nu_m = \frac{2\omega_x \sin(\theta_B/2)}{\lambda_L} X_{rms} & Random\ Motion \end{cases} \tag{7.25}$$

In principle the overall width should be the quadrature sum of these values.

Factors that lead to a shift of the Bragg spectrum are

$$Shifting\ Mechanisms \begin{cases} \delta\nu_n = \frac{4n_0 U}{7h} & Mean-Field\ Interactions \\ \delta\nu_m = \frac{v}{\lambda_L} & Reproducible\ Motion \end{cases} \tag{7.26}$$

a : *Scattering Length*	λ_L : *Laser Wavelength*	m : *Mass*
n_0 : *Peak Density*	θ_B : *Beam Angle*	τ : *Pulse Duration*
T : *Temperature*	U : *Interaction Parameter* $(4\pi\hbar^2 a/m)$	v : *Velocity*
ω_x : *Radial Trap Frequency*	X_{rms} : *Oscillation Amplitude*	x_0 : $T-F$ *Radius*

Table 7.1: Notation

7.5 Discussion of Results

Typically, condensate parameters such as atom number N and peak density n_0 are determined by measuring the size of the sample in time-of-flight X_{tof}. The Thomas-Fermi radius is then given by [14][6]

$$x_0 = \frac{X_{tof}}{\sqrt{1+(\omega_x t)^2}} \tag{7.27}$$

where t is the time-of-flight. x_0 and ω_x provide us with everything we need to characterize the condensate.[7]

An interesting result from 7.3.2 is that the mean-field shift $\delta\nu_n$ depends explicitly only on the peak density. Therefore, measurements of $\delta\nu_n$ provide an alternate means for measuring condensate parameters.[8] Recasting the the peak density and size in terms of the shift yields

$$n_0 = \frac{7h}{4U}\delta\nu_n \tag{7.28}$$

$$x_0 = \sqrt{\frac{7h}{2m\omega_x^2}\delta\nu_n} \tag{7.29}$$

Of course, it is much easier to measure the size of the cloud than to take an entire Bragg spectrum. The real value in determining $\delta\nu_n$ is that it provides a useful check for the validity of the Bragg spectrum.

7.6 Putting it all Together: A Real Example

With the features of the spectrum now well-characterized, we turn our attention to a real example. From fits to the spectrum in Figure 7-4b, the following experimental

[6]This assumes a purely 2-D expansion, characteristic of the cigar-shaped condensates we typically use.

[7]The trap frequency is typically measured by inducing dipole motion of the condensate and then measuring the ensuing oscillation frequency. Of all the parameters we measure, this is usually the best known.

[8]This requires that both $\pm\delta$'s are used so that any shift due to reproducible motion of the condensate is removed by using the *average* shift.

values were extracted for the shift and width, respectively:

$$\delta\nu_{Exp} = 3.75 \text{ kHz} \qquad \Delta\nu_{Exp} = 2.5 \text{ kHz}$$

As discussed above, we first check that the condensate parameters found via the shift $\delta\nu_{Exp}$ agree with those found in time-of-flight. Table 7.2 shows that these two methods compare favorably, giving us confidence in the spectrum.

Parameter	TOF	M-F Shift
x_0 (μm)	**14.4**	16.2
n_0 (10^{14} cm^{-3})	4.04	4.32
N (10^6)	22.5	27.8
$\delta\nu_n$ (kHz)	3.5	**3.7**
$\Delta\nu_n$ (kHz)	1.4	1.5
$\Delta\nu_p$ (kHz)	0.62	0.60
$\Delta\nu_F$ (kHz)	1.5	1.6

Table 7.2: Comparison of condensate parameters using time-of-flight (TOF) analysis and the mean-field (M-F) shift. Bold values represent the measured parameter. (Strictly speaking x_0 is not directly measured, rather, it is found using $X_{tof} = 580\mu$m, $t = 40$ ms and $\omega_x = 2\pi\times146$ Hz.)

Next, we compare the measured width $\Delta\nu_{Exp}$ to that of a thermal distribution near the critical temperature T_c. For a typical value of $T_c \sim 1$ μK, the width of a thermal sample is $\Delta\nu_T = 30$ kHz, much larger than our measured width. As we shall see (in direct analogy to a laser), the narrow linewidth of the condensate is indicative of high spatial coherence.

For a perfect condensate the coherence length χ_c should equal the size of the sample x_0. χ_c is experimentally determined by subtracting out contributions to $\Delta\nu_{Exp}$ from mean-field interactions and pulse broadening. Ideally, the remaining width is accounted for by the finite-size broadening. In practice this may not be the case. Thus, the remaining width sets a lower bound on the coherence length

$$\chi_c \geq \frac{\Delta\nu_p}{\sqrt{\Delta\nu_{Exp}^2 - \Delta\nu_n^2 - \Delta\nu_{pulse}^2}} x_0 \tag{7.30}$$

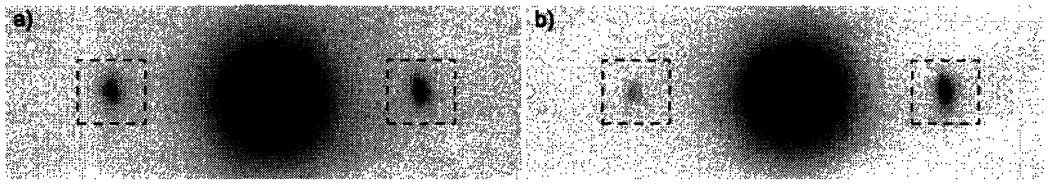

Figure 7-8: Doppler broadening caused by random motion. In these images each Bragg beam has both frequencies mixed in. (a) The ratio of out-coupled atoms should be unity. (b) Some shots, however, show asymmetric out-coupling due to motion of the condensate. Unless shots like this are discarded, the *measured* Bragg spectrum will be broadened.

The pulse duration used in this example was $\tau = 200$ μs. Using Eq(7.21) and the values from Table 7.2 we find that $\chi_c \simeq 0.66 x_0$ or ~ 10 μm.[9] This measurement demonstrates high spatial coherence over the sample and the existence of a macroscopic de Broglie wave. However, if we assume that the coherence length is indeed the sample size, then there is 700 Hz of width unaccounted for.

7.7 Noise Rejection

The unaccounted for width in our Bragg spectrum is most likely due to Doppler broadening caused by random center-of-mass motion and other collective excitations. A line broadening of 700 Hz corresponds to a vibrational amplitude of only $\simeq 0.35$ μm (compared to $x_0 = 14$ μm). Therefore, it seems likely that this width is attributable to random motion. This possibility was investigated by mixing both frequencies ν_1, ν_2 into each Bragg beam to out-couple particles in both $\pm$x directions. For particles at rest, the out-coupling should be symmetric. However, we observed the ratio of out-coupled particles to fluctuate (see Figure 7-8).

Doppler broadening caused by random motion can, in principle, be eliminated using the two-frequency technique described above. Discarding data in which the out-coupled ratio falls outside a certain bandwidth should improve spectroscopic resolution. The bandwidth should be narrow enough such that $\Delta\nu_m$ is small compared

[9] J. Stenger *et al.* [94] measure a coherence length of $0.8 x_0$.

to the finite size width $\Delta\nu_p$, but not so small as to require Herculean data collection. Finally, it must be noted that this method fails if the spectrum is shifted by reproducible motion $\delta\nu_m$. Because of this shift, one cannot expect symmetric outcoupling. This effect plagued our measurement of the molecular Bragg spectrum (see Chapter 8) [3]. In this case a stray magnetic field provided a reproducible kick to the molecules upon their creation. This effect can be compensated for with some extra effort. This requires providing frequencies ν_1,ν_2 to one beam and ν_1,$\nu_2 + \delta\nu_m$ to the other to compensate for the shift.

Chapter 8

Coherent Molecular Optics

The unprecedented intensity and coherence properties of lasers have led directly to the observation of effects such as wave-mixing and parametric down-conversion. Similarly, atom and molecular optics have benefitted greatly from the realization of Bose-Einstein condensates (BEC). High phase-space density (particles per mode) and uniform spatial phase give the condensate laser-like qualities, opening the door for studies of nonlinear and quantum particle optics.

This chapter supplements work reported in the following publication:

J.R. Abo-Shaeer, D.M. Miller, J.K. Chin, K. Xu, T. Mukaiyama, and W. Ketterle *"Coherent Molecular Optics using Sodium Dimers,"* cond-mat/0409327 (2004).

(Included in Appendix E) Ref [3]

8.1 Optics

Recent developments in atom/molecular optics parallel the revolution that took place in conventional optics after the invention of the laser. Indeed, many useful analogies between the two fields can be drawn. With this in mind, I begin the chapter with a discussion of the key features of conventional optics, before turning my attention to atom optics and finally molecular optics.

8.1.1 Conventional Optics

The field of optics underwent a dramatic shift midway through the twentieth century. Prior to the invention of the laser (1960), optics consisted mainly of two subfields: ray and wave optics. Ray optics has, in some sense, been understood since the dawn of man, evident in phenomena such as the bending and reflection of light by water.[1] In ray optics coherence plays no role. Rather, light behaves as small particles (photons) that move in straight-line trajectories. This picture is sufficient for describing reflection and refraction, the basis of geometric optics.

Wave optics describes phenomena in which photons travel in "lockstep" with one another. Unlike particles, waves overlap, adding constructively and destructively. Similar to ray optics, the wave nature of light is manifest in everyday life such as thin-film interference on a soap bubble. However, effects such as this are more subtle. It was not until 1803 that T. Young's double slit experiment gave conclusive evidence for the wave-nature of light.

The key differences between a laser and thermal source are its intensity and coherence. These features produce remarkable effects that have led to the development of two new subfields of optics: nonlinear[2] and quantum optics. Nonlinear optical phenomena such as wave-mixing, result from the interaction of light with matter. In free space photons do not interact with one another. However, in materials there can be an effective photon interaction, caused by an intensity dependent index of refraction. Frequency doubling was the first qualitatively new nonlinear optical effect observed using lasers (1961) [34]. Here a crystal irradiated with an intense pulse of red laser light produced a small amount blue light at twice the input frequency. Frequency doubling is a specific example of the more general process of sum-frequency generation, where two light waves mix to create a third wave at the sum frequency.

Quantum optics deals partly with study of nonclassical light fields. Nonclassi-

[1] Primitive fishermen, for example, realized that they had to aim their spears at a sharper angle than they perceived to make their catch.

[2] Strictly speaking, some nonlinear phenomena such as the D.C. Kerr effect (1875) were observed before the advent of the laser. However, the full potential of nonlinear optics was not realized until the invention of the laser.

Subfield:	Ray	Wave	Nonlinear	Quantum
Photons are:	Particles	Waves	Interacting	Correlated
Verification:	Fish Spearing (Dawn of Man)	Two-Slit Interference (1802)	DC Kerr Effect (1875)	Parametric Down-Conversion (1970)
Phenomena:	Reflection Refraction	Interference Diffraction	Wave-Mixing Induced Birefringence	"Squeezed" Light Anti-Bunching
Requirements:	---	Coherent Light	Intense Fields	Intense Fields/ Coherent Light
Source:	Thermal	Thermal	Laser	Laser
Tools:	Lenses	Gratings	Nonlinear Media	Nonlinear Media

Figure 8-1: Key Features of conventional optics.

cal light can be generated via parametric down-conversion [12], the inverse process of sum-frequency generation. In this case, photons travelling through a material are split in two. This splitting is, however, fundamentally different from that of a beamsplitter. Beamsplitters are governed by poissonian statistics, which requires a minimum uncertainty in the number of photons in each arm. In parametric down-conversion energy and momentum conservation make the resultant photons emerge strongly correlated, with complementary direction and frequency. This "squeezing" of number fluctuations can produce measurements below the shot-noise limit.

The key features of each subfield of conventional optics are summarized in Figure 8-1.

8.1.2 Atom Optics

Ray atom optics concerns itself only with the particle nature of atoms. Although these properties are well-understood, considerable effort is still devoted to the field, partly for its applications to cold atom physics. Recent experiments have demonstrated novel tools for the manipulation of atoms, including atomic mirrors, waveguides, conveyor belts, and BEC Chip experiments [46, 24, 74, 59, 43, 42, 64].

Wave atom optics has its roots in the pioneering work on crystal diffraction from

the early 20th century. Davisson and Germer used this technique to demonstrate matter-wave interference of electrons (1927)[22]. Shortly thereafter, J. Estermann and O. Stern used crystal diffraction to prove that more massive objects (He atoms) also propagate as waves (1930)[29]. Unfortunately, most atoms tend to stick to surfaces rather than reflecting off or passing through them. Therefore, Bragg diffraction did not become a useful atom-optical tool until much later (1987) [82], when atoms were demonstrated to diffract from standing light waves [69] and nanofabricated gratings [56] .

Until recently, atom optics experiments were limited to single-particle phenomena where interactions between particles could be neglected. However, in 1993 a new regime was considered in which interactions play a crucial [66]. For sufficiently dense samples atomic mean-field interactions can play the role of a nonlinear medium. Indeed, the Gross-Pitaevskii equation (the nonlinear Schrodinger equation used to describe condensates) is similar in form to a certain class of wave equations governing nonlinear optics [6]. Nonlinear atom optics has benefitted greatly from the realization of Bose-Einstein condensates (BEC). High phase-space density (atoms per mode) and a uniform phase [94, 40] give the condensate laser-like qualities. Although not fundamentally required [75, 58], BEC has led to the observation of such nonlinear phenomena as four-wave mixing [23] and matter wave amplification [51, 61]. In addition, quantum atom optic effects such as atom number squeezing have also been observed [80, 37].

The key features of atom optics are summarized in Figure 8-2. Note the similarities to Figure 8-1.

8.2 Molecular Optics

The current state of molecular optics is similar to atom optics prior to the realization of BEC. Diffraction and interferometry of thermal molecular beams has been demonstrated [11, 15, 39, 88], yet monoenergetic beams lack the density necessary to observe nonlinear effects. However, recent experiments using Feshbach resonances

Subfield:	Ray	Wave	Nonlinear	Quantum
Atoms are:	Particles	Waves	Interacting	Correlated
Verification:	Democritus' Atom & Void (500 BC)	He Diffraction (1930)	4-Wave Mixing (1999)	Atom Number Squeezing (2001)
Phenomena:	Reflection Refraction	Interference Diffraction	Wave-Mixing Solitons	"Squeezed" Atoms Entanglement
Requirements:	---	Coherent Atoms	High Density	High Density/ Coherent Atoms
Source:	Thermal	Thermal	BEC	BEC
Tools:	E-M Fields	Gratings	Mean-Field Interactions	Mean-Field Interactions

Figure 8-2: Key Features of atom/molecular optics.

have demonstrated the conversion of degenerate atomic bosons [28, 45, 107] and fermions [85, 55, 113, 18, 96] into ultracold molecules. These sources have the potential to greatly advance molecular optics. Furthermore, atom-molecule coupling can be studied as the first steps towards "superchemistry", where chemical reactions are stimulated via macroscopic occupation of a quantum state [44].

Here we demonstrate the ability to apply Kapitza-Dirac and Bragg diffraction [60] to cold molecules. Using optical standing waves of suitably chosen frequencies, sodium dimers were coherently manipulated with negligible heating or other incoherent processes. First, we characterized the coherence of our "source" molecules, created via Feshbach resonance. By measuring the Bragg spectrum of the molecules immediately after their creation, the conversion from atoms to molecules was shown to be coherent - the matter wave analog to frequency doubling in optics. The quadratic spatial dependence of the phase of the expanding molecules was observed using an autocorrelation interference technique. By creating a duplicate sample of molecules and overlapping it with the original, matter wave interference was observed. Finally, the matter wave analog to sum-frequency generation was demonstrated. Atoms prepared in two momentum states, prior to creating molecules, were observed to cross-pair, generating a third momentum state.

8.3 Bragg Diffraction of Molecules

The theory and experimental techniques underlying Bragg diffraction are discussed in detail in Chapter 7. The following touches upon the main points of the Appended text.

Figure 8-3 shows time-of-flight images of Bragg scattering for atoms and molecules. Because the kinetic energy of the scattered particles was much larger than their mean-field energy, individual momentum states were well-resolved in ballistic expansion. Both atoms and molecules receive equal two-photon recoil momentum, $p_r = 2h\sin(\theta_B/2)/\lambda_L$, where λ_L is is the wavelength of the Bragg beams. However, scattered molecules move away from the central peak with half the velocity of atoms, owing to their doubled mass. Figure 8-3c,d show Kapitza-Dirac scattering, where multiple atomic and molecular momentum states were populated due to the broad frequency distribution of the short pulse (5 μs).

8.4 Characterization of the "Source"

Furthering the analogy between conventional optics and atom optics, the conversion of atoms to molecules may be viewed as the atom optic equivalent of frequency doubling [89]. Indeed, the relevant Hamiltonian for atom-molecule coupling has the same form as that for the optical frequency doubling process:

$$a_{2m}^{\dagger} a_m a_m \tag{8.1}$$

where a_m is the annihilation operator for the atomic field and $a_{2m}^{\dagger}$ is the creation operator for the molecular field.

Here we apply the technique of Bragg spectroscopy to measure the linewidth of a molecular sample. The goal is to gain insight into the process of molecule creation. Does the Feshbach process preserve the coherence of the sample? Or, to put it another way, does a frequency doubled atom laser inherit the linewidth of the source?

The linewidth of a coherent light source is typically measured by scattering it from

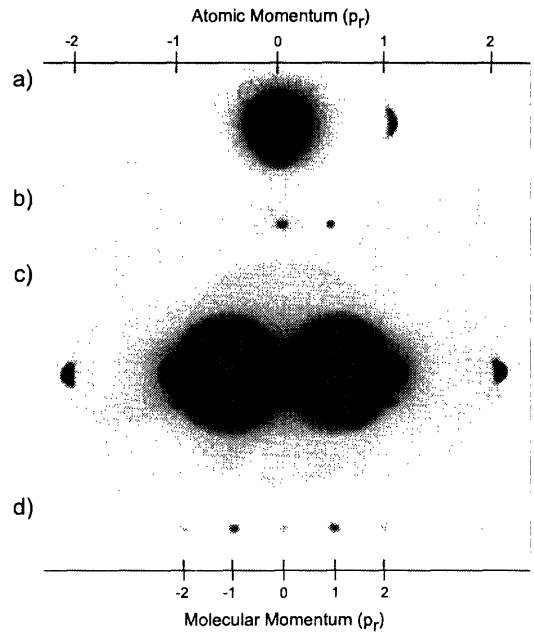

Figure 8-3: Bragg diffraction of (a) atoms and (b) molecules. Scattered particles recoil with identical momenta, p_r. However, during ballistic expansion diffracted molecules expand with half the velocity of atoms, due to their doubled mass. The pulse duration in each image was 200 μs. A shorter pulse (5 μs) populated multiple (c) atomic and (d) molecular momentum states. The halos in (c) are due to collisions between different momentum states [17]. The time-of-flight in each image is 17 ms.

a grating. It is easy to show that monochromatic light will only be diffracted at certain angles given by the Bragg condition $n\lambda = Dsin\theta$, where D is the grating spacing and n is an integer. However, because the source is not perfectly monochromatic, the Bragg condition is actually satisfied over some range of angles $\delta\theta$. The linewidth is then $\delta\lambda = D\delta\theta/\mathrm{n}$. In the same way, the linewidth of an "atom laser" (condensate) can be measured by diffracting it from a light grating. The technique, known as Bragg spectoscopy, has been used to demonstrate that the coherence length of a condensate is equal to its physical size [94].

To study the coherence properties of the sample, Bragg spectra [94] were taken. Figure 8-4 shows three spectra for (a) atoms above the Feshbach resonance, as well as (b) atoms and (c) molecules after sweeping through the resonance. Atoms below the resonance coexisted with a small fraction of molecules (2%). As expected from

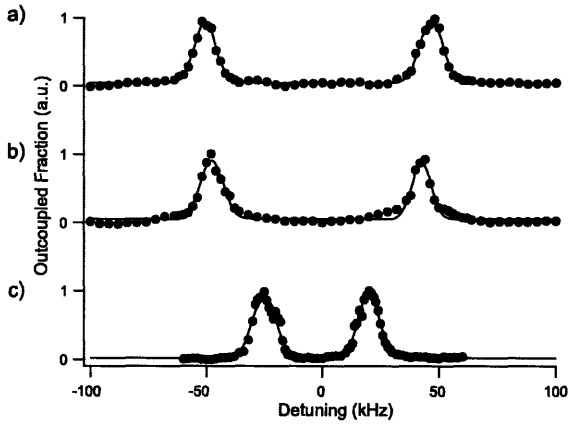

Figure 8-4: Bragg spectra for atoms and molecules. In (a) the spectrum is taken for a pure atomic sample above the Feshbach resonance. (b) and (c) are spectra of atoms and molecules, respectively, below the resonance. In (c) atoms were removed from the trap with resonant light to limit losses due to atom-molecule collisions. The Bragg resonance condition for molecules occurs at half the frequency of the atomic resonance.

the resonance condition, molecular resonances occur at half the frequency of atomic resonances.

Detailed analysis can be found in Appendix E. Suffice it to say, the width of the Bragg spectrum corresponds to a molecular temperature of 20 nK, comparable to a previous value obtained using a time-of-flight technique [107]. The BEC transition temperature for our trap parameters and 5×10^4 molecules is much higher (115 nK). This demonstrates a deeply degenerate, purely molecular sample, where as previous experiments have demonstrated coherent admixture of molecular character into an atomic BEC [25].

8.5 Sum-Frequency Generation

The measurement of the Bragg spectrum shows that the sharp "linewidth" of the seed (atom) laser is inherited by the molecular laser. In nonlinear optics, photon interactions are typically mediated by a refractive medium. Here, the nonlinearity arises from the atoms themselves, in the form of s-wave interactions. The high density,

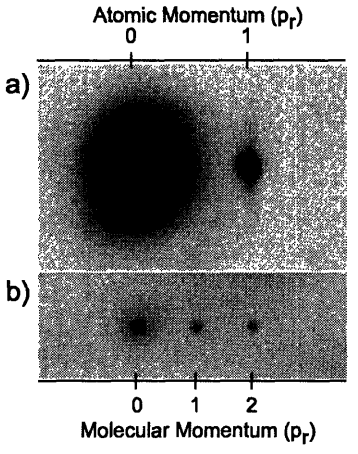

Figure 8-5: Sum frequency generation of atomic matter waves. (a) Atoms were initially prepared in momentum states 0, 1. (b) By sweeping through the Feshbach resonance, atoms combine to form molecules with momenta 0, 1, and 2. Momentum state 1 is the sum frequency of the two atomic matter waves. The "nonlinear medium" is provided by the atomic interactions. The time-of-flight in each image is 17 ms.

or "brightness", of the source, together with the enhanced interactions at the Feshbach resonance provide the means to combine two matter waves.

By combining two disparate matter waves, rather than identical ones, we extend the analogy of frequency doubling to the more general process of sum frequency generation. To do this, atoms were initially prepared in momentum states 0, 1 (in units of p_r). By sweeping through the resonance, molecules were produced in three momentum states: 0, 1, and 2 (see Figure 8-5). States 0 and 2 are simply the frequency doubled components of the two initial matter waves. State 1 however, results from cross pairing between the initial momentum states, and is thus their sum frequency. This is the first time that a Feshbach resonance was observed between atoms colliding with a controlled non-vanishing momentum. The Feshbach resonance should be slightly shifted compared to the resonance for atoms at rest, which reflects the same physics encountered in the temperature dependence of the position of the resonance [103].

8.6 Molecular Interferometery

The spatial phase of the expanding molecular cloud was directly imaged using an autocorrelation method [90], which gives rise to self-interference of the molecular sample (see Figure 8-6). To accomplish this, two identical copies of the sample were made using a short Kapitza-Dirac pulse (10 μs), applied after 2 ms of ballistic expansion. The copies, with momentum $\pm p_r$, moved away from the zero momentum peak for time Δt before an identical pulse recombined them with the original. This type of interferometer has three readout ports, with momenta 0, $\pm p_r$. The straight-line interference fringes are characteristic of a quadratic spatial phase. The fringe spacing we measure is consistent with $\lambda_f = ht/md$ [7], where $d = p_r \Delta t/m$ is the distance the copies moved between pulses.[3] Interference fringes can only be resolved for small d. Therefore, this method cannot be used to observe coherence lengths longer than those inferred from Bragg spectroscopy. It should be noted that the appearance of interference fringes does not imply that the sample is condensed. Rather, it demonstrates only that the coherence length in time-of-flight is longer than the separation d. Therefore, similar interference can also be observed for a cloud of thermal atoms [10, 73].

8.7 Conclusions and Outlook

We have demonstrated coherent molecular optics using standing light waves. The ability to coherently convert atoms into molecules makes molecular optics even richer than atom optics. These experiments demonstrate the scalable nature of atom optics and offer the promise of coherently manipulating more complex structures. In the long run this could prove useful for atom lithography and holography. In the short term the techniques demonstrated here could prove useful for probing molecules formed in quantum-degenerate fermi systems, and possibly even Cooper pairs.

[3] Strictly speaking, this analysis only applies to the outcoupled ports. The center port is comprised of three copies.

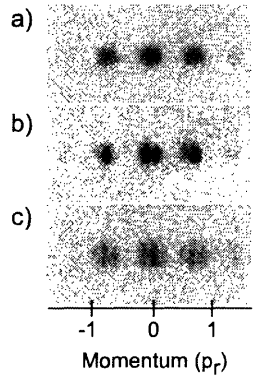

Figure 8-6: Matter wave interference of molecules. (a) The molecular sample is split with a short Kapitza-Dirac pulse, creating two identical copies with momenta $\pm p_r$. (b)-(c) After the copies have separated for time $\Delta t = 100$ μs, a second pulse recombines them, giving rise to interference in each momentum component. The time-of-flight in each image is 12 ms.

Appendix A

Observation of Vortex Lattices in Bose-Einstein Condensates

J.R. Abo-Shaeer, C. Raman, J.M. Vogels, and W. Ketterle

"Observation of Vortex Lattices in a Bose-Einstein Condensate,"

Science 292 p.476-479 (2001).

7. S. Kirkpatrick, B. Selman, *Science* **264**, 1297 (1994).
8. E. Farhi *et al.*, unpublished data.
9. L. K. Grover, *Phys. Rev. Lett.* **78**, 325 (1997).
10. E. Farhi, S. Gutmann, *Phys. Rev. A* **57**, 2403 (1998); C. H. Bennett, E. Bernstein, G. Brassard, U. V. Vazirani, *SIAM J. Comput.* **26**, 1510 (1997) (available at http://xxx.lanl.gov/abs/quant-ph/9701001).
11. A. M. Childs, E. Farhi, J. Goldstone, S. Gutmann, http://xxx.lanl.gov/abs/quant-ph/0012104.
12. Supported in part by the U.S. Department of Energy under cooperative agreement DE-FC02-94ER40818 and also by MIT's Undergraduate Research Opportunities Program. We thank the Computer Facility of the MIT Laboratory for Nuclear Science for extensive use of the computer Abacus. We benefited greatly from conversations with A. Childs, B. Selman, and L. Valiant. We also thank D. Fisher, B. Halperin, M. Kardar, and P. Lee for useful discussions about the connection of our work to statistical mechanics systems.

27 November 2000; accepted 19 March 2001

Observation of Vortex Lattices in Bose-Einstein Condensates

J. R. Abo-Shaeer, C. Raman, J. M. Vogels, W. Ketterle

Quantized vortices play a key role in superfluidity and superconductivity. We have observed the formation of highly ordered vortex lattices in a rotating Bose-condensed gas. These triangular lattices contained over 100 vortices with lifetimes of several seconds. Individual vortices persisted up to 40 seconds. The lattices could be generated over a wide range of rotation frequencies and trap geometries, shedding light on the formation process. Our observation of dislocations, irregular structure, and dynamics indicates that gaseous Bose-Einstein condensates may be a model system for the study of vortex matter.

The quantization of circulation has a profound effect on the behavior of macroscopic quantum systems. Magnetic fields can penetrate type-II superconductors only as quantized flux lines. Vorticity can enter rotating superfluids only in the form of discrete line defects with quantized circulation. These phenomena are direct consequences of the existence of a macroscopic wavefunction, the phase of which must change by integer multiples of 2π around magnetic flux or vortex lines. In superconductors, magnetic flux lines arrange themselves in regular lattices that have been directly imaged (*1*). In superfluids, direct observation of vortices has been limited to small arrays (up to 11 vortices), both in liquid ^{4}He (*2*) and, more recently, in rotating gaseous Bose-Einstein condensates (BECs) (*3*, *4*).

We report the observation of vortex lattices in a BEC. We are now able to explore the properties of bulk vortex matter, which includes local structure, defects, and long-range order. In contrast, the properties of small arrays are strongly affected by surface and finite size effects. The vortex lattices are highly excited collective states of BECs with an angular momentum of up to 60 $\hbar$ per particle. Our experiments show that such states can be prepared and are much more stable than predicted (*5*).

Vortices in BECs have been the subject of extensive theoretical study (*6*). Experimental progress began only recently with the observation of quantized circulation in a two-component condensate by a phase engineering technique (*7*) and of vortex arrays in a single-component BEC (*3*). A condensate can be subjected to a rotating perturbation by revolving laser beams around it. This technique was used to study surface waves in a trapped BEC (*8*), and subsequently for the creation of vortices (*3*). In 1997, we tried unsuccessfully to detect quantized circulation as a "centrifugal hole" in ballistic expansion of the gas (*9*, *10*). Theoretical calculations (*11*–*13*) and ultimately the pioneering experimental work (*3*) showed that vortices can indeed be detected through ballistic expansion, which magnifies the spatial structure of the trapped condensate.

BECs of up to 5×10^7 Na atoms with a negligible thermal component (condensate fraction $\geq$ 90%) were produced by a combination of laser and evaporative cooling techniques (*8*, *10*, *14*). A radio-frequency "shield" limited the magnetic trap depth to 50 kHz (2.3 μK), preventing high-energy atoms from heating the condensate. Experiments were performed in cylindrical traps with widely varying aspect ratios. Most of the results and all of the images were obtained in a weak trap, with radial and axial frequencies of $\nu_r = 84$ Hz and $\nu_z = 20$ Hz (aspect ratio 4.2), respectively. In this weak trap inelastic losses were suppressed, resulting in larger condensates of typically 5×10^7 atoms. Such clouds had a chemical potential (μ) of 310 nK (determined from time-of-flight imaging), a peak density of 4.3×10^{14} cm^{-3}, a Thomas-Fermi radius along the radial direction (R_r) of 29 μm, and a healing length (ξ) of about 0.2 μm.

Vortex lattices were produced by rotating the condensate around its long axis with the optical dipole force exerted by blue-detuned laser beams at a wavelength of 532 nm. A two-axis acousto-optic deflector generated a pattern of two laser beams rotating symmetrically around the condensate at variable drive frequency Ω (*8*). The two beams were separated by one Gaussian beam waist (w = 25 μm). The laser power of 0.7 mW in each beam corresponded to an optical dipole potential of 115 nK. This yielded a strong, anharmonic deformation of the condensate.

After the condensate was produced, the stirring beam power was ramped up over 20 ms, held constant for a variable stirring time, and then ramped down to zero over 20 ms. The condensate equilibrated in the magnetic trap for a variable hold time (typically 500 ms). The trap was then suddenly switched off, and the gas expanded for 35 ms to radial and axial sizes of $l_r \cong 1000$ μm and $l_z \cong 600$ μm, respectively. We probed the vortex cores using resonant absorption imaging. To avoid blurring of the images due to bending of the cores near the edges of the condensate, we pumped a thin, 50- to 100-μm slice of atoms in the center of the cloud from the $F = 1$ to the $F = 2$ hyperfine state (*15*). This section was then imaged along the axis of rotation with a probe pulse resonant with the cycling $F = 2 \rightarrow 3$ transition. The duration of the pump and probe pulses was chosen to be sufficiently short (50 and 5 μs, respectively) to avoid blurring due to the recoil-induced motion and free fall of the condensate.

We observed highly ordered triangular lattices of variable vortex density containing up to 130 vortices (Fig. 1). A striking feature is the extreme regularity of these lattices, free of any major distortions, even near the boundary. Such "Abrikosov" lattices were first predicted for quantized magnetic flux lines in type-II superconductors (*16*). Tkachenko showed that their lowest energy structure should be triangular for an infinite system (*17*). A slice through images shows the high visibility of the vortex cores (Fig. 2), which was as high as 80%. For a trapped condensate with maximum vortex density, we infer that the distance between the vortices was $\cong$ 5 μm. The radial size of the condensate in the time-of-flight images was over 10% larger when it was filled with the maximum number of vortices, probably due to centrifugal forces.

When a quantum fluid is rotated at a frequency Ω, it attempts to distribute the vorticity as uniformly as possible. This is similar to a rigid body, for which the vorticity

Department of Physics, Center for Ultracold Atoms at Massachusetts Institute of Technology (MIT) and Harvard University, and Research Laboratory of Electronics, MIT, Cambridge, MA 02139, USA.

*To whom correspondence should be addressed. E-mail: jamil@mit.edu

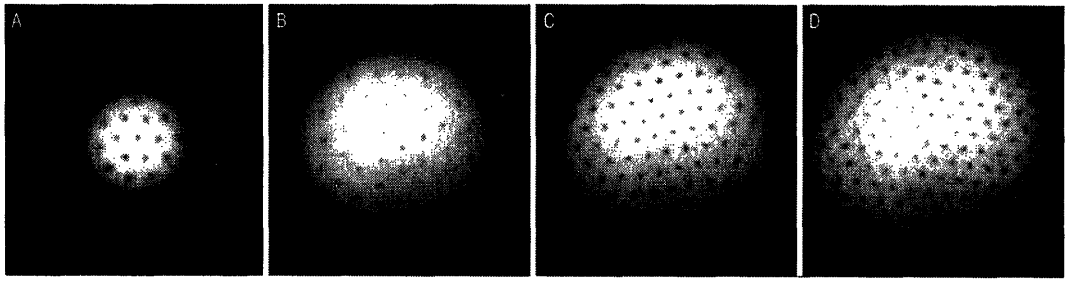

Fig. 1. Observation of vortex lattices. The examples shown contain approximately (**A**) 16, (**B**) 32, (**C**) 80, and (**D**) 130 vortices. The vortices have "crystallized" in a triangular pattern. The diameter of the cloud in (D) was 1 mm after ballistic expansion, which represents a magnification of 20. Slight asymmetries in the density distribution were due to absorption of the optical pumping light.

is constant $\nabla \times \vec{v} = 2\vec{\Omega}$. For a superfluid, the circulation of the velocity field, $\vec{v}$, is quantized in units of $\kappa = h/M$, where M is the atomic mass and h is Planck's constant. The quantized vortex lines are distributed in the fluid with a uniform area density (*18*)

$$n_v = 2\Omega/\kappa \quad (1)$$

In this way the quantum fluid achieves the same average vorticity as a rigidly rotating body, when "coarse-grained" over several vortex lines. For a uniform density of vortices, the angular momentum per particle is $N_v\hbar/2$, where N_v is the number of vortices in the system.

The number of observed vortices is plotted as a function of stirring frequency Ω for two different stirring times (Fig. 3). The peak near 60 Hz corresponds to the frequency $\Omega/2\pi = \nu_r/\sqrt{2}$, where the asymmetry in the trapping potential induced a quadrupolar surface excitation, with angular momentum $l = 2$, about the axial direction of the condensate (the actual excitation frequency of the surface mode $\nu = \sqrt{2}\nu_r$ is two times larger due to the twofold symmetry of the quadrupole pattern). The same resonant enhancement in the vortex production was observed for a stiff trap, with $\nu_r = 298$ Hz and $\nu_z = 26$ Hz (aspect ratio 11.5), and has recently been studied in great detail for small vortex arrays (*19*).

Far from the resonance, the number of vortices produced increased with the stirring time. By increasing the stir time up to 1 s, vortices were observed for frequencies as low as 23 Hz ($\cong 0.27\nu_r$). Similarly, in a stiff trap we observed vortices down to 85 Hz ($\cong 0.29\ \nu_r$). From Eq. 1 one can estimate the equilibrium number of vortices at a given rotation frequency to be $N_v = 2\pi R^2\Omega/\kappa$. The observed number was always smaller than this estimate, except near resonance. Therefore, the condensate did not receive sufficient angular momentum to reach the ground state in the rotating frame. In addition, because the drive increased the moment of inertia of the condensate (by weakening the trapping potential), we expect the lattice to rotate faster after the drive is turned off.

Looking at time evolution of a vortex lattice (Fig. 4), the condensate was driven near the quadrupole resonance for 400 ms and then probed after different periods of equilibration in the magnetic trap. A blurry structure was already visible at early times. Regions of low column density are probably vortex filaments that were misaligned with the axis of rotation and showed no ordering (Fig. 4A). As the dwell time increased, the filaments began to disentangle and align with the axis of the trap (Fig. 4, B and C), and finally formed a completely ordered Abrikosov lattice after 500 ms (Fig. 4D). Lattices with fewer vortices could be generated by rotating the condensate off resonance. In these cases, it took longer for regular lattices to form. Possible explanations for this observation are the weaker interaction between vortices at lower vortex density and the larger distance they must travel to reach their lattice sites. In principle, vortex lattices should have already formed in the rotating, anisotropic trap. We suspect that intensity fluctuations of the stirrer or improper beam alignment prevented this.

The vortex lattice had lifetimes of several seconds (Fig. 4, E to G). The observed stability of vortex arrays in such large condensates is surprising because in previous work the lifetime of vortices markedly decreased with the number of condensed atoms (*3*). Theoretical calculations predict a lifetime inversely proportional to the number of vortices (*5*). Assuming a temperature $k_BT \cong \mu$, where k_B is the Boltzmann constant, the predicted decay time of $\cong$ 100 ms is much shorter than observed. After 10 s, the number of vortices

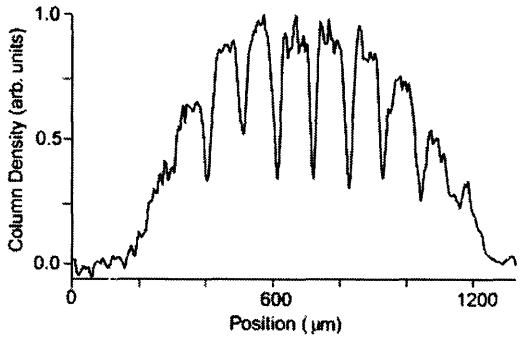

Fig. 2. Density profile through a vortex lattice. The curve represents a 5-μm-wide cut through a two-dimensional image similar to those in Fig. 1 and shows the high contrast in the observation of the vortex cores. The peak absorption in this image is 90%.

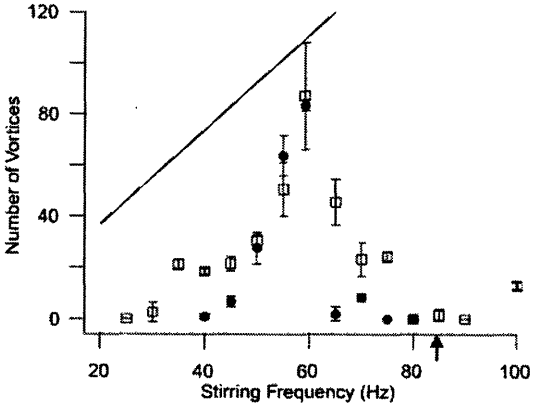

Fig. 3. Average number of vortices as a function of the stirring frequency Ω for two different stirring times, (●) 100 ms and (□) 500 ms. Each point represents the average of three measurements with the error bars given by the standard deviation. The solid line indicates the equilibrium number of vortices in a radially symmetric condensate of radius $R_r = 29$ μm, rotating at the stirring frequency. The arrow indicates the radial trapping frequency.

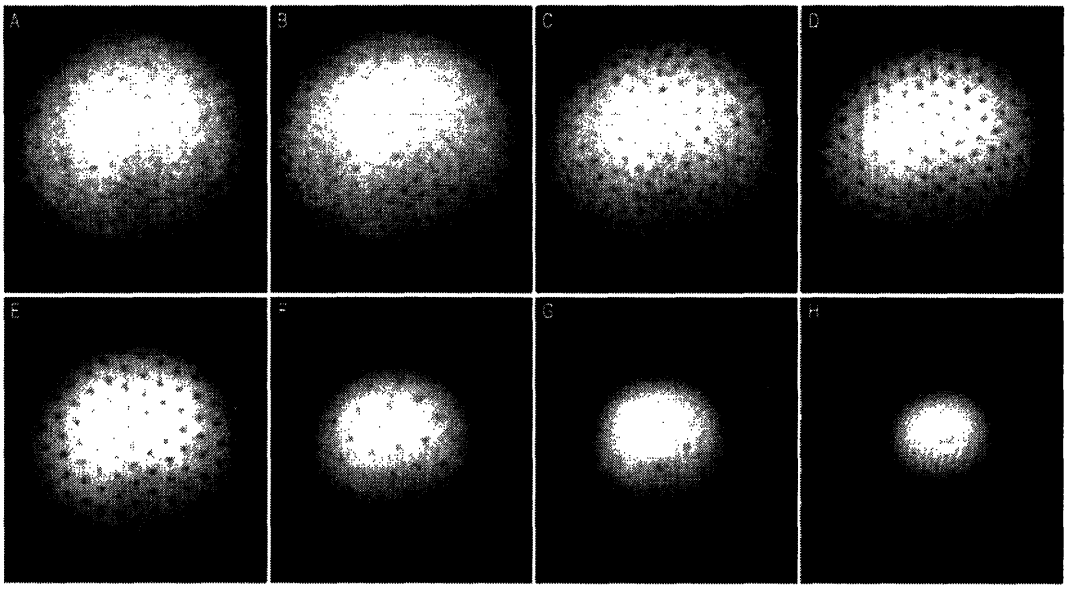

Fig. 4. Formation and decay of a vortex lattice. The condensate was rotated for 400 ms and then equilibrated in the stationary magnetic trap for various hold times. (A) 25 ms, (B) 100 ms, (C) 200 ms, (D) 500 ms, (E) 1 s, (F) 5 s, (G) 10 s, and (H) 40 s. The decreasing size of the cloud in (E) to (H) reflects a decrease in atom number due to inelastic collisions. The field of view is ~1 mm by 1.15 mm.

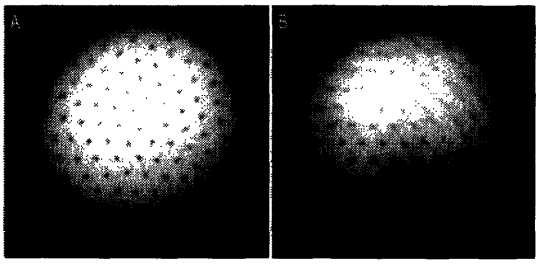

Fig. 5. Vortex lattices with defects. In (A), the lattice has a dislocation near the center of the condensate. In (B), there is a defect reminiscent of a grain boundary.

had diminished considerably. In several cases we observed a single vortex near the condensate center after 30 to 40 s (Fig. 4H). This dwell time is much longer than that observed for elongated clouds (1 to 2 s) (*3*) and for nearly spherical condensates (15 s) (*20*). We estimate that during its lifetime, the superfluid flow field near the central vortex core had completed more than 500,000 revolutions and the lattice itself had rotated ~100 times.

A feature of the lattices is their almost perfect triangular shape. Deformations are less pronounced than in theoretical calculations that predicted circular distortions (*13*, *21*). It was shown (*21*) that a configuration with perfect triangular symmetry can lower its energy by rearranging the outermost ring of vortices into a circle. This distortion is caused by the cylindrical symmetry of rotation and not by boundary effects (which were neglected in the calculations). In condensates of finite size and inhomogeneous density, one may expect even larger distortions. However, in images containing large numbers of vortices (Fig. 1, C and D), the lattice is triangular throughout the condensate even up to the edge. We have observed more complex lattice configurations in a fraction of the images. Some show patterns characteristic of partial crystallization (Fig. 4B), dislocations (Fig. 5A), and grain boundaries (Fig. 5B).

Our experiments may shed light on the ongoing discussion of vortex formation (*6*). A single vortex is expected to be thermodynamically stable when the rotation frequency exceeds (*22*)

$$\Omega_C = \frac{5}{2}\frac{\hbar}{MR_r^2}\ln\left[\frac{0.671R_r}{\zeta}\right] \qquad (2)$$

For our trap this yields a critical angular frequency of $\cong 2\pi \times 6$ Hz, or $0.08\omega_r$. Vortices were only observed at rotation frequencies much higher than Ω_C. Some have suggested that the critical frequency of $\cong 0.7\ \omega_r$ observed in other experiments was related to the suppression of unstable excitations (so-called anomalous modes) of rectilinear vortices (*6*, *23*, *24*). These anomalous modes depend strongly on the aspect ratio of the trap. Our observation of vortices at $\sim 0.25\omega_r$ in traps where the aspect ratio varied by a factor of 2.7 seems to rule out a crucial role of the anomalous modes, possibly because their frequencies are lower for dense condensates.

Apart from stability conditions, vortices must be nucleated. Several theoretical papers have discussed the barrier for the entry of a vortex from the edge (*6*, *25*, *26*). The condensate becomes unstable against surface deformations when the stirring frequency exceeds

$$\Omega_s = \min_l(\omega_l/l) \qquad (3)$$

where ω_l is the frequency of a surface excitation with angular momentum l in the axisymmetric trap (*27*, *28*). For our condensates, the instability is predicted to occur at $l \cong 18$, yielding $\Omega_s \cong 0.3\omega_r$, which is in fair agreement with our observations (*29*). The instabilities occur on a practical time scale only when the cloud is sufficiently deformed to excite high-l modes. In other experiments (*3*, *19*), a sizable deformation was achieved only by resonantly driving the $l = 2$ mode near $0.7\omega_r$. In contrast, we strongly deformed the condensate over a broad range of frequencies. For such deformations, l is no longer a good quantum number, allowing for coupling into higher-order modes. Our technique is therefore well suited to studying the threshold for vortex formation.

The surface instability criterion of Eq. 3 applies to rotational excitation. In the spirit of our earlier stirring experiments on critical velocities (*14*, *30*), we also explored linear motion of the stirrer. When we moved a small laser beam ($\cong$10 μm in diameter) at a velocity of 2 mm/s once through the condensate along the radial direction, we observed large lattices containing $\cong$ 50 vortices after an equilibration time of 1 s, indistinguishable from those generated with the rotating anisotropy. We assume that imperfect alignment of the stirring beam imparted a torque on the condensate. However, the mechanism of vortex formation warrants further study.

Properties of vortex lattices are of broad interest in superfluids, superconductors, and even astrophysics. Fluctuations in the rotation rate of pulsars are attributed to the dynamics of the vortex lattice in a superfluid neutron liquid (*5*, *31*). Our experiments show that vortex formation and self-assembly into a regular lattice is a robust feature of rotating BECs. Gaseous condensates may serve as a model system to study the dynamics of vortex matter, in analogy to work in type-II superconductors (*32*). Of particular interest are collective modes of the lattice. In liquid helium, transverse oscillations in a vortex lattice (Tkachenko oscillations) have already been investigated (*33*, *34*). Further studies may address the nucleation, ordering, and decay of lattices, in particular to delineate the role of the thermal component (*5*), and possible phase transition associated with melting and crystallization.

References and Notes

1. H. Träuble, U. Essmann, *Phys. Lett.* **24A**, 526 (1967).
2. E. J. Yarmchuk, M. J. V. Gordon, R. E. Packard, *Phys. Rev. Lett.* **43**, 214 (1979).
3. K. W. Madison, F. Chevy, W. Wohlleben, J. Dalibard, *Phys. Rev. Lett.* **84**, 806 (2000).
4. ———, *J. Mod. Opt.* **47**, 2715 (2000).
5. P. O. Fedichev, A. E. Muryshev, preprint available at http://arXiv.org/abs/cond-mat/0004264.
6. Reviewed in A. L. Fetter, A. A. Svidzinsky, *J. Phys. Condens. Matter* **13**, R135 (2001).
7. M. R. Matthews *et al.*, *Phys. Rev. Lett* **83**, 2498 (1999).
8. R. Onofrio *et al.*, *Phys. Rev. Lett.* **84**, 810 (2000).
9. M. R. Andrews, thesis, Massachusetts Institute of Technology (1998).
10. Reviewed in W. Ketterle, D. S. Durfee, D. M. Stamper-Kurn, in *Bose-Einstein Condensation in Atomic Gases, Proceedings of the International School of Physics Enrico Fermi, Course CXL*, M. Inguscio, S. Stringari, C. Wieman, Eds. (International Organisations Services B.V, Amsterdam, 1999), pp. 67–176.
11. E. Lundh, C. J. Pethick, H. Smith, *Phys. Rev. A* **58**, 4816 (1998).
12. F. Dalfovo, M. Modugno, *Phys. Rev. A* **61**, 023605 (2000).
13. Y. Castin, R. Dum, *Eur. Phys. J. D* **7**, 399 (1999).
14. R. Onofrio *et al.*, *Phys. Rev. Lett.* **85**, 2228 (2000).
15. M. R. Andrews *et al.*, *Science* **275**, 637 (1997).
16. A. A. Abrikosov, *J. Exp. Theor. Phys.* **5**, 1174 (1957) [*Zh. Eksp. Teor. Fiz.* **32**, 1442 (1957)].
17. V. K. Tkachenko, *J. Exp. Theor. Phys.* **22**, 1282 (1966) [*Zh. Eksp. Teor. Fiz.* **49**, 1875 (1965)].
18. P. Nozières, D. Pines, *The Theory of Quantum Liquids* (Addison-Wesley, Redwood City, CA, 1990).
19. K. W. Madison, F. Chevy, V. Bretin, J. Dalibard, preprint available at http://arXiv.org/abs/cond-mat/?0101051.
20. P. C. Haljan, B. P. Anderson, I. Coddington, E. A. Cornell, preprint available at http://arXiv.org/abs/cond-mat/0012320.
21. L. J. Campbell, R. M. Ziff, *Phys. Rev. B* **20**, 1886 (1979).
22. E. Lundh, C. J. Pethick, H. Smith, *Phys. Rev. A* **55**, 2126 (1997).
23. D. L. Feder, A. A. Svidzinsky, A. L. Fetter, C. W. Clark, *Phys. Rev. Lett.* **86**, 564 (2001).
24. J. J. García-Ripoll, V. M. Pérez-García, preprint available at http://arXiv.org/abs/cond-mat/0012071; ———, preprint available at http://arXiv.org/abs/con-mat/0101219.
25. T. Isoshima, K. Machida, *Phys. Rev. A* **60**, 3313 (1999).
26. A. A. Svidzinsky, A. L. Fetter, *Phys. Rev. Lett.* **84**, 5919 (2000).
27. F. Dalfovo, S. Giorgini, M. Guilleumas, L. P. Pitaevskii, S. Stringari, *Phys. Rev. A* **56**, 3840 (1997).
28. F. Dalfovo, S. Stringari, *Phys. Rev. A* **63**, 011601 (2001).
29. J. R. Anglin, personal communication.
30. C. Raman *et al.*, *Phys. Rev. Lett.* **83**, 2502 (1999).
31. R. J. Donnelly, *Quantized Vortices in Helium II* (Cambridge Univ. Press, Cambridge, 1991).
32. G. Blatter, M. V. Feigel'man, V. B. Geshkenbein, A. I. Larkin, V. M. Vinokur, *Rev. Mod. Phys.* **66**, 1125 (1994).
33. V. K. Tkachenko, *J. Exp. Theor. Phys.* **23**, 1049 (1966) [*Zh. Eksp. Teor. Fiz.* **50**, 1573 (1966)].
34. S. J. Tsakadze, *Fiz. Nizk. Temp.* **4**, 148 (1978) [*Sov. J. Low Temp. Phys.* **4**, 72 (1978)].

35. We thank J. R. Anglin, A. Görlitz, R. Onofrio, and L. Levitov for useful discussions and critical readings of the manuscript and T. Rosenband for assistance with the two-axis deflector. Supported by NSF, Office of Naval Research, Army Research Office, NASA, and the David and Lucile Packard Foundation.

26 February 2001; accepted 14 March 2001
Published online 22 March 2001;
10.1126/science.1060182
Include this information when citing this paper.

Self-Assembly of Subnanometer-Diameter Single-Wall MoS_2 Nanotubes

Maja Remskar,[1]* Ales Mrzel,[1] Zora Skraba,[1] Adolf Jesih,[1] Miran Ceh,[1] Jure Demšar,[1] Pierre Stadelmann,[2] Francis Lévy,[3] Dragan Mihailovic[1]

We report on the synthesis, structure, and self-assembly of single-wall subnanometer-diameter molybdenum disulfide tubes. The nanotubes are up to hundreds of micrometers long and display diverse self-assembly properties on different length scales, ranging from twisted bundles to regularly shaped "furry" forms. The bundles, which contain interstitial iodine, can be readily disassembled into individual molybdenum disulfide nanotubes. The synthesis was performed using a novel type of catalyzed transport reaction including C_{60} as a growth promoter.

The discovery of free-standing microscopic one-dimensional molecular structures, such as nanotubes of carbon, has attracted a great deal of attention in the last decade because of various interesting properties associated with their small dimensions, high anisotropy, and intriguing tube-like structures. These range from a variety of quantum effects (*1*, *2*) to potentially useful properties such as efficient field emission (*3*) and exceptional mechanical strength (*4*). Finding that curled-up dichalcogenide sheets can also form tube-like objects and fullerene-like nanoparticles (*5*–*8*) suggested that synthesis of nanotubes made of atoms other than carbon may be possible, and relatively small, 15-nm-diameter tubes made of tungsten and molybdenum disulfide have since been reported (*9*–*11*). The ultralow friction and wear properties of MoS_2 fullerene-like particles (*12*, *13*) make inorganic fullerenes important tribological materials. Other layered materials synthesized as nanotubes, tube-like forms, or onion-like structures have been reported, such as boron nitride nanotubes with diameters of a few nanometers (*14*, *15*), $W_{18}O_{49}$ hollow microfibers (*16*), and $NiCl_2$ multiwall nanotubes (*17*). Other layered compounds, such as NbS_2 (*18*) and GaSe (*19*), have been the subject of extensive theoretical calculations, which have predicted conditions for their stability in cylindrical form and some interesting electronic properties.

We report on the synthesis and basic structural properties of subnanometer-diameter monomolecular MoS_2 single-wall nanotubes (SWNTs) produced by a catalyzed transport reaction involving C_{60}, and show that the MoS_2 nanotubes grow in twisted chiral bundles of identically structured molecules stuck together with interstitial iodine. The tubes vary only in length, but not in diameter.

The single-wall MoS_2 nanotubes were grown by a catalyzed transport method using C_{60} as a growth promoter in the reaction. The C_{60} (5 weight %) was added to MoS_2 powder in the transport tube as catalyst, and the reaction was run typically for 22 days at 1010 K in an evacuated silica ampoule at a pressure of 10^{-3} Pa with a temperature gradient of 6 K/cm. Iodine was used as a transport agent. Approximately 15% (by weight) of the starting material was transported by the reaction to form SWNTs, with the rest remaining in the form of layered material. The transported material was subsequently thoroughly washed with toluene to remove the C_{60}.

The transported material grows in the form of bundles oriented perpendicular to the sub-

[1]Jozef Stefan Institute, Jamova 39, SI-1000 Ljubljana, Slovenia. [2]Centre de Microscopie Électronique-CIME, Ecole Polytechnique Fédérale de Lausanne, CH-1015 Lausanne, Switzerland. [3]Institute of Applied Physics, Ecole Polytechnique Fédérale de Lausanne, CH-1015 Lausanne, Switzerland.

*To whom correspondence should be addressed. E-mail: maja.remskar@ijs.si

Appendix B

Vortex Nucleation in a Stirred Bose-Einstein Condensate

C. Raman, J.R. Abo-Shaeer, J.M. Vogels, K.Xu, and W. Ketterle

"Vortex Nucleation in a Stirred Bose-Einstein Condensate,"

Phys. Rev. Lett. 87 210402 (2001).

Vortex Nucleation in a Stirred Bose-Einstein Condensate

C. Raman,* J.R. Abo-Shaeer, J.M. Vogels, K. Xu, and W. Ketterle

Department of Physics, MIT–Harvard Center for Ultracold Atoms, and Research Laboratory of Electronics, MIT, Cambridge, Massachusetts 02139

(Received 12 June 2001; published 1 November 2001)

We studied the nucleation of vortices in a Bose-Einstein condensate stirred by a laser beam. The vortex cores were observed using time-of-flight absorption imaging. Depending on the stirrer size, either discrete resonances or a broad response was visible as the stir frequency was varied. Stirring beams small compared to the condensate size generated vortices below the critical rotation frequency for the nucleation of surface modes, suggesting a local mechanism of generation. In addition, we observed the centrifugal distortion of the condensate due to the rotating vortex lattice and found evidence for bent vortices.

DOI: 10.1103/PhysRevLett.87.210402 PACS numbers: 03.75.Fi, 32.80.Pj, 67.40.Vs

Dissipation and turbulence in superfluid flow often involve the creation and subsequent motion of quantized vortices [1]. Since vortices are topological defects they may be created only in pairs or can enter a system individually from its boundary. The nucleation process has been the subject of much theoretical interest [2]. Experiments with Bose-Einstein condensates (BEC) confined in atom traps are well suited to test theories of nucleation because the boundary of the condensate is well controlled, and vortices can be directly imaged.

Vortex nucleation usually involves dynamical instabilities and superfluid turbulence [1,2]. Exceptions are the direct coupling between ground and vortex states for small condensates [3] and the engineering of states of quantized circulation by manipulating the phase of the wave function [4–6]. Turbulent flow can be created by perturbing the system with a time-dependent boundary, for example, by a small laser beam [7,8] or by a rotating trap anisotropy [9–11]. The resulting vortices have been directly imaged [8–10].

In a rotating frame, vortices are energetically favored above a critical rotational frequency Ω_c [2,12]. Current theories suggest that vortices must be nucleated by surface waves which "collapse" into a vortex state [13–17]. This corresponds to the disappearance of the energy barrier for a vortex to enter the cloud [2,14,18]. For surface excitations with angular momentum $l\hbar$ and frequency ω_l, the minimum rotational frequency is

$$\Omega_s = \min_l(\omega_l/l). \quad (1)$$

This corresponds to a Landau critical velocity for surface waves $v_c = \Omega_s R_{\mathrm{TF}}$, where R_{TF} is the Thomas-Fermi radius [15].

Recent experiments [9,19] observed vortices only at much *higher* frequencies, giving rise to a variety of theoretical models [17,20]. One explanation is that those experiments excited only the $l = 2$ mode, requiring a higher drive frequency than Eq. (1) [16,19,21,22]. We tested this prediction by stirring the condensate with anisotropies of different symmetries ($l = 2, 3, 4$) and observing distinct resonance frequencies for vortex formation.

Our central observation is that a small, localized stirring beam can generate vortices *below* Ω_s. This indicates that the current surface mode analysis of vortex nucleation is incomplete. One might expect such a stirrer to couple to many modes l. Surprisingly, the small beam did not excite resonances but could generate vortices as effectively as a resonant drive.

Our method of vortex generation has been outlined in previous work [10]. We start with nearly pure BECs (>90% condensate fraction) of up to 5×10^7 sodium atoms in a cylindrically shaped Ioffe-Pritchard magnetic trap with a mean radial frequency of $\omega_r = 2\pi \times 86$ Hz and axial frequency $\omega_z = 2\pi \times 20$ Hz. A radio frequency "shield" limited the magnetic trap depth to 50 kHz (2.3 μK). The condensate chemical potential, peak density, and healing length ξ were 300 nK, 4×10^{14} cm^{-3}, and 0.2 μm, respectively.

Vortices were generated by rotating the condensate about its long axis with a scanning blue-detuned laser beam (532 nm) whose beam waist varied between 5 and 25 μm [23]. For the tightest focus, the peak optical dipole potential was 620 nK. We used multiple beam patterns (formed by rapidly scanning the laser beam from 1.5 to 10 kHz) with scan radii as large as the Thomas-Fermi radius R_{TF}, which varied from 27–30 μm. The laser beam was left on during evaporation to damp out dipole motion. Immediately after producing a condensate we began the rotation for times of up to 500 ms, generating a vortex tangle. The laser beams were then instantly shut off and the cloud equilibrated for 500 ms, during which time the vortices crystallized into an Abrikosov lattice as shown in Fig. 4c and detailed in previous work [10]. For small numbers of vortices the gas did not fully settle into a regular lattice before imaging.

The vortex cores were observed using resonant absorption imaging after 41 ms of ballistic expansion, which magnified them by 20 from their size ξ in the trap. As in our previous work we imaged a 50–150 μm

slice of atoms in the center of the cloud using spatially selective optical pumping on the $F = 2$ to $F = 3$ cycling transition [10].

By varying the stirring parameters we explored different mechanisms for vortex nucleation. A large stirrer, with a beam waist comparable to the Thomas-Fermi radius showed enhanced vortex generation at discrete frequencies. Figure 1 shows the number of vortices versus the stirring frequency of the laser beam using 2-, 3-, and 4-point patterns. The total laser beam power corresponded to an optical dipole potential between 60 and 240 nK. The resonances were close to the frequencies of excitation of $l = 2$, 3, and 4 surface modes ($\omega_l/l = \omega_r/\sqrt{l}$) [13]. A second, higher resonance appeared in the 3- and 4-point data. This could be due to additional coupling to the quadrupole ($l = 2$) mode caused by misalignment of the laser beams [22]. The extra peaks and the shift of the resonances from the frequencies ω_l/l may be due to the presence of vortices and the stirrer, both of which make an unperturbed surface mode analysis inadequate.

Our results clearly show discrete resonances in the nucleation rate of vortices that depend on the geometry of the rotating perturbation. This confirms the role of discrete surface modes in vortex formation. A dependence on the symmetry of the stirrer (1-point versus 2-point) has also been explored in Paris [22]. For longer stirring times and higher laser powers the condensate accommodated more vortices at all frequencies, and the resonances became less pronounced.

A stirrer much smaller than the condensate size could generate vortices very rapidly—more than 100 vortices were created in 100 ms of rotation. Figure 2a shows the number of vortices produced using a 2-point pattern with a scan radius close to R_{TF} for various stirring times. Above

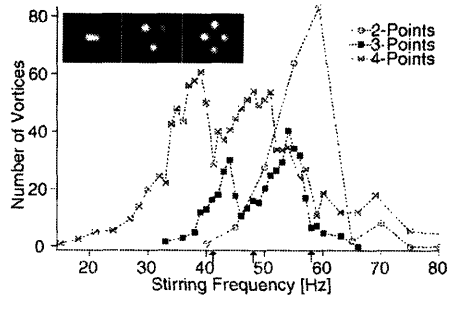

FIG. 1. Discrete resonances in vortex nucleation. The number of vortices created by multipoint patterns is shown. The condensate radius was $R_{TF} = 28$ μm. Each data point is the average of three measurements. The arrows below the graph show the positions of the surface mode resonances $\omega_r/\sqrt{l}$. The stirring times were 100 ms for the 2- and 3-point data, and 300 ms for the 4-point data. The inset shows 2-, 3-, and 4-point dipole potentials produced by a 25 μm waist laser beam imaged onto the charge-coupled device camera. The separation of the beams from the center is 25 μm for the 2-point pattern and 55 μm for the 3- and 4-point patterns. The laser power per spot was 0.35, 0.18, and 0.15 mW for the 2-, 3-, and 4-point data, respectively.

300 ms the angular momentum of the cloud appeared to saturate and even decreased, accompanied by visible heating of the cloud.

The maximum number of vortices was roughly proportional to the stirring frequency. For a lattice rotating at frequency Ω, the quantized vortex lines are distributed with a uniform area density $n_v = 2\Omega/\kappa$, where $\kappa = h/M$ is the quantum of circulation and M is the atomic mass [12]. Therefore, the number of vortices at a given rotation frequency should be

$$N_v = 2\pi R^2 \Omega/\kappa \quad (2)$$

in a condensate of radius R. The straight line in Fig. 2a assumes $R = R_{TF}$ and that the lattice has equilibrated with the drive. In contrast to the large stirrer no resonances were visible even when the number of vortices had not yet saturated. This suggests a different mechanism of vortex nucleation for which further evidence was obtained from the frequency and spatial dependences.

For our experimental conditions, a numerical calculation by Feder yields $\Omega_s \simeq 0.25\omega_r = 21$ Hz [24]. With the small stirrer, we observed vortices at frequencies as low as 7 Hz. Below this frequency the velocity of the stirrer was not much larger than the residual dipole oscillation of the condensate. The rotational frequency below which a

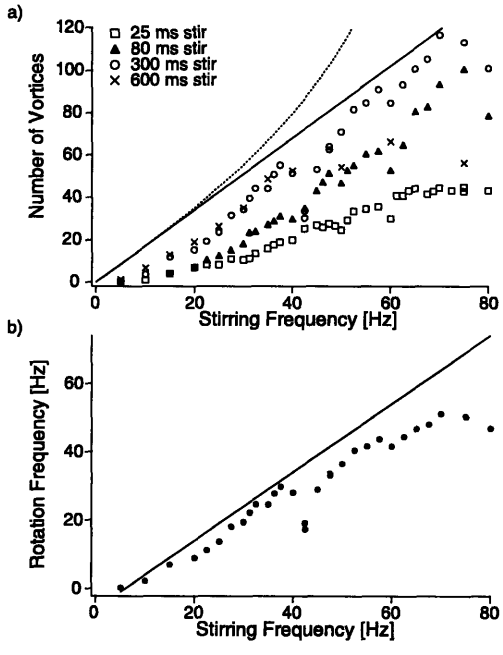

FIG. 2. Nonresonant nucleation using a small stirrer. (a) Average number of vortices created using a 2-point pattern positioned at the edge of the condensate. The beam waist, total power, and separation were 5.3 μm, 0.16 mW, and 54 μm, respectively. (b) Effective lattice rotation frequency. The lines in both graphs indicate the predictions of different models described in the text. The fewer vortices observed near half the trapping frequency (42 Hz) are probably due to parametric heating.

rectilinear vortex in the condensate center is energetically favored is 7 Hz [2].

In Fig. 3 we varied the radius of the 2-point scan. The stirring frequency was chosen to keep the linear velocity of the laser beam constant. Vortices could be generated over a broad range of radii. The maximum number was obtained at intermediate radii rather than the Thomas-Fermi surface, providing further evidence that surface excitations of the unperturbed condensate are not the dominant nucleation mechanism. The observed radial dependence makes it unlikely that the thermal cloud plays a crucial role in the vortex nucleation, since at very low temperatures its maximum density occurs at the surface of the condensate. Indeed, we observed fewer vortices at higher temperatures.

The nucleation mechanism for small stirrers may be related to our earlier experiments on the onset of dissipation in stirred condensates. There we observed a drag force at velocities above $\sim 0.1c$, where c is the speed of sound at the condensate center [7,25]. The friction with the moving stirrer causes an asymmetry in the density profile in front of and behind the laser beam. This has been directly imaged for linear motion [25]. Similar flow field effects can be observed in Fig. 3b, where they are clearly linked to the formation of vortices. Vortex pairs are predicted to arise from linear stirring [26,27]. When the laser beam moves in a circle, corotating vortices will be favored, whereas counterrotating vortices will be expelled from the system.

For an object smaller than the healing length ξ, the critical velocity for vortex formation occurs at the Landau value given by Eq. (1). For larger objects such as our laser beam, the flow field around the stirrer can reduce the critical velocity relative to Eq. (1) [26], which may explain our observation of vortices below 21 Hz.

In our earlier work we observed that the size of a condensate with vortices exceeded the size of the nonrotating condensate [10]. Here we study these centrifugal distortions quantitatively (also note [11]). Figure 4 shows the enhancement of the cloud size R in time of flight by up to 25% due to additional rotational kinetic energy. Rotation adds a centrifugal potential $-(1/2)M(\Omega r)^2$, leading to an effective radial trapping frequency of $\sqrt{\omega_r^2 - \Omega^2}$. For a constant number of atoms N, this increases the Thomas-Fermi radius

$$R_{\mathrm{TF}} = R_0/[1 - (\Omega/\omega_r)^2]^{3/10} \qquad (3)$$

and reduces the mean-field interaction energy E_{int}. The total release energy of the gas is then $E = E_{\mathrm{int}} + \frac{1}{2} I_{\mathrm{eff}} \Omega^2 + E_{v0} N_v$. The second term accounts for the rigid rotation of the lattice while the third term is a quantum correction due to the kinetic energy of the cores, which is negligible for large N_v. The effective moment of inertia of the condensate is $I_{\mathrm{eff}} = 2/7 M R_{\mathrm{TF}}^2 N$. The energy per unit length of a single vortex E_{v0} must be averaged over the Thomas-Fermi distribution [28]. We predict a 30% increase in E for 120 vortices, whereas the observed increase in R^2 is about 50%. This discrepancy is probably due to our selection of the central slice of the cigar, where the rotational energy is the highest, and due

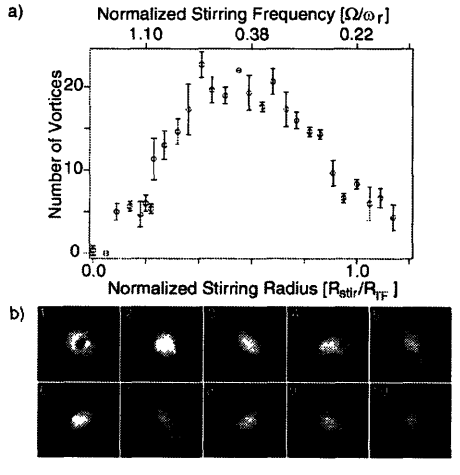

FIG. 3. Spatial dependence of vortex nucleation. (a) The number of vortices produced at a constant stirring velocity ($0.2c$). At the Thomas-Fermi radius, the angular frequency of the stirrer was 17.5 Hz. The error bars are the standard deviation of three measurements at the same radius. (b) Axial phase contrast images showing the pure condensate with the aligned stirrer (1), and at 4.4 ms intervals, the condensate during (2–7) and after (8–10) stirring. Each frame is 120 μm wide.

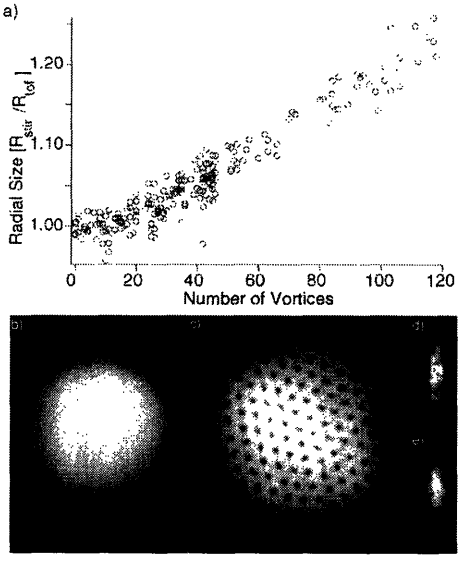

FIG. 4. Centrifugal effects on a rotating condensate. (a) Observed radial size of the condensate, as determined from a parabolic fit to the time-of-flight distribution after 41.5 ms. (b),(c) Comparison of a nonrotating condensate ($R_{\mathrm{tof}} = 570$ μm) and one with 160 vortices. Radial *in situ* phase contrast imaging of (d) a condensate at rest, and (e) in rotation at a frequency of 75 Hz, showing the modified aspect ratio. The length of the condensate in (d) was 200 μm.

to the unobserved axial expansion, which may depend on the angular momentum of the cloud.

If we account for centrifugal effects and combine Eqs. (2) and (3), we expect a divergence of the number of vortices near the trap frequency (dashed line in Fig. 2a). The deviation of the data from this line suggests that the condensate did not fully equilibrate with the rotating drive. Taking into account the critical velocity for vortex nucleation, $v_c \simeq 0.1c$ [25], we expect the maximum rotation frequency of the lattice to be $\Omega_S - v_c/R_{\mathrm{TF}}$, where Ω_S is the frequency of the stirrer moving at radius R_{TF}. Using the measured number of vortices, we can invert Eqs. (2) and (3) to derive the lattice rotation frequency, which is shown in Fig. 2b, along with the expected value $\Omega_S - 2\pi \times 6$ Hz assuming a constant N. The discrepancy can be partly attributed to loss of atom number due to heating by the stirrer, which was up to 30%. We can also derive from these equations the flow velocity at the edge of the condensate. For a lattice with 144 vortices, this velocity exceeded the speed of sound at the condensate center by 40%, in contrast to a recent suggestion that supersonic rotation speeds are unattainable [29].

At low rotational velocities, vortices should not be rectilinear as assumed in many theoretical calculations but bent [30,31]. Such bent vortices should have lower visibility in our images due to the line of sight integration across the optically pumped condensate slice. Figure 5 shows several examples. Some appear as vortex lattices with tilted vortex cores. Other images show structures reminiscent of half rings and coiled vortices. However, it is not obvious how some of the observed time-of-flight features are related to spatial structures in the trapped condensate.

In conclusion, we have identified two distinct mechanisms for vortex nucleation in rotating condensates—surface modes and local turbulence. It would be intriguing to study the vortex phase diagram [32,33] and the role of the thermal cloud in vortex decay [29].

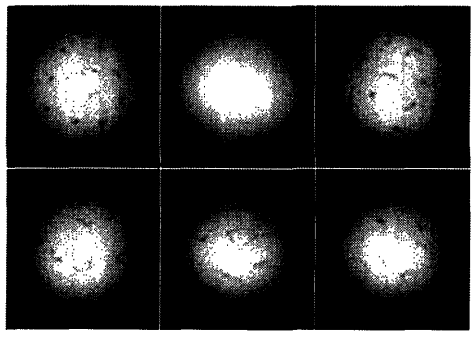

FIG. 5. Three-dimensional structure of vortices. Shown are several examples of time-of-flight pictures of condensates at low rotational frequencies, where "smeared-out" vortex cores and elongated features were observed. The condensate radius was 510 μm.

We thank J. R. Anglin, D. Feder, A. E. Leanhardt, and A. P. Chikkatur for useful discussions. This research is supported by NSF, ONR, ARO, NASA, and the David and Lucile Packard Foundation.

*Present address: School of Physics, Georgia Institute of Technology, Atlanta, GA 30332-0430.
Email address: craman@gatech.edu

[1] R. J. Donnelly, *Quantized Vortices in Helium II* (Cambridge University Press, Cambridge, 1991).
[2] A. L. Fetter and A. A. Svidzinsky, J. Phys. Condens. Matter **13**, R135 (2001).
[3] B. M. Caradoc-Davies, R. J. Ballagh, and K. Burnett, Phys. Rev. Lett. **83**, 895 (1999).
[4] M. R. Matthews *et al.*, Phys. Rev. Lett. **83**, 2498 (1999).
[5] Ł. Dobrek *et al.*, Phys. Rev. A **60**, R3381 (1999).
[6] K.-P. Marzlin and W. Zhang, Phys. Rev. A **57**, 4761 (1998).
[7] C. Raman *et al.*, Phys. Rev. Lett. **83**, 2502 (1999).
[8] S. Inouye *et al.*, e-print cond-mat/0104444.
[9] K. W. Madison *et al.*, Phys. Rev. Lett. **84**, 806 (2000).
[10] J. R. Abo-Shaeer, C. Raman, J. M. Vogels, and W. Ketterle, Science **292**, 476 (2001).
[11] P. Haljan *et al.*, e-print cond-mat/0106362.
[12] P. Nozières and D. Pines, *The Theory of Quantum Liquids* (Addison-Wesley, Redwood City, CA, 1990).
[13] F. Dalfovo *et al.*, Phys. Rev. A **56**, 3840 (1997).
[14] T. Isoshima and K. Machida, Phys. Rev. A **60**, 3313 (1999).
[15] U. A. Al Khawaja *et al.*, Phys. Rev. A **60**, 1507 (1999).
[16] F. Dalfovo and S. Stringari, Phys. Rev. A **63**, 011601 (2001); M. Tsubota *et al.*, e-print cond-mat/0104523.
[17] D. L. Feder *et al.*, Phys. Rev. Lett. **86**, 564 (2001).
[18] D. L. Feder *et al.*, Phys. Rev. A **61**, 011601(R) (2000).
[19] K. W. Madison *et al.*, Phys. Rev. Lett. **86**, 4443 (2001).
[20] J. J García-Ripoll and V. M. Pérez-García, e-print cond-mat/0006368.
[21] S. Sinha and Y. Castin, e-print cond-mat/0101292.
[22] F. Chevy *et al.*, e-print cond-mat/0104218.
[23] R. Onofrio *et al.*, Phys. Rev. Lett. **84**, 810 (2000).
[24] D. Feder (private communication).
[25] R. Onofrio *et al.*, Phys. Rev. Lett. **85**, 2228 (2000).
[26] T. Frisch *et al.*, Phys. Rev. Lett. **69**, 1644 (1992).
[27] B. Jackson *et al.*, Phys. Rev. Lett. **80**, 3903 (1998).
[28] D. Stauffer and A. Fetter, Phys. Rev. **168**, 156 (1968).
[29] P. O. Fedichev and A. E. Muryshev, e-print cond-mat/0004264.
[30] J. J. García-Ripoll and V. M. Pérez-García, e-print cond-mat/01021297.
[31] A. Aftalion and T. Riviere, e-print cond-mat/0105208.
[32] S. Stringari, Phys. Rev. Lett. **82**, 4371 (1999).
[33] T. Mizushima *et al.*, e-print cond-mat/0104358.

Appendix C

Formation and Decay of Vortex Lattices

J.R. Abo-Shaeer, C. Raman, and W. Ketterle

"Formation and Decay of Vortex Lattices in Bose-Einstein Condensates at Finite Temperatures,"

Phys. Rev. Lett. 91 070409 (2002).

(Included in Appendix C)

Formation and Decay of Vortex Lattices in Bose-Einstein Condensates at Finite Temperatures

J. R. Abo-Shaeer,* C. Raman,† and W. Ketterle

Department of Physics, MIT-Harvard Center for Ultracold Atoms, and Research Laboratory of Electronics, Massachusetts Institute of Technology, Cambridge, Massachusetts 02139

(Received 13 August 2001; published 1 February 2002)

The dynamics of vortex lattices in stirred Bose-Einstein condensates have been studied at finite temperatures. The decay of the vortex lattice was observed nondestructively by monitoring the centrifugal distortions of the rotating condensate. The formation of the vortex lattice could be deduced from the increasing contrast of the vortex cores observed in ballistic expansion. In contrast to the decay, the formation of the vortex lattice is insensitive to temperature change.

DOI: 10.1103/PhysRevLett.88.070409 PACS numbers: 03.75.Fi, 32.80.Pj, 67.40.Vs

Gaseous Bose-Einstein condensates (BEC) have become a test bed for many-body theory. The properties of a condensate at zero temperature are accurately described by a nonlinear Schrödinger equation. More recently, theoretical work on the ground state properties of condensates [1] has been extended to rotating condensates containing one or several vortices [2] and their dynamics. These include vortex nucleation [3,4], crystallization of the vortex lattice [5], and decay [6,7]. Experimental study has focused mainly on the nucleation of vortices, either by stirring condensates directly with a rotating anisotropy [8–10] or creating condensates out of a rotating thermal cloud [11]. In addition, the decay of vortices in nearly pure condensates has also been analyzed [8,11,12]. Here we report the first quantitative investigation of vortex dynamics at finite temperature. The crystallization and decay of a vortex lattice have been studied and a striking difference is found between the two processes: while the crystallization is essentially temperature independent, the decay rate increases dramatically with temperature.

The method used to generate vortices has been outlined in previous work [9,13]. Condensates of up to 75 million sodium atoms (>80% condensate fraction) were prepared in a cigar-shaped Ioffe-Pritchard magnetic trap using evaporative cooling. The radial and axial trap frequencies of $\omega_x = 2\pi \times (88.8 \pm 1.4)$ Hz, $\omega_y = 2\pi \times (83.3 \pm 0.8)$ Hz, and $\omega_z = 2\pi \times (21.1 \pm 0.5)$ Hz, corresponded to a radial trap asymmetry of $\epsilon_r = (\omega_x^2 - \omega_y^2)/(\omega_x^2 + \omega_y^2) = (6.4 \pm 0.2)\%$ and an aspect ratio of $A = \omega_x/\omega_z = (4.20 \pm 0.04)$. The relatively large value of the radial trap asymmetry is due to gravitational sag and the use of highly elongated pinch coils (both estimated to contribute equally). The radio frequency (rf) used for evaporation was held at its final value to keep the temperature of the condensate roughly constant throughout the experiment. The condensate's Thomas-Fermi radii, chemical potential, and peak density were $R_r = 28$ μm, $R_z = 115$ μm, 300 nK, and 4×10^{14} cm^{-3}, corresponding to a healing length $\xi \simeq 0.2$ μm.

Vortices were produced by spinning the condensate for 200 ms along its long axis with a scanning, blue-detuned laser beam (532 nm) [8,14]. For this experiment two symmetric stirring beams were used (Gaussian waist $w = 5.3$ μm, stirring radius 24 μm). The laser power of 0.16 mW per beam corresponded to an optical dipole potential of 310 nK. After the stirring beams were switched off, the rotating condensate was left to equilibrate in the static magnetic trap for various hold times. As in our previous work, the vortex cores were observed using optical pumping to the $F = 2$ state and resonant absorption imaging on the $F = 2$ to $F = 3$ cycling transition [9]. After 42.5 ms of ballistic expansion the cores were magnified to 20 times their size, ξ, in the trap.

The decay of the vortex lattice can be observed by allowing the condensate to spin down in the trap for variable times before the ballistic expansion and subsequent observation of the vortex cores. However, this method requires destructive imaging and suffers from shot-to-shot variations. *In situ* phase-contrast imaging is nondestructive, but the vortex cores are too small to be resolved. Instead, we monitored the centrifugal distortion of the cloud due to the presence of vorticity. This is a quantitative measure for the rotation frequency, Ω, of the lattice, and therefore the number of vortices [15]. Such distorted shapes have been observed previously for rotating clouds [9,11,13].

The shape of a rotating condensate is determined by the magnetic trapping potential and the centrifugal potential $-\frac{1}{2}M\Omega^2 r^2$, where M is the atomic mass. From the effective radial trapping frequency $\omega_r \rightarrow \omega_r' = \sqrt{\omega_r^2 - \Omega^2}$, one obtains the aspect ratio of the rotating cloud, $A' = \omega_r'/\omega_z$, as

$$A' = A\sqrt{1 - (\Omega/\omega_r)^2}. \quad (1)$$

For the decay measurements, the condensate was stirred for 200 ms, producing ~130 vortices on average at the coldest temperature (determined using time-of-flight imaging). After the drive was stopped the cloud equilibrated in the stationary magnetic trap. Ten *in situ* images of each condensate were taken at equal time intervals using nondestructive phase-contrast imaging detuned 1.7 GHz from resonance (see Fig. 1a). We verified that the decay rate was not affected due to repeated imaging by varying the

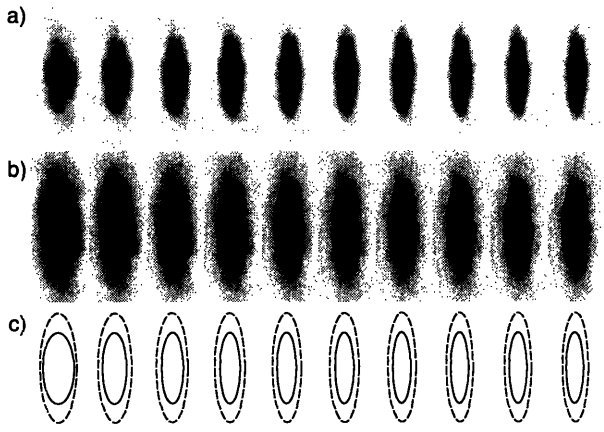

FIG. 1. (a) Spin down of a rotating condensate in a static magnetic trap. The first phase contrast image is taken 100 ms after turning off the drive, with each subsequent image spaced by 100 ms. The rotating vortex lattice caused a radial swelling of the condensate, reducing the aspect ratio. As vortices leave the system the aspect ratio approaches its static value of 4.2. The field of view is 25 by 75 μm. (b) Observation of a rotating thermal cloud. The parameters are identical to (a), but the probe light detuning is closer to resonance, enhancing the sensitivity to the more dilute thermal cloud. The phase shift of the dense condensate exceeds 2π and is displayed as saturated (black) in the image. The apparent loss in atom number is due to Rayleigh scattering of the probe light. (c) The inner and outer contours represent the aspect ratio of the condensate and thermal cloud, respectively, as obtained from two-dimensional fits to phase-contrast images.

time between exposures. The theoretical treatment of the decay has two limiting cases, one where the thermal cloud is nearly stationary and the other where the thermal cloud is closely following the rotating condensate [6]. Because the thermal cloud could not easily be discerned in images taken with 1.7 GHz detuning, we used light closer to resonance (400 MHz detuning) to determine the shape of the thermal cloud (Fig. 1b).

The aspect ratio of the condensate was obtained by fitting a 2D Thomas-Fermi profile to the 1.7 GHz images. The aspect ratio of the thermal cloud was determined from the 400 MHz images by masking off the condensate in the inner region of the cloud and then fitting a 2D Gaussian to the image. The comparison of the contours of the condensate and thermal cloud (condensate fraction of $N_c/N = 0.62$) shows that the thermal cloud is also rotating. The images for the thermal cloud show that the aspect ratio decays from 3.0 to 4.2 on the same time scale as the condensate. This corresponds to an initial rotation rate of $\sim 2/3$ that of the condensate.

The damping rate of the vortex lattice, obtained from exponential fits to the data, was studied at different temperatures by varying the condensed fraction of atoms in the trap. The condensate fractions were obtained from fits to time-of-flight images of the condensate *before* the stirring. The temperature was derived from these values using the scaling theory for an interacting Bose gas [16]. At a fixed rf frequency for evaporation, the centrifugal potential lowers the trap depth by a factor $1 - (\Omega/\omega_r)^2$ for a thermal cloud rotating at frequency Ω. Evaporation should lower the temperature of the rotating cloud by the same factor.

Figure 2a shows how the aspect ratio of the condensate approaches its static value as the vortex lattice decays. The decrease of the angular speed appears to be exponential (Fig. 2b) and strongly depends on temperature (Fig. 3). The crystallization of the lattice occurs during the first 500 ms of hold time. Examination of Fig. 2 during this time frame indicates that this process has no effect on the decay. It should be noted that the exponential nature of the decay is related to the corotation of the thermal cloud with the condensate. When the thermal cloud is fixed, theoretical [6] and experimental [8] studies show nonexponetial behavior.

In addition to the decay process, the formation of the vortex lattice has also been examined. After rotating the condensate it typically took hundreds of ms for the lattice to form (see Fig. 4 in Ref. [9]). One may expect the lattice to already form in the rotating frame during the stirring because the lattice is the lowest energy state for a given angular momentum. This absence of equilibration in the rotating frame is presumably due to heating and excitation

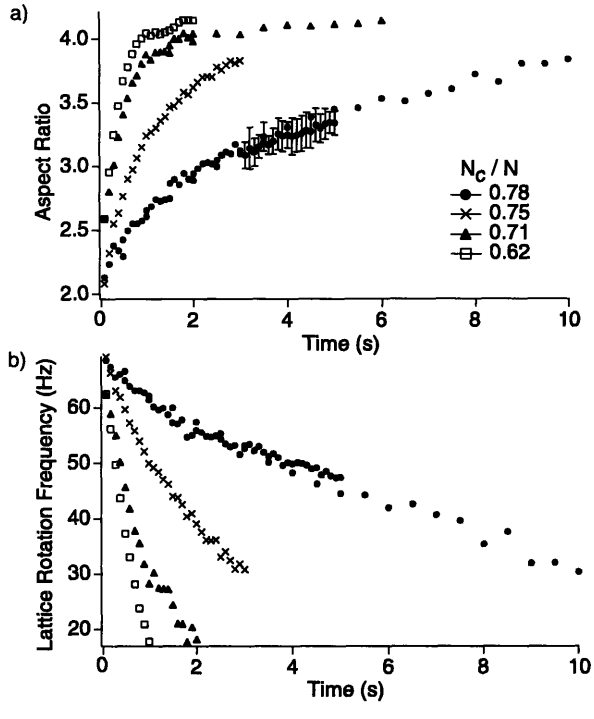

FIG. 2. Decay of a vortex lattice at finite temperatures. (a) The aspect ratio of the condensate approaching its static value. Each point represents the average of ten measurements. Error bars given for (•) are statistical and are typical of all four data sets. (b) The decay of the rotation rate of the lattice for the same data using Eq. (1). The decay of the rotation depends strongly on the thermal component.

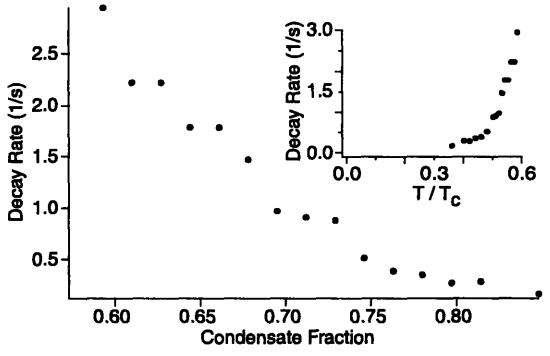

FIG. 3. Decay rates for vortex lattices at several temperatures. The rates are determined from data taken during the first second of equilibration. Each point represents the average of five measurements. The inset figure emphasizes the strong dependence of the decay rate on temperature, T. The transition temperature was $T_c = 790$ nK and varied by less than 7% for the data shown.

of collective lattice modes by the stirring beams. The crystallization of the vortex lattice was studied by determining the contrast or visibility of the vortex cores as a function of equilibration time. To avoid any bias, we used an automated vortex recognition algorithm. Each image was normalized by dividing it by a blurred duplicate of itself. A binary image was then created with a threshold set to the value at which the algorithm reliably detected almost all vortices that were identified by visual inspection of equilibrated images (there was less than 5% discrepancy). Clusters of contiguous bright pixels within a circular area were counted as "visible" vortices. Figure 4a shows three vortex lattices after different equilibration times with the visible vortices identified.

The lowest temperature (337 nK, corresponding to a condensate fraction of $\approx$80%) was close to the chemical potential. Further cooling would have resulted in smaller condensates. The highest temperature (442 nK) was limited by the rapid decay of the vortex lattice.

Figure 4b and 4c show that the formation of the lattice depends very weakly on temperature, if at all, over the range studied. The larger number of vortices crystallized at lower temperatures (Fig. 4b) is due to the strong temperature dependence of the lattice decay rates, which differed by more than a factor of 5. We can correct for this by estimating the number of vortices $N_v(t)$ as a function of time from the centrifugal distortion measurements described above as $N_v(t) = [2\Omega(t)/\kappa]\pi R(t)^2$, where $\kappa = h/M$ is the quantum of circulation, M is the sodium mass, and R is the radial Thomas-Fermi radius. By normalizing the number of visible vortices by this estimate, we deduce the vortex visibility as a function of time. These lattice formation curves overlap almost perfectly for different temperatures (Fig. 4c).

The decay of a vortex lattice is discussed in Refs. [6,7]. The process is modeled as a two-step transfer of angular momentum. The rotation of the condensate is damped due to friction with the thermal cloud ($\mu_{c-\mathrm{th}}$), which is in

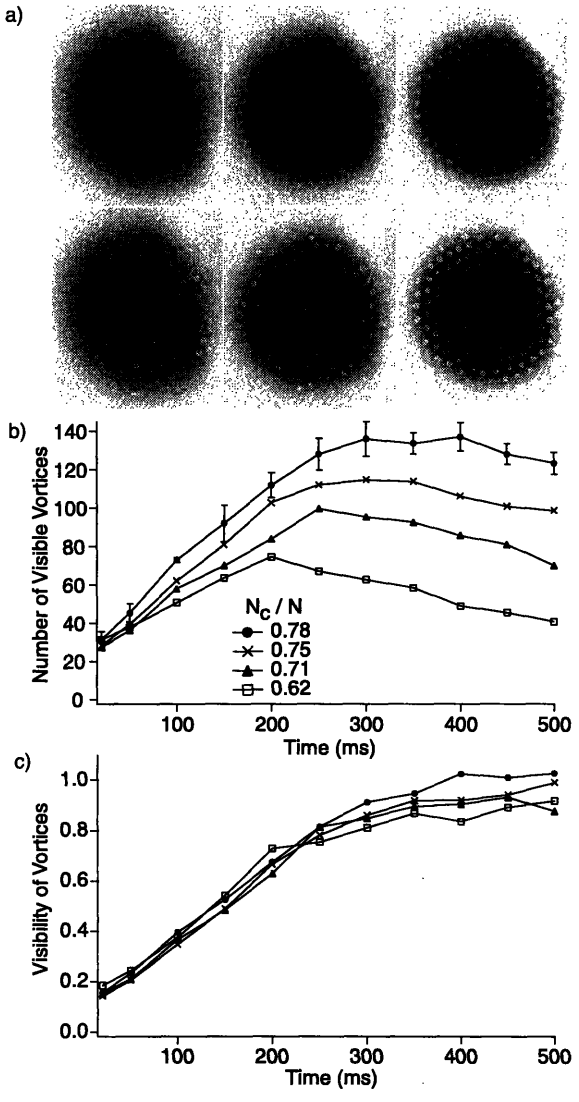

FIG. 4. Crystallization of the vortex lattice. (a) The top row shows three condensates that have equilibrated for 50, 150, and 300 ms, respectively, and have 48, 86, and 140 vortices recognized as visible by our algorithm. The bottom row shows the same condensates with the visible vortices circled. The field of view was 1.4 by 1.6 mm. (b) Growth of the number of visible vortices for several temperatures expressed by the condensate fraction (N_c/N). (c) Visibility of vortices derived from the data in (b), normalized by the number of vortices inferred from centrifugal distortion measurements.

turn damped via friction with the trap anisotropy ($\mu_{\mathrm{th}-\epsilon_r}$). Even at our highest temperatures, $\mu_{c-\mathrm{th}}$ is sufficiently larger than $\mu_{\mathrm{th}-\epsilon_r}$ as to allow the thermal cloud to spin up to $\sim$2/3 of the lattice rotation rate. $\mu_{\mathrm{th}-\epsilon_r}$ is calculated in Ref. [17] for a classical Boltzmann gas. For our parameters the relaxation time τ_{rot} for the thermal cloud rotation is $\tau_{\mathrm{rot}} = 4\tau$, where τ is the relaxation time for quadrupolar deformations. τ is approximately 5/4 of the time between elastic collisions $\tau_{\mathrm{el}} = 2/n v_{\mathrm{th}} \sigma$ [18], where

n is the atomic density, v_{th} is the thermal velocity, and σ is the elastic cross section. For a quantum-saturated thermal cloud, this gives a relaxation time proportional to T^{-2}.

The presence of the condensate adds an additional moment of inertia, extending the rotational relaxation time by a factor $f_{\text{inertia}} = (I_{th} + I_c)/I_{th}$, where I_{th} and I_c are the moments of inertia of the thermal cloud and the condensate, respectively. At high temperatures this factor approaches 1, because the moment of inertia of the thermal cloud is dominant. For very low temperatures $f_{\text{inertia}} \sim (I_c/I_{th})$. This ratio is [6]

$$\frac{I_c}{I_{th}} = \frac{15\zeta(3)}{16\zeta(4)} \frac{N_c}{N_{th}} \frac{\mu}{k_B T}, \tag{2}$$

where the numerical prefactor is 1.04. Thus, for a noninteracting Bose gas in the low temperature limit, f_{inertia} scales as T^{-4} and the relaxation time of the vortex lattice should scale as T^{-6}. (For very round traps a weaker T^{-2} temperature dependence is expected, due to the τ^{-1} scaling of the thermal cloud relaxation time.) The observed temperature dependence of the relaxation time, decreasing by a factor of 17 for a 60% increase in the temperature, agrees fortuitously well given the approximations made in the theory. The absolute relaxation rates predicted by Refs. [6,17] are on the order of 1 s^{-1}, in reasonable agreement with our results. However, for a quantitative comparison to theory it will be necessary to further characterize the rotating thermal cloud, which may not be in full equilibrium.

In contrast to the decay, the crystallization process of the vortex lattice was essentially independent of temperature. This was unexpected because all dissipative processes observed thus far in BECs, including the decay of the vortex lattice, have shown a strong temperature dependence [19,20]. Feder [21] has numerically simulated a stirred condensate using only the Gross-Pitaevskii equation. The results show that the absence of dissipation leads to a rapid, irregular motion of the vortices. The addition of a phenomenological dissipative term in Ref. [5] resulted in the formation of triangular vortex lattices. However, the origin of the dissipation was not identified. Our results suggest that the time-limiting step for the evolution of a vortex tangle into a regular lattice does not strongly depend on temperature. One possibility is that the thermal cloud is not directly involved. This may be similar to the reconnection of vortices or the damping of Kelvin modes, where the spontaneous creation of excitations acts as a dissipative mechanism [22]. Another possibility is that the rearrangement of the vortices into a rectilinear lattice is slow and not limited by dissipation. Our quantitative analysis of the formation process seems to contradict qualitative observations made in Paris [8], in which the lattice ordering appeared to have temperature dependence. This indicates that further study may be necessary to fully characterize the role of the thermal cloud in the formation process.

In conclusion, we have studied the crystallization and decay of vortex lattices. Both processes are dissipative and require physics beyond the Gross-Pitaevskii equation. The dynamics of vortices nicely illustrates the interplay of experiment and theory in the field of BEC.

The authors acknowledge T. Rosenband for the development of the vortex recognition algorithm. We also thank J. M. Vogels and K. Xu for their experimental assistance and J. R. Anglin, Z. Hadzibabic, A. E. Leanhardt, and R. Onofrio for insightful discussions. This research is supported by NSF, ONR, ARO, NASA, and the David and Lucile Packard Foundation.

*Electronic address: jamil@mit.edu
†Present address: School of Physics, Georgia Institute of Technology, Atlanta, Georgia 30332-0430.

[1] F. Dalfovo, S. Giorgini, L. P. Pitaevskii, and S. Stringari, Rev. Mod. Phys. **71**, 463 (1999).
[2] A. L. Fetter and A. A. Svidzinsky, J. Phys. Condens. Matter **13**, R135 (2001).
[3] F. Dalfovo and S. Stringari, Phys. Rev. A **63**, 011601 (2001).
[4] J. R. Anglin, cond-mat/0106619.
[5] M. Tsubota, K. Kasamatsu, and M. Ueda, cond-mat/0104523.
[6] O. N. Zhuravlev, A. E. Muryshev, and P. O. Fedichev, cond-mat/0007246.
[7] P. O. Fedichev and A. E. Muryshev, cond-mat/0004264.
[8] K. W. Madison, F. Chevy, W. Wohlleben, and J. Dalibard, Phys. Rev. Lett. **84**, 806 (2000).
[9] J. R. Abo-Shaeer, C. Raman, J. M. Vogels, and W. Ketterle, Science **292**, 476 (2001).
[10] E. Hodby, G. Hechenblaikner, S. A. Hopkins, and O. M. Maragò, and C. J. Foot, cond-mat/0106262.
[11] P. C. Haljan, I. Coddington, P. Engels, and E. A. Cornell, cond-mat/0106362.
[12] P. C. Haljan, B. P. Anderson, I. Coddington, and E. A. Cornell, Phys. Rev. Lett. **86**, 2922 (2000).
[13] C. Raman, J. R. Abo-Shaeer, J. M. Vogels, K. Xu, and W. Ketterle, Phys. Rev. Lett. **87**, 210402 (2001).
[14] R. Onofrio, D. S. Durfee, C. Raman, M. Köhl, C. E. Kuklewicz, and W. Ketterle, Phys. Rev. Lett. **84**, 810 (2000).
[15] P. Nozières and D. Pines, *The Theory of Quantum Liquids* (Addison-Wesley, Redwood City, CA, 1990).
[16] S. Giorgini, L. P. Pitaevskii, and S. Stringari, J. Low Temp. Phys. **109**, 309 (1997).
[17] D. Guéry-Odelin, Phys. Rev. A **62**, 033607 (2000).
[18] D. Guéry-Odelin, F. Zambelli, J. Dalibard, and S. Stringari, Phys. Rev. A **60**, 4851 (1999).
[19] D. S. Jin, M. R. Matthews, J. R. Ensher, C. E. Wieman, and E. A. Cornell, Phys. Rev. Lett. **78**, 764 (1997).
[20] D. M. Stamper-Kurn, H.-J. Miesner, S. Inouye, M. R. Andrews, and W. Ketterle, Phys. Rev. Lett. **81**, 500 (1998).
[21] D. L. Feder, MIT-Harvard Center for Ultracold Atoms Seminar, 2001.
[22] M. Leadbeater, T. Winiecki, D. C. Samuels, C. F. Barenghi, and C. S. Adams, Phys. Rev. Lett. **86**, 1410 (2001).

Appendix D

Dissociation and Decay of Ultracold Sodium Molecules

T. Mukaiyama, J.R. Abo-Shaeer, K. Xu, J.K. Chin, and W. Ketterle

"Dissociation and Decay of Ultracold Sodium Molecules,"

Phys. Rev. Lett. 92 180402 (2004).

Dissociation and Decay of Ultracold Sodium Molecules

T. Mukaiyama, J. R. Abo-Shaeer, K. Xu, J. K. Chin, and W. Ketterle
Department of Physics, MIT-Harvard Center for Ultracold Atoms, and Research Laboratory of Electronics, Massachusetts Institute of Technology, Cambridge, Massachusetts 02139, USA
(Received 24 November 2003; published 4 May 2004)

The dissociation of ultracold molecules was studied by ramping an external magnetic field through a Feshbach resonance. The observed dissociation energies directly yielded the strength of the atom-molecule coupling. They showed nonlinear dependence on the ramp speed. This was explained by a Wigner threshold law which predicts that the decay rate of the molecules above threshold increases with the density of states. In addition, inelastic molecule-molecule and molecule-atom collisions were characterized.

DOI: 10.1103/PhysRevLett.92.180402 PACS numbers: 03.75.Nt, 32.80.Pj, 33.80.Ps, 34.20.Cf

Recently, it has become possible to create ultracold molecular gases from precooled atomic samples [1–11]. Extending the ultralow temperature regime from atoms to molecules is an important step towards controlling the motion of more complicated objects. The complex structure of molecules may lead to new scientific opportunities, including the search for a permanent electric dipole moment, with sensitivity much higher than for heavy atoms [12], and the realization of quantum fluids of bosons and fermions with anisotropic interactions [13]. Furthermore, stable mixtures of atomic and molecular condensates are predicted to show coherent stimulation of atom-molecule or molecule-atom conversion, constituting quantum-coherent chemistry [14].

To date, all realizations of ultracold molecules (< 1 mK) have bypassed the need for direct cooling of the molecules, which is difficult due to the complicated rovibrational structure. Rather, molecules were formed from ultracold atoms using Feshbach resonances [2–11], where a highly vibrational excited molecular state is magnetically tuned into resonance with a pair of colliding atoms.

In this Letter, we study the dissociation and decay of such highly excited molecules. Figure 1 shows a schematic of the dissociation process. For magnetic fields above the Feshbach resonance, the molecular state crosses the free atomic states, shown here as discrete states in a finite quantization volume. The interaction between atoms and molecules turns these crossing into anticrossings. When the magnetic field is swept very slowly through the resonance, the molecules follow the adiabatic curve and end up in the lowest energy state of the atoms. For faster ramps, the molecular populations will partially cross some of the low-lying states, and the dissociation products will populate several atomic states. The stronger the coupling between the molecular state and the atomic states, the faster the molecules dissociate and the smaller the energy release in the dissociation. Observing the atom-molecule coupling in *one-body* decay (dissociation) is a new method to experimentally determine the strength of a Feshbach resonance. Previous measurements used *two-* or *three-body* processes to characterize the Feshbach resonance and therefore required accurate knowledge of the atomic density distribution.

Collisional properties of the molecules were also studied. Inelastic collisions limit both the production of molecules and their lifetime. We observed loss of molecules by collisions both with atoms and other molecules. These two processes were studied by separating atoms and molecules with a short pulse of laser light [9].

To generate molecules, sodium condensates in the $|F, m_F\rangle = |1, -1\rangle$ state were prepared in an optical dipole trap. The trap frequencies of 290 Hz in the radial direction and 2.2 Hz in the axial direction yielded typical densities of 1.7×10^{14} cm^{-3} for 5×10^6 atoms. Atoms were then spin-flipped using an adiabatic radio frequency sweep to the $|1, 1\rangle$ state, where a 1 G wide Feshbach resonance exists at 907 G [15].

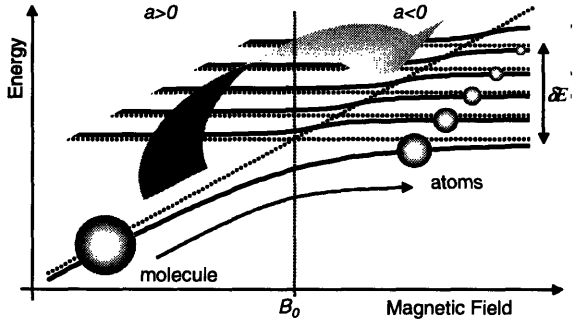

FIG. 1. Schematic diagram of energy levels for molecules and atoms. The diabatic energy levels are shown as dashed lines. The adiabatic curves (solid lines) include the atom-molecule coupling. When the magnetic field is swept from positive to negative scattering length, dissociated molecules end up in one or several atomic states, depending on the ramp rate of the magnetic field. The spheres represent the distribution of the population before and after the ramp.

 0031-9007/04/92(18)/180402(4)$22.50

The magnetic field sequence used to create and detect Na_2 molecules was identical to our previous work [9]. Briefly, the axial magnetic field was ramped to 903 G in 100 ms using two pairs of bias coils. In order to prepare the condensate on the negative scattering length side of the resonance, the field was stepped up to 913 G as quickly as possible (~ 1 μs) to jump through the resonance with minimal atom loss. The field was then ramped back down to 903 G in 50 μs to form molecules. In order to remove nonpaired atoms from the trap, the sample was irradiated with a 20 μs pulse of resonant light. Because 903 G is far from the Feshbach resonance, the mixing between atomic and molecular states was small and therefore molecules were transparent to this "blast" pulse. By ramping the field back to 913 G molecules were converted back to atoms. Absorption images were taken at high fields (either at 903 or 913 G) after 10 to 17 ms ballistic expansion, with the imaging light incident along the axial direction of the condensate.

To study the momentum distribution of the back-converted atoms, the magnetic field was ramped up immediately after turning off the optical trap, or for a reference, at the end of the ballistic expansion. The difference between the energies of ballistic expansion is the released dissociation energy. Energies were obtained from the rms width of the cloud $\langle x^2 \rangle$ as $E = 3m\langle x^2 \rangle / 2t^2$, where t is the ballistic expansion time and m is the atomic mass. Figure 2 shows that faster field ramps created hotter atoms.

An earlier theoretical treatment assumes a constant predissociation lifetime of the molecules and predicts a linear relation between dissociation energy and field ramp rate [16]. This theory predicts a much faster dissociation (and therefore smaller dissociation energy) than was observed. Furthermore, our data show a nonlinear dependence. Linear behavior would be expected if the lifetime of the molecules was independent of the energy ϵ from the dissociation threshold. The fact that the slope becomes smaller for increasing ramp rate indicates that the lifetime of molecules decreases with the ramp rate. As we show, this can be explained by an increase of the density of atomic states, leading to a $\sqrt{\epsilon}$ dependence of the molecular decay rate (Wigner threshold law [17]).

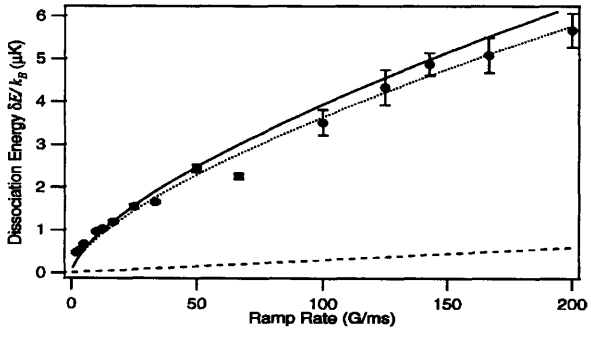

FIG. 2. Dissociation energy of molecules as a function of magnetic field ramp rate. The dashed line represents the linear relation described in Ref. [16], the solid line shows the result of our model using a theoretical value for $\Delta B = 0.98$ G and $a_{bg} = 3.4$ nm, and the dotted line shows a curve with the product $a_{bg}\Delta B$ as a fitting parameter.

The decay rate $\Gamma(\epsilon)$ follows from Fermi's golden rule as $\hbar\Gamma(\epsilon) = 2\pi|V_{ma}(\epsilon)|^2 D(\epsilon)$ [18], where V_{ma} is the matrix element between atomic and molecular states, which to leading order is independent of ϵ. The density of states $D(\epsilon)$ is given by

$$D(\epsilon) = \frac{V}{(2\pi)^2}\left(\frac{m}{\hbar^2}\right)^{3/2}\epsilon^{1/2}, \tag{1}$$

where V is the quantization volume for free atomic states.

An expression for the matrix element V_{ma} is obtained by comparing the energy shift near a Feshbach resonance with second-order perturbation theory. Assuming two atoms in a volume V, the energy shift of the low-lying continuum states due to the coupling with a bound molecular state is

$$\delta(\epsilon) = \frac{|V_{ma}|^2}{\epsilon} = \frac{|V_{ma}|^2}{\Delta\mu(B - B_0)}, \tag{2}$$

where $\Delta\mu$ is the difference between atomic and molecular magnetic moments, B is the applied magnetic field, and B_0 is the position of the Feshbach resonance.

The energy shift can also be expressed in terms of the mean field energy $4\pi\hbar^2 a/mV$, where $a = a_{bg}\Delta B/(B - B_0)$ is the scattering length near the Feshbach resonance (a_{bg} is the background scattering length and ΔB is the resonance width [19]):

$$\delta(\epsilon) = \frac{4\pi\hbar^2}{mV}\frac{a_{bg}\Delta B}{B - B_0}. \tag{3}$$

Comparing Eqs. (2) and (3) yields

$$|V_{ma}|^2 = \frac{4\pi\hbar^2}{mV}a_{bg}\Delta\mu\Delta B. \tag{4}$$

If the entire population is initially in the molecular state, the fraction of molecules, $m(\epsilon)$, at energy ϵ follows the rate equation,

$$\frac{dm(\epsilon)}{d\epsilon} = \frac{dm(\epsilon)}{dt}\left(\frac{d\epsilon}{dt}\right)^{-1} = \Gamma(\epsilon)m(\epsilon)\left(\frac{d\epsilon}{dt}\right)^{-1} \tag{5}$$

$$= \frac{2\pi|V_{ma}(\epsilon)|^2 D(\epsilon)}{\hbar\Delta\mu|\dot{B}|}m(\epsilon). \tag{6}$$

Using Eqs. (1) and (4), we solve the differential equation for $m(\epsilon)$,

$$m(\epsilon) = e^{-(2/3)C\epsilon^{3/2}}, \qquad C = \frac{2\Delta B}{\hbar\dot{B}}\sqrt{\frac{ma_{bg}^2}{\hbar^2}}. \tag{7}$$

In the laboratory frame, the atoms have kinetic energy $\epsilon/2$, and therefore the average energy of an atom after dissociation is

$$\delta E = \int_0^\infty \frac{\epsilon}{2}[-dm(\epsilon)] = 0.591\left(\sqrt{\frac{\hbar^2}{m a_{bg}^2}}\frac{\hbar \dot{B}}{2\Delta B}\right)^{2/3}. \quad (8)$$

Using theoretical values $a_{bg} = 3.4$ nm, $\Delta\mu/h = 3.65 \times 1.4$ MHz/G, and $\Delta B = 0.98$ G [20,21], the data show good agreement with our model. A fit of the product $a_{bg}\Delta B$ to our data results in $a_{bg}\Delta B = 3.64$ G nm $\pm$ 2% (dotted line in Fig. 2). The discrepancy between the theoretical and fitted values is 4 times bigger than the statistical error, but within the systematic error of the measurement of the release energy.

Further experiments with ultracold sodium molecules will critically depend on their collision properties. Therefore we also studied heating and inelastic collision processes. As shown in Fig. 3, we observed monotonic heating of the pure molecular sample over ~30 ms. In addition, we observed short time scale oscillations (6 ms) in the fitted temperature (inset of Fig. 3). Such breathing oscillations were excited because the molecules were formed over the volume of the atomic condensate and started oscillations around their equilibrium volume. The equilibrium volume deduced from the observed released energy is much smaller than the initial volume. The absence of damping implies a collision time of at least 6 ms, or a molecular scattering length smaller than 17 nm (obtained using the expression for the collision rate $8\pi a^2 v_{th} n_m$, where v_{th} is the thermal velocity). It is unclear whether the oscillation disappeared due to collisions or limited signal-to-noise ratio.

The temperature of the molecular cloud saturated at ~250 nK after 15 ms. A possible explanation is the balance between heating due to inelastic molecular decay and the evaporative cooling caused by the finite trap depth (1.7 μK). This would imply a collision time of 15 ms. However, we have no clear evidence that thermalization has occurred. Clearly, further studies of elastic collisions between ultracold molecules are necessary.

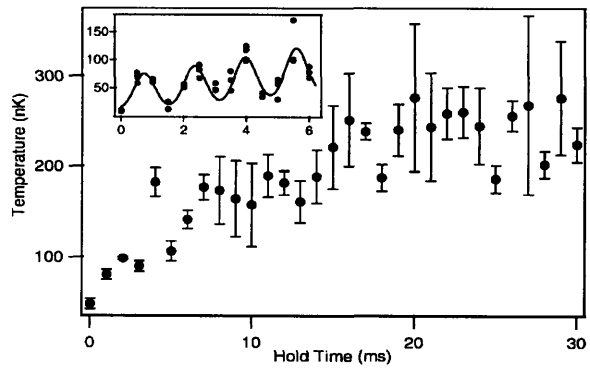

FIG. 3. Temperature of the molecular cloud. After 15 ms, the temperature saturates at ~250 nK. Error bars represent the statistical error (standard deviation). The inset shows finer resolution data for holding times up to 6 ms. The solid line is a guide to the eye.

Molecules formed via an s-wave Feshbach resonance are created in the rotational ground state, but in high vibrational states. Therefore, one expects vibrational relaxation to be a strong, inelastic decay mechanism.

Figure 4(a) shows the decay of a pure molecular sample. The decay was analyzed with the rate equation

$$\frac{\dot{N}_m}{N_m} = -K_{mm} n_m. \quad (9)$$

Here N_m, n_m is the number and the density of the molecules, respectively, and K_{mm} is the molecule-molecule collision rate coefficient. Because of the changing size and temperature of the molecular cloud during the first ~15 ms (Fig. 3), we fit data points only at later times, assuming a thermal equilibrium volume for the molecules. The decay at earlier times is slower, consistent with a larger molecular cloud. The fit yields a molecule-molecule collision coefficient of $K_{mm} \sim 5.1 \times 10^{-11}$ cm^3/s, about 2 orders of magnitude larger than the typical values reported for fermions [4,5].

Inelastic collisions between molecules and atoms were also observed by keeping atoms in the trap [Fig. 4(b)]. The decay was analyzed assuming that the loss of

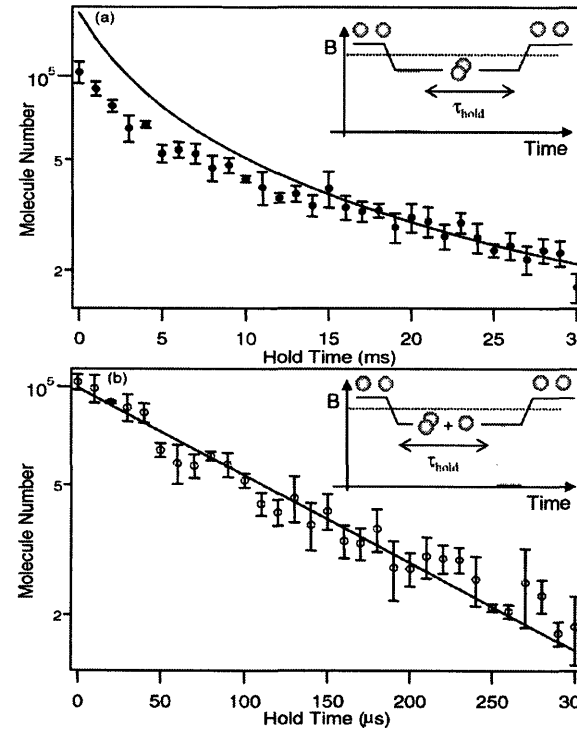

FIG. 4. Decay of ultracold molecules trapped alone (a) or together with atoms (b). The solid lines in (a) and (b) are fits of Eqs. (9) and (10) to data, which assume vibrational relaxation in the collision of m olecules (a) or collisions between molecules and atoms (b). The insets illustrate the experimental sequences.

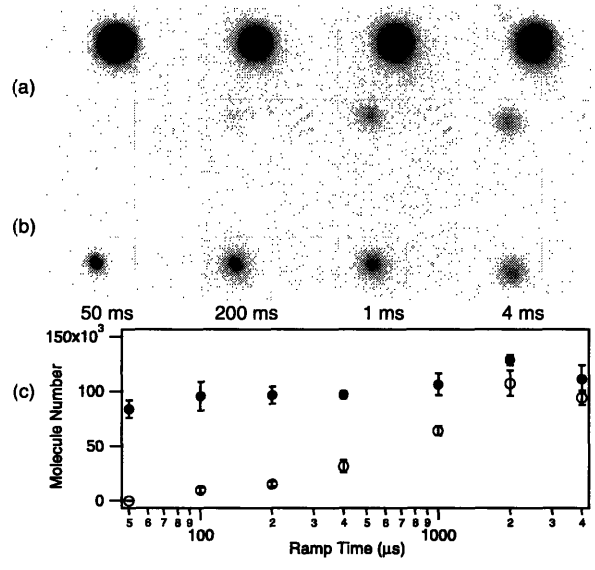

FIG. 5. Conversion of atoms to molecules for various ramp times. During a given time, the magnetic field was swept by 10 G. (a) and (b) show absorption images taken after 14 ms time of flight. The molecules (bottom) were radially separated from the atoms (top) by a field gradient of 2.8 G/cm. The molecules were converted back to atoms only 0.5 ms before imaging by ramping the magnetic field back across the Feshbach resonance. This time was chosen to be long enough for any transient field fluctuations to damp out, but short enough such that the size of the imaged cloud reflected the molecular temperature, not the dissociation energy. (a) The atoms remained in the trap. (b) The atoms were removed by a resonant laser pulse immediately after the magnetic field ramp. (c) Number of molecules as a function of ramp time for (a) (open circles) and (b) (closed circles).

molecules occurred mainly due to collisions with atoms, resulting in an exponential decay:

$$\frac{\dot{N}_m}{N_m} = -K_{am} n_a. \tag{10}$$

Here n_a is the density of atoms, and K_{am} is the atom-molecule collision rate coefficient. From the fit, we extract a lifetime of 106 μs and a rate coefficient $K_{am} \sim 5.5 \times 10^{-11}$ cm^3/s, which agrees well with theoretical predictions [21,22].

The inelastic losses determine the maximum conversion efficiency from atoms to molecules. For an adiabatic ramp, one expects close to 100% conversion efficiency. Indeed, in experiments with fermionic atoms, efficiencies up to 85% have been observed [5]. Figure 5 shows the results for magnetic field ramps of different durations. The two sets of images show that applying the blast pulse dramatically improved the molecular number and temperature. Without it, a slower ramp time (4 ms) appeared to be more favorable for molecule formation [open circles in Fig. 5(c)]. No molecules were observed for a 50 μs ramp time. However, with the blast pulse, a similar number of molecules was obtained for all ramp times between 50 μs to 4 ms [closed circles in Fig. 5(c)].

We assume that these results reflect the interplay of two competing processes. The adiabatic condition requires a relatively slow field ramp for efficient conversion. However, this means that the atoms and molecules spend more time near or at the Feshbach resonance, where inelastic collision rates are enhanced. In contrast to Fig. 5(b), the absence of a molecular signal in Fig. 5(a) for 50 μs ramp time reflects that the atomic density reduction due to the ballistic expansion is too slow for the molecules to survive the inelastic collisions with the atoms.

In conclusion, we observed a Wigner threshold behavior in the dissociation of ultracold molecules. We were able to characterize a Feshbach resonance using a one-body decay (dissociation) process. The rapid decay of the molecules due to collisions with atoms and other molecules imposes a severe limit to further evaporative cooling for bosons. This also explains the low conversion efficiency ($\sim 4\%$), in contrast to recent experiments with fermions.

The authors thank D. E. Miller for experimental assistance and A. E. Leanhardt, M. Saba, and D. Schneble for their critical reading of the manuscript. We also thank P. S. Julienne, B. J. Verhaar, and V. A. Yurovsky for useful discussion. This research is supported by NSF, ONR, ARO, and NASA.

[1] R. Wynar *et al.*, Science **287**, 1016 (2000).
[2] E. A. Donley *et al.*, Nature (London) **417**, 529 (2002).
[3] C. A. Regal *et al.*, Nature (London) **424**, 47 (2003).
[4] S. Jochim *et al.*, Phys. Rev. Lett. **91**, 240402 (2003).
[5] J. Cubizolles *et al.*, Phys. Rev. Lett. **91**, 240401 (2003).
[6] K. E. Strecker *et al.*, Phys. Rev. Lett. **91**, 080406 (2003).
[7] S. Dürr *et al.*, Phys. Rev. Lett. **92**, 020406 (2003).
[8] C. Chin *et al.*, Phys. Rev. Lett. **90**, 033201 (2003).
[9] K. Xu *et al.*, Phys. Rev. Lett. **91**, 210402 (2003).
[10] M. Greiner *et al.*, Nature (London) **426**, 537 (2003).
[11] S. Jochim *et al.*, Science **302**, 2101 (2003).
[12] J. J. Hudson *et al.*, Phys. Rev. Lett. **89**, 23003 (2002).
[13] M. Baranov *et al.*, Phys. Scr. **T102**, 74 (2002).
[14] D. J. Heinzen *et al.*, Phys. Rev. Lett. **84**, 5029 (2000).
[15] S. Inouye *et al.*, Nature (London) **392**, 151 (1998).
[16] F. A. van Abeelen and B. J. Verhaar, Phys. Rev. Lett. **83**, 1550 (1999).
[17] E. P. Wigner, Phys. Rev. **73**, 1002 (1948).
[18] F. H. Mies *et al.*, Phys. Rev. A **61**, 022721 (2000).
[19] E. Timmermans *et al.*, Phys. Rep. **315**, 199 (1999).
[20] V. A. Yurovsky *et al.*, Phys. Rev. A **60**, R765 (1999).
[21] V. A. Yurovsky *et al.*, Phys. Rev. A **62**, 043605 (2000).
[22] V. A. Yurovsky and A. Ben-Reuven, Phys. Rev. A **67**, 043611 (2003).

Appendix E

Coherent Molecular Optics using Sodium Dimers

J.R. Abo-Shaeer, D.M. Miller, J.K. Chin, K. Xu, T. Mukaiyama, and W. Ketterle *"Coherent Molecular Optics using Sodium Dimers,"* cond-mat/0409327 (2004).

Coherent Molecular Optics using Sodium Dimers

J.R. Abo-Shaeer*, D.E. Miller, J.K. Chin, K. Xu, T. Mukaiyama, and W. Ketterle†
Department of Physics, MIT-Harvard Center for Ultracold Atoms, and Research Laboratory of Electronics, MIT, Cambridge, MA 02139
(Dated: September 13, 2004)

Coherent molecular optics is performed using two-photon Bragg scattering. Molecules were produced by sweeping an atomic Bose-Einstein condensate through a Feshbach resonance. The spectral width of the molecular Bragg resonance corresponded to an instantaneous temperature of 20 nK, indicating that atomic coherence was transferred directly to the molecules. An autocorrelating interference technique was used to observe the quadratic spatial dependence of the phase of an expanding molecular cloud. Finally, atoms initially prepared in two momentum states were observed to cross-pair with one another, forming molecules in a third momentum state. This process is analogous to sum-frequency generation in optics.

PACS numbers: PACS 03.75.Fi, 34.20.Cf, 32.80.Pj, 33.80.Ps

Similar to the field of optics, where the high intensity and coherence of lasers allowed for the observation of effects such as frequency doubling and wave-mixing, atom optics has benefited greatly from the realization of Bose-Einstein condensates (BEC). High phase-space density (atoms per mode) and a uniform phase [1, 2] give the condensate its laser-like qualities. Although not fundamentally required [3, 4], BEC has led to the observation of such phenomena as four-wave mixing [5], matter wave amplification [6, 7], and atom number squeezing [8].

The current state of molecular optics is similar to atom optics prior to the realization of BEC. Diffraction and interferometry of thermal molecular beams has been demonstrated [9, 10, 11, 12], yet monoenergetic beams lack the density necessary to observe nonlinear effects. However, recent experiments using Feshbach resonances have demonstrated the conversion of degenerate atomic bosons [13, 14, 15] and fermions [16, 17, 18, 19, 20] into ultracold molecules. These sources have the potential to greatly advance molecular optics. Furthermore, atom-molecule coupling can be studied as the first steps towards "superchemistry", where chemical reactions are stimulated via macroscopic occupation of a quantum state [21].

The coherent manipulation of atomic matter waves via stimulated light scattering has been crucial in the development of nonlinear atom optics (for a review see [23]). Here we demonstrate the ability to apply Kapitza-Dirac and Bragg diffraction [24] to cold molecules. Using optical standing waves of suitably chosen frequencies, sodium dimers were coherently manipulated with negligible heating or other incoherent processes. First, we characterized the coherence of our "source" molecules, created via Feshbach resonance. By measuring the Bragg spectrum of the molecules immediately after their creation, the conversion from atoms to molecules was shown to be coherent - the matter wave analog to frequency doubling in optics. The quadratic spatial dependence of the phase of the expanding molecules was observed using an autocorrelation interference technique. By creating a duplicate sample of molecules and overlapping it with the original, matter wave interference was observed. Finally,

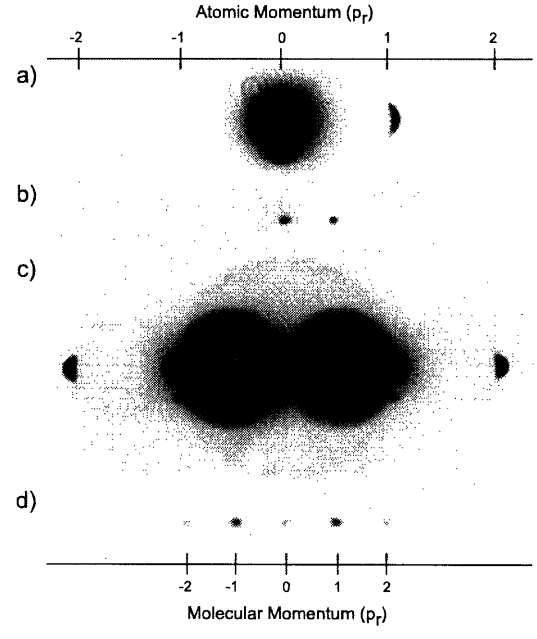

FIG. 1: Bragg diffraction of (a) atoms and (b) molecules. Scattered particles recoil with identical momenta, p_r. However, during ballistic expansion diffracted molecules expand with half the velocity of atoms, due to their doubled mass. The pulse duration in each image was 200 μs. A shorter pulse (5 μs) populated multiple (c) atomic and (d) molecular momentum states. The halos in (c) are due to collisions between different momentum states [22]. The time-of-flight in each image is 17 ms.

*Contact Info: jamil@mit.edu
†Website: cua.mit.edu/ketterle_group

the matter wave analog to sum-frequency generation was demonstrated. Atoms prepared in two momentum states, prior to creating molecules, were observed to cross-pair, generating a third momentum state.

To produce molecules, sodium condensates were prepared in a crossed optical dipole trap in the $|F, m_F\rangle = |1, -1\rangle$ state. Trap frequencies of $(\omega_x, \omega_y, \omega_z) = 2\pi\times(146, 105, 23)$ Hz yielded a typical peak density of $n_0 \simeq 4.3 \times 10^{14}$ cm^{-3} for 25 million atoms. Atoms were then spin-flipped to the $|1, 1\rangle$ state, in which a 1 G wide Feshbach resonance exists at 907 G [25].

The magnetic field sequence used to create and detect Na_2 molecules was identical to our previous work [15, 26]. Briefly, the axial (z-axis) magnetic field was ramped to 903 G in 100 ms. In order to prepare the condensate on the negative scattering length side of the resonance, the field was stepped up to 913 G as quickly as possible ($\sim$ 1 μs) to jump through the resonance with minimal atom loss. After waiting 1200 μs for the transient field to die down, the field was ramped back down to 903 G in 50 μs to form molecules. In order to remove non-paired atoms from the trap, the sample was irradiated with a 10 μs pulse of resonant light. Because 903 G is far from the Feshbach resonance, the mixing between atomic and molecular states was small, and therefore molecules were transparent to this "blast" pulse. By ramping the field back to 913 G, molecules were converted back to atoms. Absorption images were taken at high fields (either at 903 G or 913 G), with the imaging light incident along the axial direction of the condensate. Bragg scattering of atoms and molecules was carried out using two nearly orthogonal beams ($\theta_B = 84°$), aligned such that particles were scattered along the x-axis of the trap. The beams were far-detuned from atomic/molecular transitions to limit spontaneous scattering. For atoms the detuning was $\simeq$ 4 nm from the sodium D lines. To find a suitable transition for the molecules, we scanned the laser wavelength and measured the Rabi frequency for Bragg transitions. Several narrow transitions were observed, but not carefully characterized. For this work the laser was set to 590.159 nm, yielding a Rabi frequency of 2 kHz and corresponding to an effective detuning of $\sim$ 50 MHz from the resonance.

Fig 1 shows time-of-flight images of Bragg scattering for atoms and molecules. Because the kinetic energy of the scattered particles was much larger than their mean-field energy, individual momentum states were well-resolved in ballistic expansion. Both atoms and molecules receive equal two-photon recoil momentum, $p_r = 2h\sin(\theta_B/2)/\lambda_L$, where λ_L is is the wavelength of the Bragg beams. However, scattered molecules move away from the central peak with half the velocity of atoms, owing to their doubled mass. Fig 1c,d show Kapitza-Dirac scattering, where multiple atomic and molecular momentum states were populated due to the broad frequency distribution of the short pulse (5 μs).

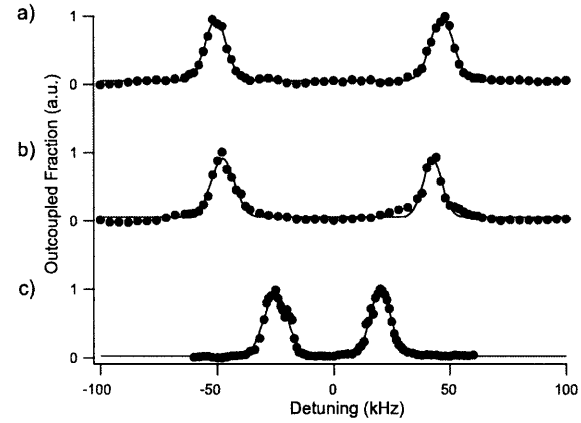

FIG. 2: Bragg spectra for atoms and molecules. In (a) the spectrum is taken for a pure atomic sample above the Feshbach resonance. (b) and (c) are spectra of atoms and molecules, respectively, below the resonance. In (c) atoms were removed from the trap with resonant light to limit losses due to atom-molecule collisions. The Bragg resonance condition for molecules occurs at half the frequency of the atomic resonance.

In order to study the coherence properties of the sample, Bragg spectra [1] were taken by pulsing on the two laser beams for 250 μs ($\sim$ 1 kHz resolution), before releasing the particles from the trap. For noninteracting particles, the Bragg resonance occurs at a relative detuning of $\nu_0 = \pm p_r^2/2mh$ between the beams, where the sign of ν_0 dictates the direction of out-coupling. Interactions in a condensate give rise to a mean-field shift of the resonance $\delta\nu = 4n_0U/7h$, where U=$4\pi\hbar^2a/m$ and a is the scattering length. Fig 2 shows three spectra for (a) atoms above the Feshbach resonance, as well as (b) atoms and (c) molecules after sweeping through the resonance. The reduced mean-field shift for atoms below the resonance (Fig 1b) can be attributed to inelastic losses caused by passing through the resonance. Atoms below the resonance coexisted with a small fraction of molecules (2%). The peak output for each set of data is normalized to 1. The actual peak out-coupled fractions were 0.06 for the atoms and 0.5 for the molecules. The atomic signal was kept intentionally low to minimize collisions, which make the data analysis difficult (see halos in Fig 1c). As expected from the resonance condition, molecular resonances occur at half the frequency of atomic resonances.

Two mechanisms contribute to the fundamental width of the Bragg resonance [1, 27]. For a parabolic density distribution, the finite size of the sample yields a momentum spread

$$\Delta\nu_p = 1.58\frac{p_r}{2\pi m x_0}, \quad (1)$$

where x_0 is the Thomas-Fermi radius. In addition, the inhomogeneous density distribution of the sample pro-

duces a spread in mean-field energy

$$\Delta\nu_n = \sqrt{\frac{8}{147}}\frac{n_0 U}{h}. \quad (2)$$

The fundamental width is approximately given by the quadrature sum of these two broadening mechanisms $\Delta\nu = \sqrt{\Delta\nu_n^2 + \Delta\nu_p^2}$.

The fundamental width, $\Delta\nu$, and measured rms width, $\overline{\sigma}$, are compared for each case in Table I. n_0 and x_0 were determined from the size of the condensate in time-of-flight. The measured widths cannot be accounted for by fundamental broadening mechanisms alone. For atoms above resonance, the fundamental width is $\Delta\nu$=1.39 kHz, compared to the measured value of 4.46 kHz. Therefore, another broadening mechanism must contribute $\sim$ 4 kHz to the width. Most likely this is due to Doppler broadening caused by random center-of-mass motion and other collective excitations of the condensate. This was investigated by mixing two frequencies into each Bragg beam to out-couple particles in both $\pm$x directions. For particles at rest, the out-coupling should always be symmetric. However, we observe the ratio of out-coupled particles in either direction to fluctuate. In addition we measure a small, consistent shift in the Bragg spectrum, indicating a drift velocity. A line broadening of 4 kHz corresponds to a velocity of $\simeq$ 2 mm/s, or a vibrational amplitude of $\simeq$ 2 μm (compared to $x_0 = 13\mu$m). This is not unreasonable, because the field ramping scheme used to bring the atoms to high field is violent and may induce collective excitations such as breathing modes.

Spectrum	$\Delta\nu$ (kHz)	$\overline{\sigma}$ (kHz)	T (nK)
Atoms (Above)	1.39	4.46(17)	10
Atoms (Below)	1.03	4.50(60)	10
Molecules	0.36 ‡	4.53(14)	20

TABLE I: Fundamental width ($\Delta\nu$), measured rms width ($\overline{\sigma}$), and the corresponding temperature (T), assuming a thermal distribution.
‡This lower bound assumes that the molecules have the same spatial profile as the atoms, which our results indicate is not the case.

Despite vibrational noise making the dominant contribution to the width of the spectra, the measured values are still narrow enough to indicate quantum degeneracy. For a given $\overline{\sigma}$, the corresponding temperature for a thermal distribution of particles is

$$T = \frac{m h^2 \overline{\sigma}^2}{k_B p_r^2} \quad (3)$$

Thus, for an rms width of 4.5 kHz, the temperature for a thermal distribution of molecules would be 20 nK, comparable to a previous value obtained using a time-of-flight technique [15]. The BEC transition temperature for our trap parameters and 5 x 10^4 molecules is much higher

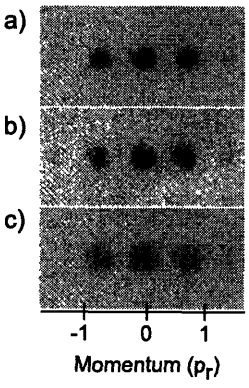

FIG. 3: Matter wave interference of molecules. (a) The molecular sample is split with a short Kapitza-Dirac pulse, creating two identical copies with momenta $\pm p_r$. (b)-(c) After the copies have separated for time $\Delta t = 100$ μs, a second pulse recombines them, giving rise to interference in each momentum component. The time-of-flight in each image is 12 ms.

(115 nK). This demonstrates a deeply degenerate, purely molecular sample, where as previous experiments have demonstrated coherent admixture of molecular character into an atomic BEC [28].

The molecular Bragg Spectrum showed a surprisingly large shift of $\delta\overline{\nu}$ = 625 Hz. If interpreted as a mean-field shift, this would imply either a very high density (possible due to a spatial collapse) or an anomalously large molecular scattering length outside the Feshbach resonance. Further study is necessary.

The spatial phase of the expanding molecular cloud was directly imaged using an autocorrelation method [29], which gives rise to the self-interference of the molecular sample (see Fig. 3). To accomplish this, two identical copies of the sample were made using a short Kapitza-Dirac pulse (10 μs), applied after 2 ms of ballistic expansion. The copies, with momentum $\pm p_r$, moved away from the zero momentum peak for time Δt before an identical pulse recombined them with the original. This type of interferometer has three readout ports, with momenta 0, $\pm p_r$. The straight-line interference fringes are characteristic of a quadratic spatial phase. The fringe spacing we measure is consistent with $\lambda_f = ht/md$ [30], where $d = p_r \Delta t/m$ is the distance the copies moved between pulses [31]. Interference fringes can only be resolved for small d. Therefore, this method cannot be used to observe coherence lengths longer than those inferred from Bragg spectroscopy. It should be noted that the appearance of interference fringes does not imply that the sample is condensed. Rather, it demonstrates only that the coherence length in time-of-flight is longer than the separation d. Therefore, similar interference can also be observed for a cloud of thermal atoms [32, 33].

The conversion of atoms to molecules may be viewed as the atom optic equivalent of frequency doubling [34]. The

relevant Hamiltonian for the atom-molecule coupling has the same form as that for the optical frequency doubling process:

$$a_{2m}^{\dagger} a_m a_m \tag{4}$$

where a_m is the annihilation operator for the atomic field and $a_{2m}^{\dagger}$ is the creation operator for the molecular field. The measurement of the Bragg spectrum shows that the sharp "linewidth" of the seed (atom) laser is inherited by the molecular laser. In nonlinear optics, photon interactions are typically mediated by a refractive medium. Here, the nonlinearity arises from the atoms themselves, in the form of s-wave interactions. The high density, or "brightness", of the source, together with the enhanced interactions at the Feshbach resonance provide the means to combine two matter waves. By combining two disparate matter waves, rather than identical ones, we extend the analogy of frequency doubling to the more general process of sum frequency generation. To do this, atoms were initially prepared in momentum states 0, 1 (in units of p_r). By sweeping through the resonance, molecules were produced in three momentum states: 0, 1, and 2 (see Fig. 4). States 0 and 2 are simply the frequency doubled components of the two initial matter waves. State 1 however, results from cross pairing between the initial momentum states, and is thus their sum frequency. This is the first time that a Feshbach resonance was observed between atoms colliding with a controlled non-vanishing momentum. The Feshbach resonance should be slightly shifted compared to the resonance for atoms at rest, which reflects the same physics encountered in the temperature dependence of the position of the resonance [35].

In conclusion, we have demonstrated coherent molecular optics using standing light waves. The ability to coherently convert atoms into molecules makes molecular optics even richer than atom optics. In addition, the techniques demonstrated in this paper could prove useful for probing molecules formed in quantum-degenerate fermi systems, and possibly even Cooper pairs.

The authors would like to acknowledge M. Boyd and W. Setiawan for experimental contributions and thank A.E. Leanhardt and M. W. Zwierlein for critical readings of the manuscript. This research is supported by NSF, ONR, ARO, and NASA.

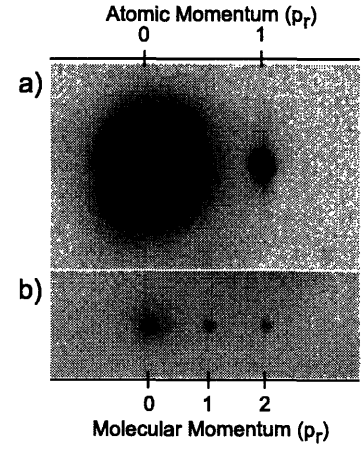

FIG. 4: Sum frequency generation of atomic matter waves. (a) Atoms were initially prepared in momentum states 0, 1. (b) By sweeping through the Feshbach resonance, atoms combine to form molecules with momenta 0, 1, and 2. Momentum state 1 is the sum frequency of the two atomic matter waves. The "nonlinear medium" is provided by the atomic interactions. The time-of-flight in each image is 17 ms.

[1] J. Stenger *et al.*, Phys. Rev. Lett. **82**, 4569 (1999).
[2] E. W. Hagley *et al.*, Phys. Rev. Lett. **83**, 3112 (1999).
[3] M. G. Moore and P. Meystre, Phys. Rev. Lett. **86**, 4199 (2001).
[4] W. Ketterle and S. Inouye, Phys. Rev. Lett. **86**, 4203 (2001).
[5] L. Deng *et al.*, Nature **398**, 218 (1999).
[6] S. Inouye *et al.*, Nature **402**, 641 (1999).
[7] M. Kozuma *et al.*, Science **286**, 2309 (1999).
[8] C. Orzel *et al.*, Science **291**, 2386 (2001).
[9] C. Bordé *et al.*, Phys. Lett. A **188**, 187 (1994).
[10] M. S. Chapman *et al.*, Phys. Rev. Lett. **74**, 4783 (1995).
[11] L. Hackermüller *et al.*, Phys. Rev. Lett. **91**, 090408 (2003).
[12] H. Sakai *et al.*, Phys. Lett. A **57**, 27942801 (1998).
[13] S. Dürr *et al.*, Phys. Rev. Lett. **92**, 020406 (2003).
[14] J. Herbig *et al.*, Science **301**, 1510 (2003).
[15] K. Xu *et al.*, Phys. Rev. Lett. **91**, 210402 (2003).
[16] C. A. Regal *et al.*, Nature **424**, 47 (2003).
[17] S. Jochim *et al.*, Science **302**, 2101 (2003).
[18] M. W. Zwierlein *et al.*, Phys. Rev. Lett. **91**, 250401 (2003).
[19] J. Cubizolles *et al.*, Phys. Rev. Lett. **91**, 240401 (2003).
[20] K. E. Strecker *et al.*, Phys. Rev. Lett. **91**, 080406 (2003).
[21] D. J. Heinzen *et al.*, Phys. Rev. Lett. **84**, 5029 (2000).
[22] A. P. Chikkatur *et al.*, Phys. Rev. Lett. **85**, 483 (2000).
[23] S. L. Rolston and W. D. Phillips, Nature Insight **416**, 219 (2002).
[24] M. Kozuma *et al.*, Phys. Rev. Lett. **82**, 871 (1999).
[25] S. Inouye *et al.*, Nature **392**, 151 (1998).
[26] T. Mukaiyama *et al.*, Phys. Rev. Lett. **92**, 180402 (2004).
[27] J. Stenger *et al.*, Phys. Rev. Lett. **84**, 2283 (2000), erratum.
[28] E. A. Donley *et al.*, Nature **417**, 529 (2002).
[29] J. Simsarian *et al.*, Phys. Rev. Lett. **85**, 2040 (2000).
[30] M. R. Andrews *et al.*, Science **275**, 637 (1997).
[31] Strictly speaking, this analysis only applies to the outcoupled ports. The center port is comprised of three copies.
[32] I. Bloch *et al.*, Nature **403**, 166 (2000).
[33] D. Miller *et al.*, in Preparation (2004).
[34] B. Saleh and M. Teich, *Fundamentals of Photonics* (Wiley, New York, 1991).
[35] V. Vuletić *et al.*, Phys. Rev. Lett. **83**, 943 (1999).

Bibliography

[1] J. R. Abo-Shaeer, C. Raman, and W. Ketterle. Formation and Decay of Vortex Lattices in Bose-Einstein Condensates at Finite Temperatures. *Phys. Rev. Lett.*, 88:070409, 2002.

[2] J. R. Abo-Shaeer, C. Raman, J. M. Vogels, and W. Ketterle. Observation of Vortex Lattices in Bose-Einstein Condensates. *Science*, 292:476–479, 2001.

[3] J.R. Abo-Shaeer, D.M. Miller, J.K. Chin, K. Xu, T. Mukaiyama, and W. Ketterle. Coherent Molecular Optics using Sodium Dimers. 2004. cond-mat/0409327.

[4] A. A. Abrikosov. *Sov. Phys. JETP*, 5:1174, 1957. Zh. Eksp. Teor. Fiz. 32, p. 1442(1957).

[5] A. Aftalion and T. Riviere. Vortex energy and vortex bending for a rotating Bose-Einstein condensate. *Phys. Rev. A*, 64:043611, 2002.

[6] B. P. Anderson and P. Meystre. Nonlinear atom optics. *Contemporary Physics*, 44:473, 2003.

[7] M. R. Andrews, C. G. Townsend, H.-J. Miesner, D. S. Durfee, D. M. Kurn, and W. Ketterle. Observation of interference between two Bose condensates. *Science*, 275:637–641, 1997.

[8] J. T. Bahns, W. C. Stwalley, and P. L. Gould. Laser cooling of molecules: A sequential scheme for rotation, translation, and vibration. *J. Chem. Phys.*, 104:9689–9697, 1998.

[9] Hendrick L. Bethlem, Giel Berden, and Gerard Meijer. Decelerating neutral dipolar molecules. *Phys. Rev. Lett.*, 83:1558–1561, 1999.

[10] I. Bloch, T. W. Hänsch, and T. Esslinger. Measurement of the spatial coherence of a trapped Bose gas at the phase transition. *Nature*, 403:166–170, 2000.

[11] C.J. Bordé, N. Courteir, F.D. Buck, A.N. Goncharov, and M. Gorlicki. Molecular interferometry experiments. *Phys. Lett. A*, 188:187–197, 1994.

[12] D.C. Burnham and D.L. Weinberg. Observation of simultaneity in parametric production of optical photon pairs. *Phys. Rev. Lett.*, 25:84–87, 1970.

[13] L. J. Campbell and R. M. Ziff. *Phys. Rev. B*, 20:1886, 1979.

[14] Y. Castin and R. Dum. Bose-Einstein condensation in time dependent traps. *Phys. Rev. Lett.*, 77:5315–5319, 1996.

[15] Michael S. Chapman, Christopher R. Ekstrom, Troy D. Hammond, Richard A. Rubenstein, Jörg Schmiedmayer, Stefan Wehinger, and David E. Pritchard. Optics and interferometry with Na2 molecules. *Phys. Rev. Lett.*, 74:4783–4786, 1995.

[16] F. Chevy, K. W. Madison, V. Bretin, and J. Dalibard. Formation of quantized vortices in a gaseous Bose-Einstein condensate. Proceedings of Trapped Particles and Fundamental Physics Workshop (Les Houches 2001), Editor : S. Atutov, K. Kalabrese, L. Moi.

[17] A. P. Chikkatur, A. Grlitz, D. M. Stamper-Kurn, S. Inouye, S. Gupta, and W. Ketterle. Suppression and enhancement of impurity scattering in a Bose-Einstein condensate. *Phys. Rev. Lett.*, 85:483–486, 2000.

[18] J. Cubizolles, T. Bourdel, S. J. J. M. F. Kokkelmans, G. V. Shlyapnikov, and C. Salomon. Bose-Einstein condensation of molecules. *Phys. Rev. Lett.*, 91:240401, 2003.

[19] F. Dalfovo, S. Giorgini, M. Guilleumas, L. P. Pitaevskii, and S. Stringari. Collective and single-particle excitations of a trapped Bose gas. *Phys. Rev. A*, 56:3840–3845, 1997.

[20] J. Dalibard. Collisional dynamics of ultra-cold atomic gases. Proceedings of the International School of Physics Enrico Fermi, Course CXL, pages 321–349. IOS Press, Amsterdam, 1999.

[21] C. Davisson and L. H. Germer. Diffraction of electrons by a crystal of nickel. *Phys. Rev.*, 30:705–740, 1927.

[22] C.J Davisson and L.H. Germer. Scattering of electrons by a single crystal of nickel. *Nature*, 119:558–560, 1927.

[23] L. Deng, E. W. Hagley, J. Wen, M. Trippenbach, Y. Band, P. S. Julienne, J. E. Simsarian, K. Helmerson, S. L. Rolston, and W. D. Phillips. Four-wave mixing with matter waves. *Nature*, 398:218, 1999.

[24] J. Denschlag, D. Cassettari, and J. Schmiedmayer. Guiding neutral atoms with a wire. *Phys. Rev. Lett.*, 82:2014–2017, 1999.

[25] E. A. Donley, N. R. Claussen, S. T. Thompson, and C. E. Wieman. Atom-molecule coherence in a BoseEinstein condensate. *Nature*, 417:529, 2002.

[26] R. J. Donnelly. *Quantized vortices in helium II.* Cambridge University Press, Cambridge, 1991.

[27] D.S. Durfee. *Dynamic Properties of Dilute Bose-Einstein Condensates.* PhD thesis, Massachusetts Institute of Technology, 1999.

[28] S. Dürr, T. Volz, A. Marte, and G. Rempe. Observation of molecules produced from a Bose-Einstein condensate. *Phys. Rev. Lett.*, 92:020406, 2003.

[29] J. Estermann and O. Stern. *Z. Physik*, 61:95, 1930.

[30] D. L. Feder, A. A. Svidzinsky, A. L. Fetter, and C. W. Clark. Anomalous modes drive vortex dynamics in confined Bose-Einstein condensates. *Phys. Rev. Lett.*, 86:564–567, 2001.

[31] P. O. Fedichev and A. E. Muryshev. preprint cond-mat/0004264.

[32] H. Feshbach. A unified theory of nuclear reactions. *Annals of Physics*, 19:287, 1962.

[33] A. L. Fetter and A. A. Svidzinsky. Vortices in a trapped dilute Bose-Einstein condensate. *J. Phys.: Condens. Matter*, v. 13, No 12, p. R135-R194,2001.

[34] P.A. Franken, A.E. Hill, C.W. Peters, and G. Weinreich. Generation of optical harmonics. *Phys. Rev. Lett.*, 7:118–119, 1961.

[35] J. J. García-Ripoll and V. M. Pérez-García. preprint cond-mat/0006368.

[36] J. J. García-Ripoll and V. M. Pérez-García. Vortex bending and tightly packed vortex lattices in Bose-Einstein condensates. *Phys. Rev. A*, 64:053611, 2001.

[37] M. Greiner, O. Mandel, T. Esslinger, T. W. Hnsch, and I. Bloch. Quantum phase transition from a superfluid to a mott insulator in a gas of ultracold atoms. *Nature*, 415:39–44, 2002.

[38] S. Gupta, A. E. Leanhardt, A. D. Cronin, and D. E. Pritchard. Coherent manipulation of atoms with standing light waves. *C. R. Acad. Sci. IV-Phys.*, 2:479–495, April-May 2001.

[39] L. Hackermüller, S. Uttenthaler, K. Hornberger, E. Reiger, B. Brezger, A. Zeilinger, and M. Arndt. Wave nature of biomolecules and fluorofullerenes. *Phys. Rev. Lett.*, 91:090408, 2003.

[40] E. W. Hagley, L. Deng, M. Kozuma, M. Trippenbach, Y. B. Band, M. Edwards, M. Doery, P. S. Julienne, K. Helmerson, S. L. Rolston, and W. D. Phillips. Measurement of the coherence of a Bose-Einstein condensate. *Phys. Rev. Lett.*, 83:3112–3115, 1999.

[41] P. C. Haljan, I. Coddington, P. Engels, and E. A. Cornell. Driving Bose-Einstein-condensate vorticity with a rotating normal cloud. *Phys. Rev. Lett.*, 87:210403–4, 2001.

[42] W. Hänsel, P. Hommelhoff, T.W. Hänsch, and J. Reichel. Bose-Einstein condensation on a microelectric chip. *Nature*, 413:498–501, October 2001.

[43] W. Hänsel, J. Reichel, P. Hommelhoff, and T. W. Hänsch. Magnetic conveyor belt for transporting and merging trapped atom clouds. *Phys. Rev. Lett.*, 86:608–611, January 2001.

[44] D. J. Heinzen, R. Wynar, P. D. Drummond, and K. V. Kheruntsyan. Superchemistry: Dynamics of coupled atomic and molecular Bose-Einstein condensates. *Phys. Rev. Lett.*, 84:5029–5033, 2000.

[45] J. Herbig, T. Kraemer, M. Mark, T. Weber, C. Chin, H.-C. Nägerl, and R. Grimm. Preparation of a pure molecular quantum gas. *Science*, 301:1510, 2003.

[46] E. A. Hinds and I.G. Hughes. Magnetic atom optics: mirrors, guides, traps, and chips for atoms. *J. Phys. D: Appl. Phys.*, 32:R119–R146, September 1999.

[47] T.-L. Ho. Bose-Einstein condensates with large number of vortices. *Phys. Rev. Lett.*, 87:060403, 2001.

[48] K. Huang. *Statistical Mechanics.* Wiley, New York, 1987.

[49] M. Inguscio, S. Stringari, and C. E. Wieman (editors). *Bose-Einstein condensation in atomic gases, Proceedings of the International School of Physics Enrico Fermi, Course CXL.* IOS Press, Amsterdam, 1999.

[50] S. Inouye, M. R. Andrews, J. Stenger, H.-J. Miesner, D. M. Stamper-Kurn, and W. Ketterle. Observation of feshbach resonances in a Bose-Einstein condensate. *Nature*, 392:151–154, 1998.

[51] S. Inouye, T. Pfau, S. Gupta, A. P. Chikkatur, A. Grlitz, D. E. Pritchard, and W. Ketterle. Observation of phase-coherent amplification of atomic matter waves. *Nature*, 402:641–644, 1999.

[52] B. Jackson, J. F. McCann, and C. S. Adams. Dissipation and vortex creation in Bose-Einstein condensed gases. *Phys. Rev. A*, 61:051603(R), 2000.

[53] D. S. Jin, M. R. Matthews, J. R. Ensher, C. E. Wieman, and E. A. Cornell. Temperature-dependent damping and frequency shifts in collective excitations of a dilute Bose-Einstein condensate. *Phys. Rev. Lett.*, 78:764, 1997.

[54] S. Jochim, M. Bartenstein, A. Altmeyer, G. Hendl, C. Chin, J. Hecker Denschlag, and R. Grimm. Pure gas of optically trapped molecules created from fermionic atoms. *Phys. Rev. Lett.*, 91:240402, 2003.

[55] S. Jochim, M. Bartenstein, A. Altmeyer, G. Hendl, S. Riedl, C. Chin, J. Hecker Denschlag, and R. Grimm. Bose-Einstein condensation of molecules. *Science*, 302:2101, 2003.

[56] D. W. Keith, M. L. Schattenburg, H. I. Smith, and D. E. Pritchard. Diffraction of atoms by a transmission grating. *Phys. Rev. Lett.*, 61:1580–1583, 1988.

[57] W. Ketterle, D. S. Durfee, and D. M. Stamper-Kurn. Bose-Einstein condensation in atomic gases. Proceedings of the International School of Physics Enrico Fermi, Course CXL, pages 67–176. IOS Press, Amsterdam, 1999.

[58] W. Ketterle and S. Inouye. Does matter wave amplification work for fermions? *Phys. Rev. Lett.*, 86:4203–4206, 2001.

[59] M. Key, I. G. Hughes, W. Rooijakkers, B. E. Sauer, E. A. Hinds, D. J. Richardson, and P. G. Kazansky. Propagation of cold atoms along a miniature magnetic guide. *Phys. Rev. Lett.*, 84:1371–1373, 2000.

[60] M. Kozuma, L. Deng, E. W. Hagley, J. Wen, R. Lutwak, K. Helmerson, S. L. Rolston, and W. D. Phillips. Coherent splitting of Bose-Einstein condensed atoms with optically induced bragg diffraction. *Phys. Rev. Lett.*, 82:871, 1999.

[61] M. Kozuma, Y. Suzuki, Y. Torii, T. Sugiura, T. Kuga, E. W. Hagley, and L. Deng. Phase coherent amplification of matter waves. *Science*, 286:2309–2312, 1999.

[62] C. E. Kuklewicz. Surface excitations and critical velocity of a Bose-Einstein condensate. Master's thesis, Massachusetts Institute of Technology, 2000.

[63] M. Leadbeater, T. Winiecki, D. C. Samuels, C. F. Barenghi, and C. S. Adams. Sound emission due to superfluid vortex reconnections. *Phys. Rev. Lett.*, 86:1410, 2001.

[64] A. E. Leanhardt, A. P. Chikkatur, D. Kielpinski, Y. Shin, T. L. Gustavson, W. Ketterle, and D. E. Pritchard. Propagation of Bose-Einstein condensates in a magnetic waveguide. *Phys. Rev. Lett.*, 89:040401, 2002.

[65] A. E. Leanhardt, A. Grlitz, A. P. Chikkatur, D. Kielpinski, Y. Shin, D. E. Pritchard, and W. Ketterle. Imprinting vortices in a Bose-Einstein condensate using topological phases. *Phys. Rev. Lett.*, 89:190403, 2002.

[66] G. Lenz, P. Meystre, and E. M. Wright. Nonlinear atom optics. *Phys. Rev. Lett.*, 71:3271, 1993.

[67] K. W. Madison, F. Chevy, W. Wohlleben, and J. Dalibard. Vortex formation in a stirred Bose-Einstein condensate. *Phys. Rev. Lett.*, 84:806–809, 2000.

[68] K. W. Madison, F. Chevy, W. Wohlleben, and J. Dalibard. Vortices in a stirred Bose-Einstein condensate. *J. Mod. Opt.*, 47:2715, 2000.

[69] P. J. Martin, B. G. Oldaker, A. H. Miklich, and D. E. Pritchard. Bragg scattering of atoms from a standing light wave. *Phys. Rev. Lett.*, 60:515, 1988.

[70] M. R. Matthews, B. P. Anderson, P. C. Haljan, D. S. Hall, C. E. Wieman, and E. A. Cornell. Vortices in a Bose-Einstein condensate. *Phys. Rev. Lett.*, 83:2498–2501, 1999.

[71] H. Metcalf and P. van der Straten. *Laser Cooling and Trapping.* Springer Verlag, 1999.

[72] F. H. Mies, E. Tiesinga, and P. S. Julienne. Manipulation of feshbach resonances in ultracold atomic collisions using time-dependent magnetic fields. *Phys. Rev. A*, 61:022721, 2000.

[73] D.E. Miller, J.R. Abo-Shaeer, K. Xu, J.K. Chin, J.R. Anglin, and W. Ketterle. In Preparation (2004).

[74] D. Müller, D. Z. Anderson, R. J. Grow, P. D. D. Schwindt, and E. A. Cornell. Guiding neutral atoms around curves with lithographically patterned current-carrying wires. *Phys. Rev. Lett.*, 83:5194–5197, 1999.

[75] M. G. Moore and P. Meystre. Atomic four-wave mixing: Fermions versus bosons. *Phys. Rev. Lett.*, 86:4199, 2001.

[76] T. Mukaiyama, J. R. Abo-Shaeer, K. Xu, J. K. Chin, and W. Ketterle. Dissociation and decay of ultracold sodium molecules. *Phys. Rev. Lett.*, 92:180402, 2004.

[77] P. Nozires and D. Pines. *The Theory of Quantum Liquids.* Addison-Wesley, Redwood City, CA, 1990.

[78] R. Onofrio, D. S. Durfee, C. Raman, M. Khl, C. E. Kuklewicz, and W. Ketterle. Surface excitations in a Bose-Einstein condensate. *Phys. Rev. Lett.*, 84:810–813, 2000.

[79] R. Onofrio, C. Raman, J. M. Vogels, J.R. Abo-Shaeer, A. P. Chikkatur, and W. Ketterle. Observation of superfluid flow in a Bose-Einstein condensed gas. *Phys. Rev. Lett.*, 85:2228–2231, 2000.

[80] C. Orzel, A. K. Tuchman, M. L. Fenselau, M. Yasuda, and M. A. Kasevich. Squeezed states in a Bose-Einstein condensate. *Science*, 291:2386–2389, 2001.

[81] C.J. Pethick and H. Smith. *Bose-Einstein Condensation in Dilute Gases.* Cambridge University Press, 2002.

[82] D. E. Pritchard, A. D. Cronin, S. Gupta, and D.A. Kokorowski. Atom optics: Old ideas, current technology, and new results. *Ann. Phys.*, 10:35–54, 2001.

[83] C. Raman, J. R. Abo-Shaeer, J. M. Vogels, K. Xu, and W. Ketterle. Vortex nucleation in a stirred Bose-Einstein condensate. *Phys. Rev. Lett.*, 87:210402, 2001.

[84] C. Raman, M. Khl, R. Onofrio, D. S. Durfee, C. E. Kuklewicz, Z. Hadzibabic, and W. Ketterle. Evidence for a critical velocity in a Bose-Einstein condensed gas. *Phys. Rev. Lett.*, 83:2502–2505, 1999.

[85] C. A. Regal, C. Ticknor, J. L. Bohn, and D. S. Jin. Creation of ultracold molecules from a fermi gas of atoms. *Nature*, 424:47, 2003.

[86] J. L. Roberts, N. R. Claussen, S. L. Cornish, E. A. Donley, E. A. Cornell, and C. E. Wieman. Controlled collapse of a Bose-Einstein condensate. *Phys. Rev. Lett.*, 86:4211, 2001.

[87] Tim Rom, Thorsten Best, Olaf Mandel, Artur Widera, Markus Greiner, Theodor W. Hnsch, and Immanuel Bloch. State selective production of molecules in optical lattices. *Phys. Rev. Lett.*, 93:073002, 2004.

[88] H. Sakai, A. Tarasevitch, J. Danilov, H. Stapelfeldt, R. W. Yip, C. Ellert, E. Constant, and P. B. Corkum. Optical deflection of molecules. *Phys. Lett. A*, 57:27942801, 1998.

[89] B.E.A. Saleh and M.C. Teich. *Fundamentals of Photonics.* Wiley, New York, 1991.

[90] J.E. Simsarian, J. Denschlag, Mark Edwards, Charles W. Clark, L. Deng, E. W. Hagley, K. Helmerson, S. L. Rolston, and W. D. Phillips. Imaging the phase of

an evolving Bose-Einstein condensate wave function. *Phys. Rev. Lett.*, 85:2040, 2000.

[91] D. M. Stamper-Kurn, A. P. Chikkatur, A. Grlitz, S. Inouye, S. Gupta, D. E. Pritchard, and W. Ketterle. Excitation of phonons in a Bose-Einstein condensate by light scattering. *Phys. Rev. Lett.*, 83:2876–2879, 1999.

[92] D. M. Stamper-Kurn, H.-J. Miesner, S. Inouye, M. R. Andrews, and W. Ketterle. Collisionless and hydrodynamic excitations of a Bose-Einstein condensate. *Phys. Rev. Lett.*, 81:500–503, 1998.

[93] J. Stenger, S. Inouye, M. R. Andrews, H.-J. Miesner, D. M. Stamper-Kurn, and W. Ketterle. Strongly enhanced inelastic collisions in a Bose-Einstein condensate near feshbach resonances. *Phys. Rev. Lett.*, 82:2422–2425, 1999.

[94] J. Stenger, S. Inouye, A. P. Chikkatur, D. M. Stamper-Kurn, D. E. Pritchard, and W. Ketterle. Bragg spectroscopy of a Bose-Einstein condensate. *Phys. Rev. Lett.*, 82:4569–4573, 1999.

[95] J. Stenger, S. Inouye, A. P. Chikkatur, D. M. Stamper-Kurn, D. E. Pritchard, and W. Ketterle. Bragg spectroscopy of a Bose-Einstein condensate. *Phys. Rev. Lett.*, 84:2283, 2000. Erratum.

[96] K. E. Strecker, G. B. Partridge, and R. G. Hulet. Conversion of an atomic fermi gas to a long-lived molecular Bose gas. *Phys. Rev. Lett.*, 91:080406, 2003.

[97] E. Tiesinga, A. J. Moerdijk, B. J. Verhaar, and H. T. C. Stoof. Conditions for Bose-Einstein condensation in magnetically trapped atomic cesium. *Phys. Rev. A*, 46:R1167, 1992.

[98] V. K. Tkachenko. Stability of vortex lattices. *Sov. Phys. JETP*, 23:1049, 1966. Zh. Eksp. Teor. Fiz. 50, p. 1573 (1966).

[99] M. Tsubota, K. Kasamatsu, and M. Ueda. Vortex lattice formation in a rotating Bose-Einstein condensate. *Phys. Rev. A*, 65:023603, 2002.

[100] F. A. van Abeelen and B. J. Verhaar. Determination of collisional properties of cold Na atoms from analysis of bound-state photoassociation and feshbach resonance field data. *Phys. Rev. A*, 59:578–584, 1999.

[101] F. A. van Abeelen and B. J. Verhaar. Time-dependent feshbach resonance scattering and anomalous decay of a Na Bose-Einstein condensate. *Phys. Rev. Lett.*, 83:1550–1553, 1999.

[102] J. M. Vogels, K. Xu, C. Raman, J. R. Abo-Shaeer, and W. Ketterle. Experimental observation of the Bogoliubov transformation for a Bose-Einstein condensed gas. *Phys. Rev. Lett.*, 88:060402, 2002.

[103] Vladan Vuletić, Cheng Chin, Andrew J. Kerman, and Steven Chu. Supression of atomic radiative collisions by tuning the ground state scattering length. *Phys. Rev. Lett.*, 83:943–946, 1999.

[104] Jonathan D. Weinstein, Robert deCarvalho, Thierry Guillet, Bretislav Friedrich, and John M. Doyle. Magnetic trapping of calcium monohydride molecules at millikelvin temperatures. *Nature*, 395:148–150, 1998.

[105] J. E. Williams and M. J. Holland. Preparing topological states of a Bose–Einstein condensate. *Nature*, 401:568–572, 1999.

[106] R. Wynar, R. S. Freeland, D. J. Han, C. Ryu, and D. J. Heinzen. Molecules in a Bose-Einstein condensate. *Science*, 287:1016–1019, 2000.

[107] K. Xu, T. Mukaiyama, J. R.Abo-Shaeer, J. K. Chin, D. E. Miller, and W. Ketterle. Formation of quantum-degenerate sodium molecules. *Phys. Rev. Lett.*, 91:210402, 2003.

[108] E. J. Yarmchuk, M. J. V. Gordon, and R. E. Packard. Observation of stationary vortex arrays in rotating superfluid helium. *Phys. Rev. Lett.*, 43:214, 1979.

[109] E. J. Yarmchuk and R. E. Packard. Photographic studies of quantized vortex lines. *J. Low Temp. Phys.*, 46:479, 1982.

[110] V. A. Yurovsky and A. Ben-Reuven. Formation of a molecular Bose-Einstein condensate and an entangled atomic gas by feshbach resonance. *Phys. Rev. A*, 67:043611, 2003.

[111] V. A. Yurovsky, A. Ben-Reuven, P. S. Julienne, and C. J. Williams. Atom loss and the formation of a molecular Bose-Einstein condensate by feshbach resonance. *Phys. Rev. A*, 62:043605, 2000.

[112] O. N. Zhuravlev, A. E. Muryshev, and P. O. Fedichev. Dissipative dynamics of vortex arrays in anisotropic traps. *Phys. Rev. A*, 64:053601, 2001.

[113] M. W. Zwierlein, C. A. Stan, C. H. Schunck, S. M. F. Raupach, S. Gupta, Z. Hadzibabic, and W. Ketterle. Observation of Bose-Einstein condensation of molecules. *Phys. Rev. Lett.*, 91:250401, 2003.